The self-assembly of chitin nanocrystals into hierarchically structured functional materials

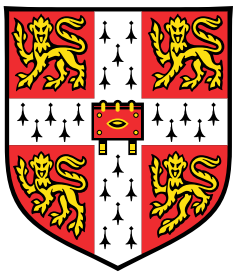

Aurimas Narkevičius

Supervisor: Prof. Silvia Vignolini

Yusuf Hamied Department of Chemistry
University of Cambridge

This dissertation is submitted for the degree of
Doctor of Philosophy

Robinson College June 2021

Declaration

I hereby declare that except where specific reference is made to the work of others, the contents of this dissertation are original and have not been submitted in whole or in part for consideration for any other degree or qualification in this, or any other university. This dissertation is my own work and contains nothing which is the outcome of work done in collaboration with others, except as specified in the text and Acknowledgements. This dissertation contains fewer than 65,000 words including appendices, bibliography, footnotes, tables and equations and has fewer than 150 figures.

Aurimas Narkevičius
June 2021

Abstract

The self-assembly of chitin nanocrystals into hierarchically structured functional materials

Aurimas Narkevičius

To drive more sustainable technological innovations, highly abundant natural resources such as a biopolymer chitin need to be better exploited. In this work, chitin was used to produce rod-shaped nanoparticles, known as chitin nanocrystals (ChNCs) via acid hydrolysis. Firstly, hydrolysis in hydrochloric acid with varied acidity (3.0 and 5.0 M) and duration (90 to 540 min) was investigated to correlate hydrolysis conditions to colloidal and self-assembly properties of the resulting ChNCs. The post processing using tip sonication was investigated, showing that while it reduced the nanoparticle size, the self-assembly properties were not strongly affected, which contrasts with the previously reported findings for cellulose nanocrystals. Using ChNCs allowed to increase the surface charge by means of deacetylation while maintaining the nanoparticle dimensions unaffected, providing evidence that too high surface charge hinders the self-assembly. On the other hand, the process of deacetylation if applied on chitin before the acidic hydrolysis, allows to reduce the nanocrystal thickness without changing the surface charge strongly. As such, nanoparticles of higher aspect ratio can be produced. The importance of the chitin source was evaluated, revealing that ChNCs prepared from mushroom *Agaricus bisporus* were longer, higher aspect ratio, and less crystalline, when compared to shrimp derived ChNCs. Furthermore, fungal ChNCs exhibited self-assembly at lower nanoparticle concentrations and had smaller chiral nematic pitch in comparison to shrimp ChNC studied at comparable conditions. This broad investigation into the preparation conditions of ChNCs is the first of its kind; the field of cellulose nanocrystals is flourishing owing to comparable studies on cellulose nanocrystals. The effect of ionic strength and pH was revisited to demonstrate that these two parameters can be used to effectively tune the self-assembly of ChNCs, and in turn tune the helicoidal nanoarchitecture preserved in the solid state. While the shrimp ChNC system was found to be limited to pitch values ranging from 650 to 4,000 nm in solid state, fungal ChNC suspension could be evaporated to reach helicoidal pitch values small enough to manifest structural colouration. Optical properties of such ChNC films, reported for the first time, were studied in relation

to previously published works and theory to understand their low reflectance, which could be increased by an *in-situ* post-treatment using a concentrated alkali. The resulting chitin conversion into chitosan retained the nanoarchitecture and increased the birefringence from 0.001-0.003 (chitin) to approximately 0.015 (chitosan). Overall, this work provides the basis for designing ChNC preparation conditions to obtain desired colloidal and liquid crystalline properties, outlines the differences between ChNCs and a much more studied system of cellulose nanocrystals, and shows that ChNCs can be successfully used to be used as a functional material.

To those who surround me and myself.

Acknowledgements

There are many to be thanked and acknowledged. I hope that most of them know well that I immensely value their contribution not only to my growth as a scientist but also as a person. A lot of these people belong to my unique research group. Bio-Inspired Photonics instilled into me to do my best, believe in myself and remember that failures inevitably come and go. The very first member and founder of the group, Silvia Vignolini, has been guiding with such words which were always supported by her actions. Never have I seen such a strong person before. Lisa Maria Steiner introduced me to the group and took me under her wing during my initial brittle steps, teaching, guiding, and ensuring that I was always well. In the meantime, Richard Parker and Bruno Frka-Petešić became my scientific sunshine. Giulia Guidetti, Olimpia Onelli, and Rox Middleton, the first-generation PhD students in Bio-inspired Photonics taught me a lot: from a proper optical microscope alignment to literally holding my hand when I was learning SEM and to being astonishing when presenting your research. Cyan Williams, Tianheng Zhao, and Gianni Jacucci, my contemporaries, have shared the same struggles yet never fell and never allowed me to fall. Alyssa Smith, Mélanie Bay, Clement Chan, Thomas Parton, Gea van de Kerkhof, Benjamin Droguet, Laura Catón, Yin Chang, Xiaotian Zhang, Johannes Haataja, Han Yang, and Lukas Schertel have all inspired and taught me many invaluable lessons. John Kah Shang Yeo, Alyce Merryweather, Giuseppe Sportelli, Zihao Lu, and Jordi Ferrer-Orri, were phenomenal students from whom I learnt at least as much as they learnt from me. In particular, Jordi Ferrer-Orri worked with me to obtain results on fungal chitin nanocrystals which led to form a vital part of this thesis. Zihao Lu, who absorbed within months most of what took me years to learn, have span off with new chitin nanocrystal related projects with mesmerising efficiency and imagination. Matthew Pond has been vital in working safely and efficiently in the laboratory. He has always smiled and brought positivity and professionalism to the lab. There are no lab related issues that Matthew Pond couldn't help you to sort out. Duer's group, Yusuf Department of Chemistry, helped enormously with conducting solid state NMR experiments. Yu Ogawa, Gea van de Kerkhof, and Heather Greer assisted numerous times with transmission electron microscopy. Katie King, Nina Warner, Andre Cruz, Jade McCune, Rebecca Forster, Kamil

Sokolowski, and Aniello Palma, from Scherman's group, who have shown that the academic excellence can be combined with fun.

Table of contents

List of figures **xv**

List of tables **xvii**

List of abbreviations **xix**

1 Introduction **1**
1.1 Outline and objectives 2

2 Background **5**
2.1 Chitin and chitosan 5
2.2 Polysaccharide nanocrystals 7
2.2.1 Colloidal properties of polysaccharide nanocrystals 8
2.2.2 Polysaccharide nanoparticle self-assembly 12
2.3 Optics of chiral nematic and helical structures 16

3 Current state of ChNC research **23**
3.1 Motivation for studying chitin 23
3.2 ChNC preparation 24
3.2.1 Hydrolysis in hydrochloric acid 24
3.2.2 Alternative methods 25
3.2.3 CNC preparation 27
3.3 Liquid crystalline properties of ChNCs 28
3.4 Other interesting applications of ChNCs 29
3.5 Potential for ChNC chemical modifications 31
3.5.1 Deacetylation 31
3.5.2 Schiff base formation 32
3.5.3 Click chemistry 32
3.5.4 Inspiration from protein chemical modifications 33

4 Experimental section **35**
4.1 Chitin purification . . . 35
4.1.1 Shrimp chitin . . . 35
4.1.2 Fungal chitin purification . . . 36
4.2 Concentration measurement . . . 36
4.3 Chitin hydrolysis to ChNCs . . . 37
4.4 Tip sonication . . . 37
4.5 Chitin deacetylation . . . 37
4.6 Chitin nanocrystal deacetylation . . . 38
4.7 Ionic strength and pH tuning . . . 38
4.8 Chemical composition characterisation . . . 39
4.8.1 ssNMR spectroscopy . . . 39
4.8.2 Powder X-ray diffraction . . . 39
4.8.3 FTIR spectroscopy . . . 39
4.9 UV-vis spectroscopy . . . 39
4.10 Microscopy . . . 40
4.10.1 TEM . . . 40
4.10.2 SEM . . . 40
4.10.3 AFM . . . 41
4.10.4 Optical microscopy . . . 41
4.11 Casting solid ChNC films . . . 42
4.11.1 Casting films on magnets . . . 42
4.12 ChNC film deacetylation . . . 43
4.13 Colloidal properties . . . 43
4.13.1 Dynamic light scattering and zeta potential . . . 43
4.13.2 Conductometric titration . . . 43
4.14 Liquid crystalline properties . . . 44
4.14.1 Preparation of dilution series . . . 44
4.14.2 Phase diagrams . . . 44
4.14.3 Pitch diagrams . . . 45

5 From chitin to chitin nanocrystals **47**
5.1 Acidic hydrolysis . . . 48
5.1.1 Chemical composition . . . 48
5.1.2 Colloidal properties . . . 52
5.1.3 Liquid crystalline behaviour . . . 54
5.2 Tip sonication . . . 57

5.3 Deacetylation 60
5.3.1 Chitin deacetylation prior acidic hydrolysis 61
5.3.2 Chitin deacetylation after acidic hydrolysis 64
5.4 Mushroom: a different source of chitin 68
5.4.1 Preparing fungal ChNC suspensions 70
5.4.2 Comparing fChNCs and sChNCs 74
5.5 Statistical significance 76

6 Solid ChNC films **79**
6.1 Ionic strength and pH 79
6.2 From a chiral nematic suspension to a solid film 83
6.2.1 Fungal ChNC films 87

7 Conclusions **103**

8 Future work **107**

References **109**

Appendix A Double layer calculations **125**

List of figures

2.1 Molecular structure of cellulose, chitin, and chitosan. 6
2.2 Diffuse ion cloud surrounding rod-shaped nanoparticles. 10
2.3 Liquid crystalline phases of rod-shape mesogens. 12
2.4 Electromagnetic wave and polarisation states of light. 17
2.5 Characteristic liquid crystalline behaviour of chitin nanocrystals. 19
2.6 Structurally coloured CNC films. 21

4.1 Polarised optical microscopy set-up. 41

5.1 FTIR spectra of chitin and ChNCs. 49
5.2 pXRD diffractograms of chitin and ChNCs. 50
5.3 ^{13}C ssNMR spectra of chitin and ChNCs. 51
5.4 Turbidity of ChNCs prepared at different hydrolysis conditions. 52
5.5 Colloidal properties of ChNCs prepared with different hydrolysis conditions. 54
5.6 Transmission electron microscopy micrographs of ChNCs prepared at 3.0 M HCl with varied reaction duration. 55
5.7 Liquid crystalline behaviour of ChNCs prepared at different hydrolysis conditions. 56
5.8 Turbidity of ChNCs processed with different tip sonication times. 57
5.9 Colloidal properties of ChNCs prepared with different tip sonication conditions. 58
5.10 Liquid crystalline behaviour of ChNCs Ts2 sample. 59
5.11 Self-assembly of ChNCs prepared with different tip sonication conditions. . 60
5.12 FTIR spectra of shrimp chitin in its original and partially deacetylated forms. 62
5.13 ^{13}C ssNMR spectra of partially deacetylated chitin and resulting ChNCs. . . 63
5.14 pXRD diffractograms of partially deacetylated chitin and the corresponding ChNCs. 64
5.15 Colloidal properties of ChNCs prepared from partially deacetylated chitin. . 65

5.16 Liquid crystalline behaviour of ChNCs prepared from partially deacetylated chitin. 66
5.17 The effect of directly deacetylating ChNCs on their colloidal properties. . . 67
5.18 Liquid crystalline behaviour of directly deacetylated ChNCs. 68
5.19 Phase separation of 0h and 3h deacetylated ChNC samples. 69
5.20 FTIR spectra of fungal chitin and the resulting fungal ChNCs. 70
5.21 pXRD diffractograms of fungal chitin and resulting fungal ChNCs. 71
5.22 ^{13}C ssNMR spectra of fungal chitin and resulting fungal ChNCs. 72
5.23 The effect of fungal ChNC preparation conditions on their colloidal properties. 73
5.24 Liquid crystalline properties of fungal ChNCs. 74
5.25 Comparison of liquid crystalline properties of fungal and shrimp ChNCs. . 75
5.26 Atomic force microscopy imaging of shrimp and fungal ChNCs. 76
5.27 Comparison of liquid crystalline properties of fungal and shrimp ChNCs. . 77

6.1 Tuning of ChNC self-assembly with ionic strength and pH. 80
6.2 Polarised optical microscopy micrographs of ChNC suspensions at different HCl concentrations. 83
6.3 Tuning of the helicoidal pitch in solid-state films by tailored ChNC self-assembly and gelation. 86
6.4 Structural colouration in fungal ChNC films. 88
6.5 Fungal ChNC titrations used to fine tune surface charge. 90
6.6 Tuning the reflection bandwidth of fungal ChNC films using NaCl and HCl. 91
6.7 Tuning the reflection bandwidth of fungal ChNC films using PEG. 92
6.8 Optical simulations of reflectance spectra of helicoidal structures as a function of thickness and birefringence. 95
6.9 Polarised optical microscopy micrographs of fChNC films cast between two magnets. 96
6.10 Shrimp derived ChNC films cast with patterned polymagnets magnets. . . . 97
6.11 Cross-sectional SEM and FTIR of fungal ChNC before and after deacetylation. 97
6.12 Increased reflectance after deacetylation of fChNC solid-state films. 98
6.13 Comparison of optical properties of fungal ChNC films before and after deacetylation. 99
6.14 Structural colouration in shrimp derived ChNC films after deacetylation. . . 101

A.1 Effective diameter of ChNC as a function of surface charge 126

List of tables

5.1 A summary of ChNC suspensions prepared by various hydrolysis conditions. 48
5.2 Assignment of diffractions peaks observed in pXRD diffractograms. 50
5.3 A summary of fungal ChNC preparation conditions. 70

List of abbreviations

Roman Symbols

^{13}C ssNMR	Carbon-13 solid-state Nuclear Magnetic Resonance
AFM	Atomic Force Microscopy
ChNC	Chitin Nanocrystal
CNC	Cellulose Nanocrystal
fChNC	fungal Chitin Nanocrystal
FTIR	Fourier-Transform Infrared
LC	Liquid crystal
LCP	Left-Circular Polarisation
PEG	Polyethylene glycol
pXRD	powder X-ray Diffraction
RCP	Right-Circular Polarisation
sChNC	shrimp Chitin Nanocrystal
SEM	Scanning Electron Microscopy
TEM	Transmission Electron Microscopy
vol%	Volume percentage
wt%	Weight percentage

Chapter 1

Introduction

The technologies developed in the last century have greatly enhanced the living standards of people around the world. However, it was accomplished by heavily relying on fossil fuel as a starting material which have led to massive environmental issues that the world is currently facing. One of them is the accumulation of waste such as plastics. Nature, on the other hand, rarely leaves waste for a long time as virtually everything is recycled, serving as an inspiration on how to develop technologies of the future which are more sustainable. In fact, enabling the exploitation of highly abundant natural resources is a promising way to develop more sustainable and affordable future technologies.

Along the aspects of sustainability, various natural materials such as teeth, bones, nails, hair, wood, and cuticles are also highly functional. These materials are in fact made of a limited range of the building blocks, primarily, proteins, lipids, minerals, and polysaccharides which is unlike the current human technologies that require a wide range of materials. [1, 2] Despite the apparent simplicity of the building blocks, the deeper understanding obtained by relying on the advances in nanoscience proved these natural yet functional materials to be complex. [3] This is achieved by employing hierarchical structuring on the nanoscale.

In the context of the most abundant biopolymers, namely chitin and cellulose, this hierarchy is observed over several length-scales. The molecules of these polysaccharides are assembled into nano-fibrils which are often organised further to obtain nano-architectures resembling a plywood organisation. Such complex structures impart the organisms with functions such as structural colouration or toughness and resistance to crack propagation. [4–6] As a result, relatively simple repeating building blocks can lead to complex and multi-functional materials, however, the natural assembly processes are still beyond our understanding. [6, 7]

Analogous materials can be produced by relying on artificially tailored self-assembly of cellulose or chitin derivatives and nanoparticles, which spontaneously self-assemble into a

chiral nematic liquid crystalline phase. [8–10] In fact, cellulose derived materials are already highly appreciated for the vibrant structural colouration attainable in liquid and solid state. [7, 11–14] In contrast, chitin based materials are yet to be artificially imparted with functions which have served crabs, shrimps, beetles, and even fungi in their daily struggles for aeons. [15]

1.1 Outline and objectives

While there are many direction in which the research on chitin could propagate, this work is dedicated to study chitin nanocrystals (ChNCs), with a particular emphasis on their self-assembly. Therefore, this work aims to:

1. Establish the connection between preparation conditions and resulting ChNC colloidal and liquid crystalline properties.
2. Establish a routine preparation procedure to achieve ChNCs that self-assemble.
3. Determine the range of ChNCs that can be produced by means of changing the starting material source.
4. Produce solid-state ChNC films with tunable nanoarchitecture.
5. Produce functional ChNC solid-state materials.
6. Study the relationship between the material, its structure and function.

Chapter 2 provides relevant background, required to achieve the objectives outlined above. The theoretical knowledge is integrated with the current knowledge on polysaccharide nanocrystals. Such a combination should provide a comprehensive qualitative framework to be used when dealing with polysaccharide nanocrystals.

Chapter 3 begins with the important question of why one should even bother studying chitin, instead of a similar polysaccharide cellulose, which is not only more abundant but also more investigated. The overview of the current state of ChNC research follows, describing other areas besides their liquid crystalline properties; it includes different approaches in preparing ChNCs, their possible applications as well as potential chemical modifications. Overall, this chapter should give a good context for where the ChNC research is currently at.

Chapter 4 provides details on the experimental conditions, techniques, statistical analysis of the data as well as the source of the reagents that were used in this work.

Chapter 5 focuses on making of ChNCs from chitin. Acidic hydrolysis conditions, namely acidity and duration, are investigated first in relation to colloidal and liquid crystalline properties. A post-processing by tip sonication is explored next. Thereafter, two different approaches are employed to increase the surface charge of ChNCs to establish the effect of this parameter on colloidal and liquid crystalline properties. Lastly, another chitin source, mushroom, is used to prepare ChNCs to better understand the impact of chitin source on the produced ChNCs.

Chapter 6 is dedicated to the use of produced ChNCs in the previous chapter to manufacture functional solid state materials. Given that the liquid crystalline state dictates the structure in the solid state, suspension formulation parameters (i.e., ionic strength and pH) are studied, allowing to tune the chiral nematic pitch in both suspension and solid-state films. Thereafter, the attention is shifted to using fungal ChNCs as these nanoparticles allowed to produce structurally coloured solid state films. Such optical performance of ChNCs, which is reported here for the first time, is studied by bringing forward theory and previously published works on structural colouration. A method to improve and blue-shift the reflected light from fungal ChNC films is then demonstrated, which, when applied on shrimp ChNCs, can shift the reflection to red/near-IR range.

Chapter 7 provides a summary of the key findings and concluding remarks for this work, while chapter 8 outlines the future perspectives for ChNC research.

Chapter 2

Background

2.1 Chitin and chitosan

When we are being annoyed by a perpetually buzzing fly or having a fancy dinner eating a crab topped up with truffle shavings, we rarely stop to think that all of that is only possible because of chitin. Chitin is a ubiquitous biopolymer employed by various organisms, from insects, crustaceans, arachnids and molluscs, to fungi. [15] It not only provides a mere structural support to these organisms but also imparts additional functions such as eye-catching structural colouration or crack resistant shells. [16–18]

A lot of chitin is disposed as a waste product of the fishing or food industries as such tough crustacean shells, unlike the soft inner flesh, are unsuitable as food for human consumption. [15, 19, 20] Chitin constitutes up to 30 % of the crustacean shell dry mass and thus represents an abundant, cheap, and *sustainable* resource. [20] It is thus hardly surprising that crustacean shells currently are the most available raw source of chitin. [15] These mechanically impressive shells contain calcium carbonate, proteins, and pigments besides chitin. Thus it needs to be purified first which is relatively easy to accomplish due to chemical inertness of chitin arising from its molecular structure. [15, 19]

Chitin is a linear polysaccharide made up of repeating β(1-4)-N-acetyl-D-glucosamine monomers which provide many sites for hydrogen-bonding (Figure 2.1). The individual chitin molecular chains assemble into elementary fibrils with a tight packing. [15, 16] Such an organisation, as well as its molecular structure, result in chitin being chemically inert in comparison to proteins, calcium carbonate, and pigments. Therefore, rather mild acidic and basic conditions are sufficient to disintegrate calcium carbonate and proteins with the remnants of red-orange pigments being removed by gentle bleaching. [21] These treatments yield pure chitin.

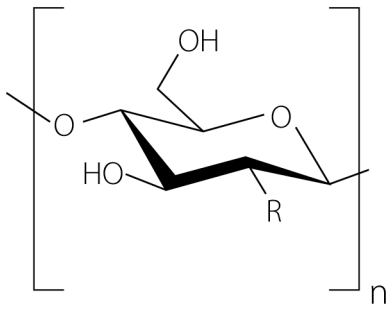

R	Name
−OH	cellulose
$-NH_2$	chitosan
$-HN-C(=O)-CH_3$	chitin

Figure 2.1 Molecular structure of cellulose, chitin, and chitosan. While they differ only by a single substituent, the resulting physicochemical properties are significantly different.

The physical and chemical properties of chitin strongly depend on the hierarchical organisation of chitin molecular chains and thus its source. [15, 16] In nature, chitin molecules are arranged either in parallel or anti-parallel; these organisational patterns are known as β and α crystalline allomorphs, respectively. [16] With chitin molecular chains arranged anti-parallel in α allomorph, the structure overall forms sheets. The sheets themselves are strongly held by intra-sheet hydrogen bonds arising from numerous hydroxy and amide groups. Such a tight packing and numerous interactions result in α-chitin fibres being resistant to dissolution in most common solvents, not swelling as well as not being particularly reactive. [15] Thus, it is not surprising that α-chitin is the most abundant chitin allomorph in nature, found in crustaceans, insects, arachnids, fungi and many more. In some exceptional organisms, like molluscs or *Riftia pachyptila* worms, molecular chains of chitin are arranged in parallel to each other resulting in β-chitin instead, which is a meta-stable chitin allomorph that can be converted to more stable α-chitin by, e.g., base treatment. [16, 22] Whether chitin is of α or β allomorph can be distinguished by X-ray diffraction, FTIR and/or solid-state NMR spectroscopies. [15, 16, 23]

In practice, natural chitin is far from being an ideal crystal as even the molecular chain of β-(1-4)-N-acetyl-D-glucosamine monomers is not perfect. [15] When extracted from the raw resources, chitin is always found to be partially deacetylated, meaning that amine functional groups are present instead of a fraction of the amide groups (Figure 2.1). [10, 15, 24] This deacetylation is likely to be present only on the molecular chains lying at the surface of the chitin elementary fibrils as they are more accessible and do not contribute much to the crystalline-like ordering. The number of amines in comparison to all the available sites is usually quantified by the degree of deacetylation. When it reaches values of 50 % or higher, the physical properties of chitin drastically change, for example, becoming soluble in acidic aqueous conditions. [15]

When chitin becomes soluble in acidic pH because of deacetylation, the molecule is termed chitosan, which is the most known and important chitin derivative. While it can be obtained by employing chitin deacetylase enzymes, most often chitin deacetylation is performed using a concentrated alkali solution. [15, 24, 25] The protonation of chitosan amines, which have $pKa_H \approx 6.3$, occurs in acidic conditions and induces strong electrostatic repulsive forces between chitosan chains as well as increases the hydrophilicity of the polymer. As a result, chitosan is highly soluble in acidic aqueous solvents. [15] This reaction is carried out heterogeneously as chitin itself is insoluble in most common solvents. Only at concentrations above $\sim$40 wt% of sodium hydroxide, can the chitin crystal structure be swelled and deacetylation can be carried out throughout the crystal rather than just at the surface. [24–26]

Practically, most of chitin is used in the form of chitosan as it is inexpensive and non-toxic with uses in many different fields: as an antimicrobial compound in agriculture, as an activator of plant defence responses, as a flocculating agent in waste-water treatment, as an additive in the food industry, as a hydrating agent in cosmetics, as a pharmaceutical agent in biomedicine, wound healing, and also as a biodegradable plastic. [15, 19, 27] While such chitosan applications have highly boosted the use of chitin, a lot of it is still discarded to landfill which could change if it was valorised as a novel nanomaterial.

2.2 Polysaccharide nanocrystals

Chitin has an analogous polysaccharide in the plant kingdom: cellulose (Figure 2.1). Due to the extent of the massive forestry and paper industries the study of cellulose-based systems attracted a wider attention in comparison to chitin. This is especially true in the case of the polysaccharide nanomaterials with chitin being studied mostly as a side project by people interested in cellulose nanocrystals (CNCs). Fortunately, cellulose resembles chitin in primary, secondary, and tertiary structures, and as such the extensive cellulose research provides a wealth of knowledge.

However, even small differences, like the presence of amine/amide in chitin instead of a hydroxy in cellulose result in large differences due to the accumulative effects of the hierarchical organisation of these materials, making it interesting to study chitin based systems.

2.2.1 Colloidal properties of polysaccharide nanocrystals

Chitin and cellulose are water insoluble polysaccharides, unlike e.g., sucrose, a common table sugar. This disaccharide can be readily and homogenously dispersed in water on a molecular level, meaning that every single molecule of sucrose gets surrounded by numerous water molecules. In contrast, chitin and cellulose can only be dissolved in some unusual solvents, but when mixed with water they simply sediment.

Nevertheless, in 1959 R.H. Marchessault discovered a way to disperse chitin in water by obtaining nanoparticles of this polysaccharide by hydrolysis in HCl, inspired by reports on cellulose by Ranby and Mukherjee. [8, 28, 29] While a lot of new ways of preparing chitin nanocrystals (ChNCs) are emerging, in this thesis only hydrolysis in hydrochloric acid is employed as it is the predominant and most promising method. [19] Nanoparticles prepared this way can be well dispersed in water but not a molecular level. [30]

Colloids like ChNCs can be well understood by applying several fundamental concepts of physical chemistry. With many different examples of colloidal systems (e.g. aerosols, fogs, mists, and smoke, emulsions, gels), ChNCs represent colloidal suspensions as they are made of ultra-fine solid particles that can be well dispersed in aqueous medium. This occurs because the dispersed phase has at least one of the dimensions below a micrometre which ensures a considerable surface area to volume ratio resulting in a lot of molecules facing the medium rather than the identical molecules in the bulk. [30]

ChNCs are colloids derived from natural resources and as such they are disperse in their physical dimensions, [10] though it is not to say that they are inferior to many artificial non-disperse systems of identically sized particles. In fact, both systems have their own advantages and uses. [30] ChNCs are rod-shaped averaging to 200 nm in length and 20 nm in width, while CNCs are typically shorter and thinner, with physical dimensions being strongly dependent not only on the preparation methodology but also on the source of the raw material. [10, 31–33] Because of the dimensions being sub-micrometre in size, ChNCs have a large surface areas compared to their volume.

Having a large surface area is usually energetically unfavourable. The loss of attractive van der Waals interactions between similar molecules of chitin are not compensated by the interaction with the surrounding water molecules. Such a system if kept at a constant temperature will spontaneously evolve to lower its free energy. In the case of the colloids, it would mean the formation of aggregates. In fact, many nanoparticles tend to clump up after they are finely dispersed by mechanical means. Rather loose aggregates, or flocs, sometimes separate out but sedimentation or creaming are almost certain if the aggregate coagulates to a much denser form. [30]

Yet, ChNCs can remain well dispersed for months to years. This is because the aggregation follows a mechanism with a transition state that imparts an energy barrier which the system has to overcome. This barrier is higher in energy than the dispersed phase or their aggregates, thus preventing the system to reaching the lowest energy state, i.e. aggregate. The energies in colloidal systems are distributed about a mean value according to the Maxwell-Boltzmann distribution and so there is always a possibility to over-come this energy barrier but if the energy of the system is low compared to the energy barrier, such transformation would progress exceedingly slowly, or practically speaking, would not happen. [30] The energy to over-come such a barrier for ChNC particles arises from a high rate of random encounter with water molecules which is known as Brownian motion (or random walk). The average translational energy of colloidal particles undergoing Brownian motion is $\sim 1.5kT$ (k - Botlzmann's energy, T - absolute temperature), thus it is best to keep ChNC suspensions cool to reduce the aggregation.

The energy barrier in the mechanism of ChNC aggregation originates from long range repulsive forces. These prevent the nanoparticles from coming close enough for the attractive van der Waals interactions to become dominant, leading to aggregation. In the case of ChNCs, the repulsive forces originate from the ionisation of the nanoparticle surface (Figure 2.2 A). The surface of ChNC is decorated with amines with $pKa_H \approx 6.3$, which get completely protonated at pH values below 3, while at pH above 7 the system becomes colloidally unstable. [10, 33] This contrasts with CNCs which are decorated with sulphate half-esters with $pKa \approx 0$ thus making them not sensitive to pH. [34]

This ionisation results in ChNC having a positively charged surface. Due to the principle of electroneutrality, these surface charges have corresponding counter-ions. In solution, however, not all of them are tightly held to the surface and are instead distributed following a Boltzmann's distribution due to the balance between the electrostatic attraction to the nanoparticle surface and entropy driven diffusion outwards. These are the premises of the Debye-H*ü*ckel model which dictates that in the case of a plane surface carrying uniform charge, the electrical potential decreases exponentially with distance from the surface. It can be expressed mathematically as $\Psi = \Psi^0 exp(-\kappa \cdot r)$, where Ψ is the potential at distance r, which decreases from the surface potential Ψ^0 (Figure 2.2A). At a distance equal to $1/\kappa$ the initial potential drops by a factor of $1/exp(1)$. The ion cloud up to this distance is known as a double-layer. Not only does it strongly depend on the initial surface potential but also on the ionic strength, I, since $1/\kappa = const./I$ (Figure 2.2 A). Importantly, the ionic-strength depends not only on the concentration but also on the valency of the counter-ions via $I = \sum(C \cdot Z^2)$. This Debye-H*ü*ckel model can be further expanded as was done by B. Derjaguin, L. Landau, E. Verwey, and T. Overbeek resulting in the so-called DLVO theory. It combines

various attractive and repulsive interactions into an overall energy profile for the potential aggregation mechanism which can be heavily modulated by the ionic strength. [30]

More intuitively, these theories can be understood by considering a charged nanoparticle which randomly moves in suspension and carries along with it a double-layer along. When two such nanoparticles start getting close enough so that their double layers overlap, they begin to repel each other (Figure 2.2 B). This repulsive interaction gets stronger as the overlap increases, as in the overlap region, the concentration of the counter-ions becomes much higher than in the surrounding environment. Consequently, water molecules start to diffuse in to reduce this ion concentration gradient, thus resulting in the apparent repulsive interactions. This electrochemical gradient is extremely high, however, at sufficiently high ionic strength, the overlap region never creates a strong enough gradient for water to diffuse in to separate two approaching nanoparticles and so they can get close enough so that the short-range attractive interactions take over.

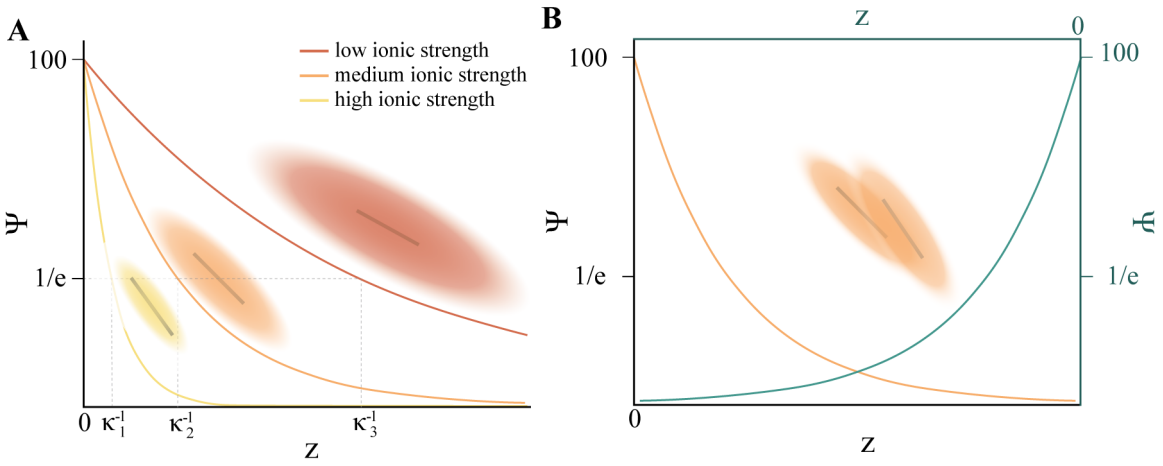

Figure 2.2 Diffuse ion cloud surrounding rod-shaped nanoparticles. **A** Double layer exponentially shrinks with distance from the particle surface and depends on the ionic strength. **B** Ion concentration and repulsive potential increase locally when the double-layers of two nanoparticles start to overlap.

While these theories were developed for uniform spherical nanoparticles with uniform charge distribution at low concentrations, they provide a surprisingly convenient qualitative description to describe the behaviour of ChNC suspensions. The double-layer essentially can be considered to add an additional non-overlapping layer to the physical nanoparticle dimensions. As a result, the *effective* length and diameter become $L_{eff} = L + 2 \cdot 1/\kappa$ and $D_{eff} = D + 2 \cdot 1/\kappa$, respectively. This is a less prominent effect on ChNC length as it is a much larger dimension than the diameter or the double-layer size. This simplification provides good working grounds to understand the effects of the double-layer but for a more

extensive discussion the reader is referred to Appendix A. As a result, the effective ChNC aspect ratio, L/D_{eff} decreases, with particles looking less spindle like while the effective volume, $V_{eff} = L \cdot {D_{eff}}^2$ increases. When the ionic strength is low, the ChNCs have an enormous effective volume causing jamming of the nanoparticles and gel-like behaviour even at low concentrations. This is an example of a repulsive gel, or Wigner glass, which was thoroughly studied for CNCs. [35–37] On the other hand, when the ionic strength is high, the double-layer is thin, allowing the nanoparticles to get close enough for the attractive interactions becoming relatively strong thus developing the nanoparticle suspension into an attractive gel via formation of a percolating network of aggregates. [36–38]

It has important consequences when well dispersed ChNC suspensions are dried to form solid state materials. Initially a moderate ionic strength is used to disperse these polysaccharide nanoparticles so they would not form neither a repulsive, nor an attractive gel. However, the ionic strength inevitably increases as the suspension dries, resulting in a thinning double-layer. Eventually a critical ionic strength is reached which promotes gelation via attractive interactions. In the case of CNCs, this kinetic arrest can be obtained at nanoparticle concentrations ranging from 2-25 wt% by fine tuning the ionic strength of the suspension and appears to be mostly related to the absolute ionic strength. [7, 38–42] Due to this kinetic arrest, the defects and particle configurations within the gelled suspension can be preserved upon complete drying.

Besides the ionic strength, the surface charge also influences the double-layer thickness and, in fact, is the reason for its appearance in the first place. The electrostatic stabilisation of ChNCs result from a number of protonated amines. It is directly related to the degree of deacetylation at ChNC surface which could be inferred by methods such as solid-state NMR or IR spectroscopies, elemental analysis, and conductometric titration. [15, 23, 24] However, only conductometric titration truly probes the number of amines on the nanoparticle surface, which contribute to the colloidal stability, and the titration is performed akin to a weak acid - strong base titration. [24] The surface charge reaches the values of around $\sim 300\ mmol_{-NH_3^+}/kg_{ChNC}$, which results from a low degree of deacetylation found naturally in chitin in conjunction with some deacetylation happening during the acid catalysed amide hydrolysis during ChNC preparation. [10, 24] However, the absolute surface charge can be increased by a further hydrolysis under basic conditions, while the adjustment of the pH in the range of 2-7, the number of amines that are protonated can be tuned, which may prove to be advantageous when high surface charge is required. [24, 25, 43, 44] In contrast to ChNCs, the surface charge of CNCs is limited to $\sim 300\ mmol_{-OSO_3^-}/kg_{CNC}$. The maximum surface charge in CNCs can be altered by tuning the hydrolysis conditions but altering them also results in changes to the physical dimensions of CNC. [31, 32] Then it

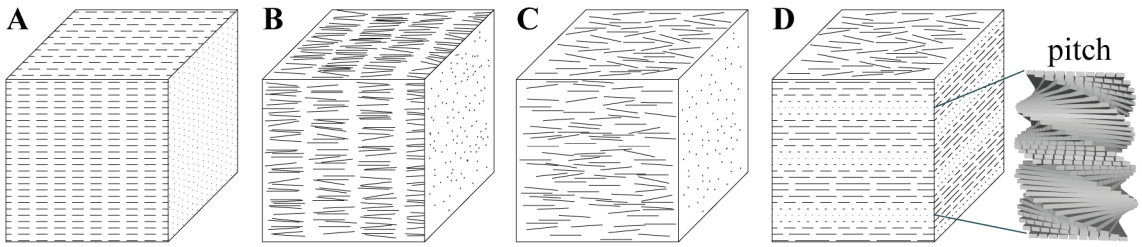

Figure 2.3 Crystalline and liquid crystalline phases of rod-shape mesogens. The rod-shaped ChNCs in theory could achieve **A** crystalline, **B** smectic, **C** nematic, or **D** chiral nematic phases, however, only the chiral nematic phases have been observed.

can be controllably reduced by acid catalysed desulphation at elevated temperatures. [45] However, this desulphation happens, though slower, even when CNC suspensions are kept at low temperatures ($\sim$5 °C), however, the effect becomes non-negligible during long term storage (months to years) confirmed by changes in the CNC colloidal properties. [45]

2.2.2 Polysaccharide nanoparticle self-assembly

With the ionic strength and surface charge well controlled, ChNCs remain colloidally stable over a range of concentrations. Interestingly, the same researcher who discovered ChNCs in 1959, also described that ChNCs exhibit a peculiar behaviour at higher concentrations. [8] The suspension separated into two distinct phases if left unperturbed, with the bottom phase appearing bright when observed between the crossed-linear polarisers with a back illumination while the top phase remained dark (Figure 2.5). [10, 33] This interaction with the polarisation of light is indicative that the bottom phase of the material is birefringent and anisotropic, similar to molecular liquid crystals such as cholesterol derivatives. [46]

Liquid crystals (LC) are materials constructed of mesogens which overall flow like a liquid but attain some ordering thus reminiscent of the crystal. There are many known organic molecular mesogens exhibiting liquid crystalline behaviour which arises primarily due to a high geometrical anisotropy. [46] Interestingly, geometrically anisotropic colloids exhibit a similar behaviour which was described in proteins such as the tobacco virus, amyloid fibrils, and collagen and polysaccharide nanoparticles such ChNCs. [6, 7, 46] The transitions between different LC phases can be promoted by a number of factors that can be divided primarily into either thermal changes (thermotropic LC) or changes in composition (lyotropic LC). In principle there are several ordered phases that can be formed from rod-like mesogens such as ChNCs:

- Crystalline phase (Figure 2.3 B). It is the ultimately organised state, a colloidal crystal, however, virtually unachievable for disperse colloids such as ChNCs. This structure would be rigid and would not flow, unlike the liquid crystals (LCs).

- Smectic LC phase (Figure 2.3 B). The mesogens align in parallel along a common director **n** as well as in well-defined planes and so is the most ordered phase of the three possible LC phases since it has long range directional and translational order. The phase can be further subdivided if the director **n** is perpendicular to each layer (Smectic A) or tilted at an angle (Smectic C).

- Nematic LC phase (Figure 2.3 C). The mesogens align in parallel along a common director **n** but in the absence of long-range translation order. Another vector **m** can be defined which is perpendicular to the director **n**.

- Chiral nematic (or cholesteric) LC phase (Figure 2.3 D). The mesogens align parallel along a common director **n** which continuously rotates in the plane perpendicular helix director **m**. The distance over which the common director **n** makes a 360° rotation is called the chiral nematic pitch (p).

When aqueous suspensions of ChNC (or CNC) are concentrated, they spontaneously self-assemble into an ordered phase. [8–10] Such anisotropic phase starts to form after a threshold concentration, C_I, following a nucleation and growth mechanism. Small spherical formations, known as tactoids, spontaneously appear and grow. They have a higher local nanoparticle concentration and, therefore, are denser than the surrounding isotropic suspension and sediment. Initially each individual tactoid can be characterised by its own individual nanoparticle alignment and orientation in suspension. After sedimentation they start to merge into domains which may further relax into a uniform continuous macroscopic phase. [9, 10, 13, 33, 47–50] The amount of the anisotropic phase formed typically increases linearly with the nanoparticle concentration until it reaches a second threshold concentration, C_A, after which the entire suspension is fully anisotropic. [51]

This self-assembly of colloidal nanoparticles was first explained in the seminal paper published by L. Onsager in 1949. [52] Onsager's theory considers a monodisperse population of long and thin hard rods which are well dispersed in a continuous medium. Such hard rods with a high aspect ratio do not interact at all except that they are not allowed to intersect one another. At low concentrations these rods are spaced apart sufficiently that they can take any possible orientation without having to intersect with the neighbouring rods. This behaviour is equivalent to an isotropic liquid. However, as the concentration increases, the neighbouring rods are forced into closer proximity which limits their freedom to occupy

certain orientations. As a result, they start to jam but by sacrificing some orientational entropy for a gain in a translational entropy, a proportion of the system begins to order into a nematic liquid-crystalline phase. Although counter-intuitive, the overall result is that the overall entropy of the system is maximised by having a part of the system ordered as a nematic phase. [53] A qualitatively extremely useful result derived from this theory is that the transition from isotropic to a nematic liquid crystalline phase depends on the excluded volume of the particles and is inversely proportional to the aspect ratio of the rods. The threshold volume fractions (or concentrations) for the isotropic ϕ_I and anisotropic ϕ_A nematic phase are simply a function of the inverse aspect ratio multiplied by a constant: [52, 54, 55]:

$$\phi_I = 3.3 \times \frac{D}{L}, \phi_A = 4.5 \times \frac{D}{L} \tag{2.1}$$

This essentially means, that when the nanoparticle concentration is below ϕ_I, only the isotropic phase is formed. However, when the average suspension concentration is in-between ϕ_I and ϕ_A, the suspension separates into isotropic and anisotropic parts, which are of ϕ_I and ϕ_A concentrations, respectively. However, when the average nanoparticle concentration is beyond ϕ_A, only anisotropic phase will be formed.

The assumptions employed in this model resemble well the behaviour of ChNCs which can be approximated as long thin rods. They can be further assumed to be non-interacting by simplifying repulsive interactions as simply non-overlapping effective length and diameter (i.e. L_{eff} and D_{eff}) arising from the double-layer. This description works well to qualitatively describe the tendencies of ChNCs to phase separate. In addition, the theory has been refined to circumvent some of the assumptions, limiting its quantitative applications, by including electrostatic interactions, dispersity, and lower aspect ratio. [49, 56–60]

The threshold concentrations for ChNC phase transitions are determined by the nanoparticle physical dimensions and the ionic strength via effective dimensions as expected from the Onsager's theory. [33, 52] Addition of electrolytes to ChNC suspensions increases both C_I and C_A because the double layer and so the effective rod volume shrinks. In contrary, the effective aspect ratio would increase, predicting lower threshold concentrations. However, the experimental observations suggest that the change in the effective volume is the dominant factor in determining the phase transitions threshold concentrations when the ionic strength is tuned. [33, 49, 52, 61, 62] Similarly, increasing the surface charge leads to higher threshold concentrations of ChNC and CNC suspensions. [24, 63]

This phase separation can be exploited to tailor the nanoparticle dispersity in terms of size and the overall average size. Extrapolating from the Onsager's theory, for a disperse suspensions, such as ChNC, the high-aspect ratio (or generally large) nanoparticles transit

into the anisotropic phase at a lower concentration than those with smaller aspect ratios. Thus by physically separating anisotropic and isotropic phases from the initially biphasic suspension results in two new suspensions which have different nanoparticle distributions in terms of size. Then, if the anisotropic suspension is diluted, a biphasic suspension can be obtained which can be physically separated into anisotropic and isotropic phases. Similarly, isotropic phase can be concentrated. Consequently, by repeatedly physically separating anisotropic and isotropic phases several suspensions can be obtained which have different sizes with narrower distributions and thus different liquid crystalline behaviour. [62] To an extent size sorting can also be obtained by centrifugation where the nanoparticles of the lower volume remain suspended while the rest of the rods form a pellet. [64] In this way, large aspect-ratio ChNCs could be separated out though not as well as by means of phase separation and with a lot of waste.

However, ChNCs form a chiral nematic rather than a nematic phase but the latter can be considered to be a case of a chiral nematic phase with an infinite pitch. [10, 33] In fact, the nematic and chiral nematic LC phases are comparable in an overall energy as the energy of twisting is small compared to the overall energy of parallel ordering of mesogens which can be confirmed experimentally as minute amounts of molecular chiral nematic LC are sufficient to dope the molecular nematic LC with the whole phase obtaining chirality. [46] In this way molecular nematic liquid crystals can be forced to form left-handed or right-handed chiral nematic phases.

In contrast, the chiral nematic phase of ChNCs (and CNCs) is always a *left-handed* helical structure. [10, 33, 65, 66] While other cellulose derivatives, such as hydroxypropyl cellulose, can also form chiral nematic structures that have a *right-hand* helical structure. [11, 67] Thus, it is unlikely that chirality in the molecular structure is solely responsible for the translation of chirality of the final liquid-crystalline phase. In fact, the origin of chirality in these phases is not clear and it could result from the nanocrystal shape, their bundled aggregates acting as chiral dopants, chiral distribution of the surface charges, and the twisting of the crystal structure. [66, 68–72] Regardless of the origin of the chirality, the fact that only left-handed structures are formed by ChNCs or CNCs indicates that specific interparticle interactions are employed. However, these must be different in magnitude for ChNCs and CNCs, as the chiral nematic pitches and thus the twisting strengths are rather different. [33, 63]

The pitch, in these polysaccharide nanoparticle suspensions, depends on many parameters, for example, attractive and repulsive interactions which can be easily adjusted. The addition of simple electrolytes (e.g. NaCl, KCl) to the aqueous suspension causes the pitch to decrease which can be related to the thinner double-layer and smaller effective nanoparticle volume (Figure 2.2 A). Consequently, the physical nanoparticles can pack denser to each

other, resulting in stronger chiral interactions. [62, 65, 66, 68, 73, 74] Also, only for ChNC suspensions a complex non-linear behaviour as a result of HCl addition to ChNC suspension was found. [33] This behaviour results from the intricate balance between increasing the ionic strength and the surface charge, as they appear to exhibit opposite effects on the chiral nematic pitch. Indeed, the chiral nematic pitch was observed to decrease as CNCs surface charge was lowered by, e.g., autocatalytic desulphation. [45, 63, 65, 73] The attractive interactions between the nanoparticles can be enhanced by employing a high permittivity solvent which results in smaller pitch values. [45] Lastly, even a commonly applied tip sonication treatment used to better disperse these suspensions was shown to affect the liquid crystalline behaviour. [65, 75]

This chiral nematic structure thus formed can be preserved when the colloidal liquid crystals, such as ChNCs, are dried. This is unique for colloidal liquid crystals as they become gel-like when the suspensions are allowed to dry due to the inevitable increase in ionic strength and particle concentration leads to a formation of a gel. The drying process proceeds, accompanied only by the shrinkage of the gelled suspension. This behaviour has predominantly been described with CNC suspensions where the micrometre pitch in liquid state becomes mechanically compressed to hundreds of nanometres, permitting the interaction with the visible light. [76] While there is only a single mention of the possibility to preserve the helicoidal structure of ChNCs into the solid state, [10] this attractive optical functionality arising from the helicoidal nanoarchitecture in solid state has become one of the key aspects of science in CNCs. [13, 42, 45, 47, 47, 65, 75, 77–79] Thus, it suggests that either ChNCs are far from being understood or there are some fundamental differences between the two systems, or both, explaining the lack of structurally coloured materials being produced from chitin.

2.3 Optics of chiral nematic and helical structures

While the colour does not appear to be the most important aspect of humans' life, it brings a lot of joy and meaning to life. The use of nanoarchitecturing of otherwise colourless materials to produce structural colouration is a wide-spread strategy in nature. [5, 80–82] Most of the examples are present in the animal kingdom, specifically *Arthropoda*, where chitin is used as one of the principal building blocks. Structural colour gives the organisms much more brilliant and intense looking colouration in comparison to colours obtained from dyes or pigments and serve an important role for the interspecies communications. [81] This is achieved because of the structural colouration may give rise to additional optical effects such as selective reflection of light of a specific polarization or angle dependence.

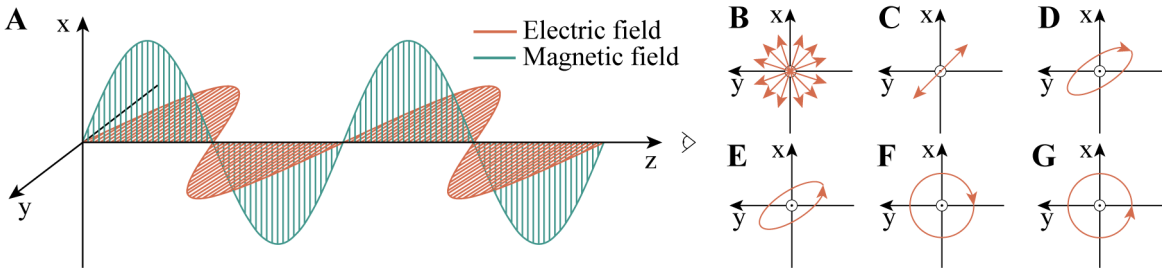

Figure 2.4 Electromagnetic wave and polarisation states of light. **A** An electromagnetic wave is comprised of electric and magnetic fields oscillating perpendicular to each other and the propagation direction. The polarisation of light is defined as the direction of electric field oscillation which, when looking towards the light source, can be categorised as **B** random, **C** linear, **D** right elliptical, **E** left elliptical, **F** right circular, and **G** left circular polarisations. However, the definitions of handedness vary among different scientific fields. [84]

[81] Besides, the materials with structural colour are much more resistant to colour changes because of light bleaching or thermal degradation which are notable problems for pigment based colours. [78] The ability to produce structurally coloured materials analogous to the ones found in nature is highly desirable: a single cheap and highly available biodegradable biopolymer, like cellulose or chitin, could allow to attain the whole range of colours by tuning its nano-architecture, to be used in new branches of art, decoration, or to replace various polluting plastic-based materials, e.g., glitter in cosmetics. Structural colouration could be used as sensors for, e.g., humidity or various molecules, which could be detected via colour change due to the changes in the nanoarchitecture and/or refractive index.[83]

To better understand light matter interaction with chiral nematic phase and helicoidal architectures, it is important to recall some concepts about light. In fact, light is an electromagnetic wave characterised by its wavelengths. It is a combination of electric and magnetic fields oscillating periodically with time (Figure 2.4 A). These two fields are perpendicular to each other and also to the light propagation direction. [84] By convention, the direction of the electric field oscillation describes the polarisation of light which is vital for the emergence of structural colouration in the case of helicoidal nanoarchitectures, among other things.

When the light propagates along an arbitrary direction **z**, the electric field can only oscillate in a perpendicular plane constrained to **x** and **y** directions (Figure 2.4 A). Therefore, any polarisation of light can be expressed as a combination of the electric field components in **x** and **y**. It is more convenient to look at a more formal equation, derived by solving Maxwell's equations, describing electromagnetic wave travelling through a material with a refractive index n (Equation: 2.2). [85]

$$\mathbf{E} = E_{0x}exp(i(kz - \omega t + \phi_x)\mathbf{x} + E_{0y}exp(i(kz - \omega t + \phi_y))\mathbf{y} \tag{2.2}$$

where

- E_{0x} and E_{0y} are the initial electric field amplitude components in **x** and **y** directions, respectively.
- k is the magnitude of the wave vector, which described the direction of light propagation. The magnitude, however, is known as a wavenumber and is equal to a number of waves per unit distance.
- z is the position along the light propagation direction at a given time.
- t is the time.
- ω is the angular frequency of oscillations, which is related to the more familiar frequency $f = \frac{\omega}{2\pi}$.
- ϕ_x and ϕ_y are the phase of the electric field in the **x** and **y** directions. The phase gives an offset from the 0^{th} position for the periodically oscillating waves.
- **x** and **y** are the unit vectors along x and y directions and have magnitude equal to 1 and they define the plane in which the electric field oscillates.

From this equation, it can be inferred that only the electric field amplitude components E_{0x} and E_{0y} and the phases ϕ_x and ϕ_y determine the direction along which the electric field oscillates and so the polarisation of light. In general, four main types of light polarisation can be described: [84]

- Random (or natural) polarisation occurs when many coherent light beams with different polarisations are superimposed. Various sources natural (e.g. sun) or artificial (e.g. incandescent lamp bulb with a filament) can provide such a light (Figure 2.4 B).
- Elliptical polarisation occurs when $E_{0x} \neq E_{0y}$ and $\phi_x \neq \phi_y$ and it can obtain any real value. The electric field vector defines an ellipse in the xy-plane (Figure 2.4 D, E).
- Circular polarisation occurs when $E_{0x} = E_{0y}$ and $\phi_x = \phi_y \pm \frac{\pi}{2}$. The electric field vector defines a circle in the xy plane. This can be achieved by the electric field rotating clockwise (RCP) or anti-clockwise (LCP) when viewed towards the light source (Figure 2.4 G, F).
- Linear polarisation occurs when $E_{0x} \neq E_{0y}$ and $\phi_x = \phi_y$. The electric field vector defines a line in the xy-plane (Figure 2.4 C).

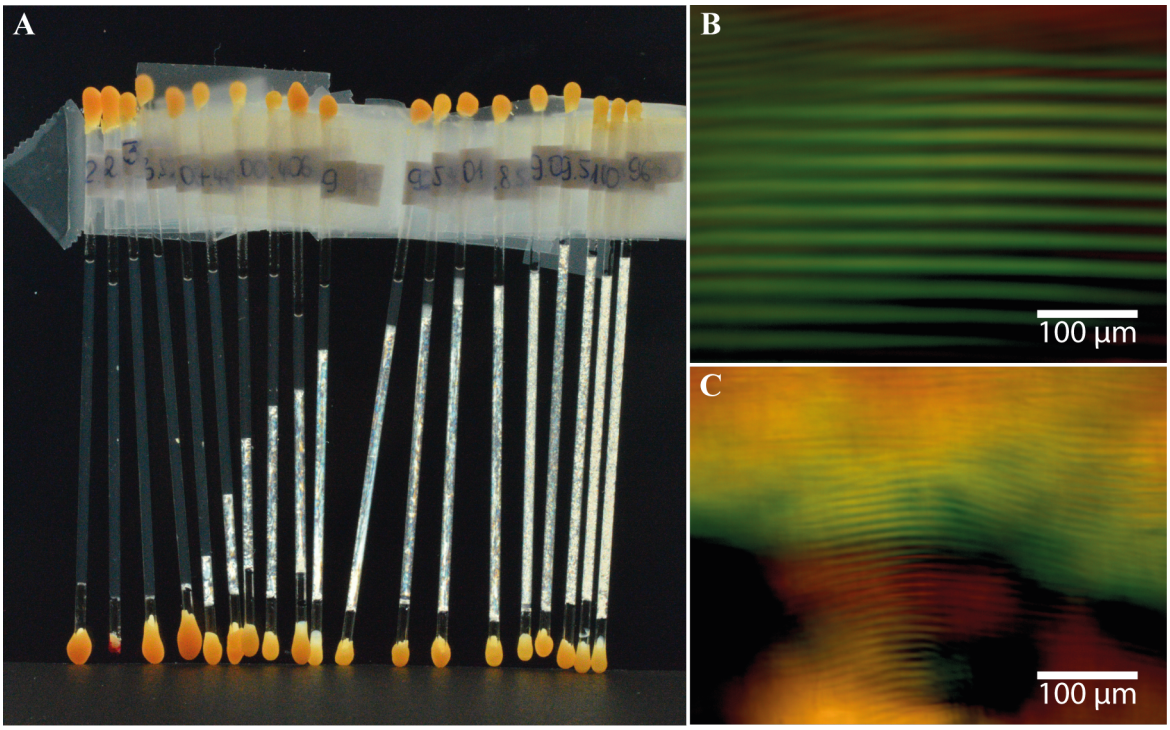

Figure 2.5 Characteristic liquid crystalline behaviour of chitin nanocrystals. **A** The anisotropic phase starts form past the first threshold concentration, with the volume fraction of anisotropic phase increasing with the nanocrystal concentration until the whole suspension becomes fully anisotropic. **B** The anisotropic phase exhibits characteristic fingerprint pattern when looked at by polarised optical microscopy. **C** The spacing, equal to half the chiral nematic pitch, becomes smaller as suspension gets concentrated.

One of the applications of linearly polarised light for ChNCs, is to study their self-assembly because ChNC suspension are birefringent. Birefringence is a term used to describe the refractive index contrast and in general can be further divided into two categories. [84, 86] Intrinsic birefringence arising from the crystal-like molecular arrangement of a cellulose or chitin. While the studies on chitin optical constants are scarce, it is well known that CNCs have a higher refractive index along their long axis than perpendicular to it. [79, 87, 88] Form birefringence arises when geometrically anisotropic particles are ordered in medium of a different refractive index as in the case of ChNCs aqueous chiral-nematic phases as there is a refractive index difference between chitin and water, called form birefringence. Therefore, the isotropic and anisotropic phase separation can be easily distinguished by observing the suspension between crossed-linear polarisers with back illumination (Figure 2.5 A). The isotropic phase is not birefringent, so it remains dark overall, while only the anisotropic phase alters the polarisation direction of light, thus resulting in a brighter appearance when looked at between crossed-linear polarisers. [9, 13, 34, 79, 89, 90]

Beyond just the bright appearance, which could be attained by any ordering of ChNCs, the appearance of a fingerprint pattern under polarised optical microscopy (POM) is characteristic of chiral nematic ordering (Figure 2.5 B, C). [10, 33] When the sample is oriented so that the light propagates through the chiral nematic LC *perpendicular* to the helical director **m**, it encounters periodic variation in the refractive index. [46] The maximum transmission occurs when the ChNCs are aligned perpendicular to the direction of light propagation and minimal when they are parallel. [91] In this way, one can measure the chiral nematic pitch equal to twice the periodicity of the fingerprint pattern, which is usually several to tens of micrometres for CNC and tens to hundreds of micrometres for ChNC aqueous suspensions. [9, 10, 33, 34]

In contrast, when the light impinges on the chiral nematic LC like structures *parallel* to the helical director **m**, it encounters a spatially modulated continuous and periodic refractive index variation because ChNCs have intrinsic birefringence. In the case of CNCs, it can result in selective reflection of visible light, if the pitch is of the chiral nematic structure is comparable to the wavelength of light (Figure 2.6 A). Such structures can be approximated as Bragg diffractors of finite thickness with repeating units every half-pitch. Superimposing numerous interferences from the inside of the film, the reflected wavelengths can be calculated to be $\lambda = n_{avg} \times p \times cos(\theta)$, where n_{avg} is the average refractive index, p is the chiral nematic pitch, θ is the angle between the direction of incident light and the helical director **m**. [92] This can be further simplified by assuming an illumination and reflection at ($\theta = 0\,^{\circ}$), giving an easily applicable equation; $\lambda = n_{avg} \times p$.

However useful this model is, it is an oversimplification that does not account for the reflected light being circularly polarised. Whether LCP or RCP light is reflected depends on the handedness of the helicoidal structure (Figure 2.6 B, C, E). For example, only LCP light is reflected by CNC films as they have a left-handed helicoidal structure, while only RCP light comes back from the hydroxypropyl cellulose samples as they have a right-handed helicoidal structure. [13, 47, 65, 93] Light of opposite handedness compared to the structure is simply transmitted. Such observations can be explained by more sophisticated analytical or numerical methods. [94–99]

De Vries in 1951, [97] considering the chiral nematic LC as a stack of infinitesimally thin layers of different refractive indices corresponding to the chiral nematic LC, provides a solution to the Maxwell's equations in this geometry. This approach describes why LCP, but not RCP, light is reflected by CNC films as well as it can be used to calculate the expected reflectance spectra (Figure 2.6 D). [98] The type and the amount of light reflected thus depends on many parameters such as the angle θ between the angle of the incident light and

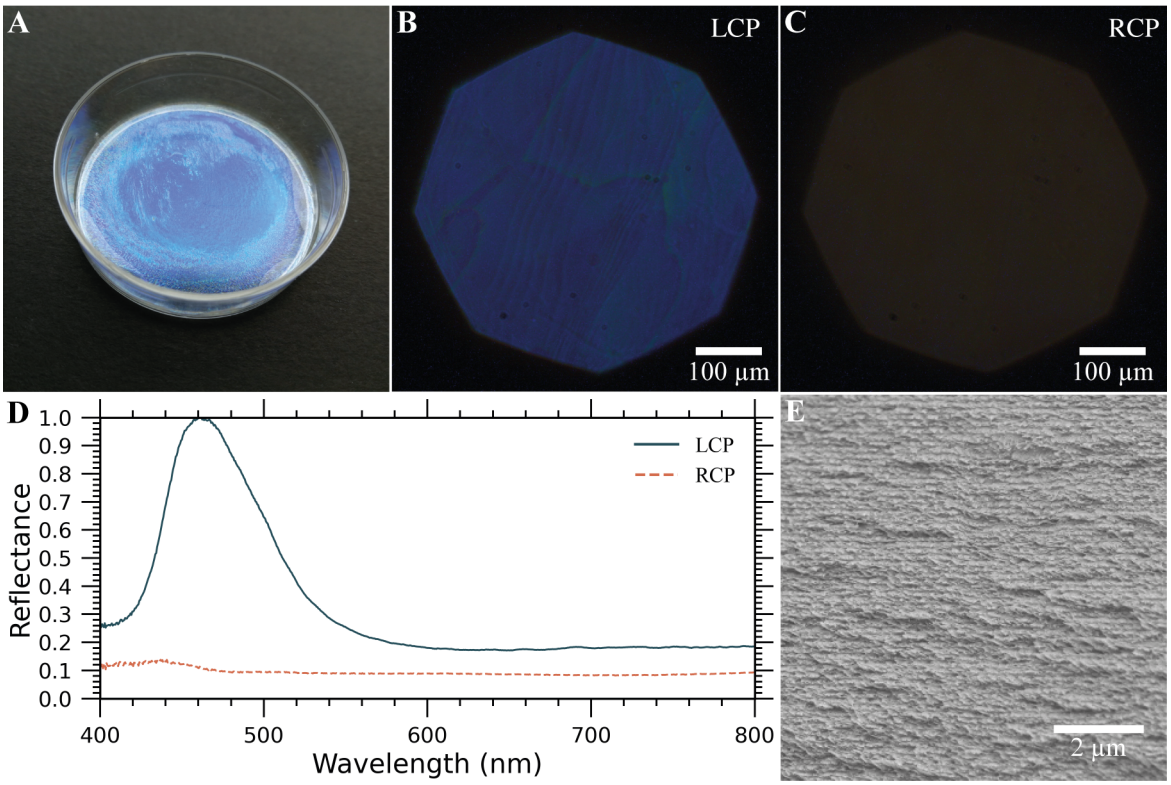

Figure 2.6 Structurally coloured CNC films. **A** A photograph of a structurally coloured dry CNC film. **B, C** Polarised optical microscopy reveals that the colour is only present in the LCP channel, with RCP light not being reflected. **D** Corresponding reflectance spectra show that such films selectively reflect 100 % of the LCP light of the appropriate wavelength. **E** A cross-section of a structurally coloured CNC film. *Data for this figure was provided by Benjamin Droguet, Yusuf Hamied Department of Chemistry, University of Cambridge.*

helical director **m**, the average refractive index n_{avg}, birefringence, thickness, the pitch and handedness of the chiral nematic-like structures. [91, 97, 98, 100]

In fact, by combining linear polariser and quarter-waveplate in a particular arrangement, it is possible to characterise such samples in detail (Figure 4.1). The reflected LCP or RCP light can be distinguished by a quarter-wave plate followed by a linear polariser (Figure 2.6 B, C, D). The quarter wave plate induces a phase delay of $\pi/2$ which, as described above, will transform LCP and RCP light into LP light which would oscillate in different directions. Then a linear polariser oriented at $-\pi/4$ would allow only the light which was originally LCP to pass through and $+\pi/4$ orientation only for RCP. When such optical components are combined with a microscope and spectrometer, the reflected wavelength and its reflectance can be measured as well as the handedness (Figure 2.6 D). Such measurements can now be easily compared to computational calculation. [101]

Chapter 3

Current state of ChNC research

3.1 Motivation for studying chitin

Chitin is an amino polysaccharide which is biologically active, unlike cellulose. [102] Chitin (and chitosan) can be used as materials that promote wound-healing and improve cosmetic skin restoration. [102–104] This polysaccharide exhibit hypolipidemic activity, when ingested as dietary fibre, as well as increases lipid digestion, as confirmed by *in vivo* and *in vitro* experiments. [102, 105] When tested for antibacterial and antifungal properties, chitin and especially its derivative chitosan show strong effects. In addition, plant germination and growth can be improved by coating seeds with chitosan. [102, 106]

In nature, chitin is widely associated with various proteins. In the phylum of *Arthropoda*, various structural proteins in the cuticle have a highly conserved chitin binding motif. [107, 108] Better understanding chitin and ChNCs will enable to approach the study of chitin-protein interactions from a materials science perspective to better understand the function of such interactions in nature. There is also a potential in harvesting the knowledge of such chitin-protein interactions to produce high-end functional products. [109, 110]

Chitin nanocrystals (ChNCs) have better thermal stability in comparison to cellulose nanocrystals (CNCs). [111–113] The latter material suffers from a decreased thermal stability partly because of the sulphate half-ester groups, which are grafted onto cellulose surface during the nanocrystal preparation. The temperature of degradation for CNC is 250 °C while that for ChNC is 280-300 °C. In addition, chitin has a better stability than cellulose when exposed to chemicals, in particular to alkali, which originates from a much tighter chitin hydrogen bonding network. [15, 114] The hydrogen bonding makes chitin less prone to swelling in water than cellulose.

ChNCs have an advantage when considering the sustainability and cost of production of the material. While 3.0 M (10 wt%) HCl is commonly used to produce ChNCs, 64 wt%

H_2SO_4 is required to prepare CNCs, at comparable solid-to-liquid ratios. The acid used in the process is hard to recover and usually discarded. [10, 115] Furthermore, there is a promising emerging way to sustainably obtain chitin from insect farming, since they grow fast and could produce chitin in large quantities. Insect farming is promising for their high protein yield per area when compared to other protein sources: mealworm requires 18 m^2 to produce 1 kg of protein, which is significantly lower than 200 m^2 per kg required for obtain beef protein. [116] The other advantages include lower light and water consumptions as well as a sustainable source of food (e.g., crop waste). [117, 118] Chitin constitutes 5 to 10% of insect dry mass and can be easily separated as evidenced by the successful bio-refinery approach to separate proteins, lipids, and chitin from black fly pupae. [118, 119] Besides, growing insects molt frequently, leaving behind chitin-rich shells, which can be harvested directly for chitin. Improving the value of chitin products is one of the steps to promote insect farming industry.

ChNCs much like CNCs exhibit liquid crystalline properties. [7, 10] However, many fundamental questions still remain unanswered and, in this respect, ChNCs can serve not only as an interesting yet less explored system on its own right, but also as a valuable comparable system to evaluate the generality of the theories of colloidal self-assembly established on the grounds of only CNCs. This is especially true when considering the enigmatic origin of chirality in the liquid crystalline phase for these polysaccharide nanocrystals.

ChNCs have an amine and amide functional groups in addition to hydroxy groups and as such offer additional interesting routes for chemical modifications in comparison to CNCs. The possible routes take advantage of this property are addressed in more detail in Section 3.5.

Lastly, there are other interesting findings where chitin outperforms cellulose, and these are, where appropriate, mentioned in the text that follows.

3.2 ChNC preparation

3.2.1 Hydrolysis in hydrochloric acid

The most common preparation strategy to convert chitin into ChNCs employs acidic hydrolysis in hydrochloric acid (HCl). In general, chitin is hydrolysed at 2.5 - 4.0 M HCl at temperatures varying from 90 to 104 °C (i.e., reflux) for 1 to 6 hours. [8, 10, 21, 23–25, 33, 61, 120–123, 123–139] While many studies successfully prepare discrete ChNCs dispersed in an aqueous solvent, there is a considerable variation in reported nanoparticle size and shape. Although ChNCs polydispersity in size can contribute to this variation, even

the average values fluctuate: 200-800 nm in length and 3-60 nm in width; this is despite the apparently similar preparation conditions used in the process, making it virtually impossible to disentangle the relationship between the slight alterations to the reported preparation conditions and nanoparticle characterisation. The difficulty in characterising ChNCs by means of TEM and AFM complicate the extraction of meaningful relationships between preparation conditions and resulting properties. In fact, the issues with characterisation of polysaccharide nanoparticles are now recognised in the established field of CNCs and efforts to standards the methodologies are emerging. [140–142] Additionally, the nature of the manuscripts for publishing does not encourage negative results or issues despite their usefulness; such accounts are only rarely reported, e.g., a notable material sedimentation after ChNC preparation at commonly used conditions. [33] Moreover, there appears to be conviction in the literature that 3.0 M HCl concentration is optimal in preparing ChNCs, in spite of the lack of studies on the effects of acid concentration on ChNC properties. Given that chitin dissolves only above 8.0 M HCl aqueous solution,[143] the hydrolysis at higher acid concentrations than 3.0 M (or lower) could produce useful ChNCs with unusual physical properties.

3.2.2 Alternative methods

The use of sulphuric acid, which is commonly used to prepare CNCs, has only been recently reported to be suitable to ChNCs. [144] The reaction conditions employed were much milder: 3.0 M H_2SO_4 at 95 °C for 12 hours in comparison to 64 wt% H_2SO_4 at 60 °C, 1 hour used to prepare CNCs. [115] On the other hand, using sulphuric acid concentration of 64 wt% can also be used to prepare ChNCs, however, the STEM images presented, under closer inspection, show a significant number of bundles and aggregates. [145–147]

Seemingly more sustainable, yet more expensive, routes employ oxidation reactions. The radical catalyst 2,2,6,6-tetram-ethyl-piperidinyl-1-oxyl (TEMPO), in combination with NaClO and NaBr, can act as a co-oxidant in a reaction converting the primary hydroxy into the carboxy moiety. [148] When the degree of oxidation, adjustable by NaClO/chitin ratio, becomes sufficiently high, a large number of carboxy groups provides a strong enough electrostatic repulsion for mechanical agitation to be able to break chitin into well dispersed ChNCs. Such a TEMPO-mediated oxidation allows to obtain 15 nm wide and 270 nm long ChNCs on average. [148] However, extremely high surface charge values are required to prepare ChNCs in this way; lower oxidation values produce chitin nanofibers (i.e. extremely long and aggregated fibrils of chitin). A variation of the TEMPO based system, involves a laccase enzyme to produce carboxylated ChNCs. [149] Due it its large size, chitin cannot access the active site of the laccase enzyme, but TEMPO is able to mediate the electron

transfer to oxidize chitin primary alcohol. An alternative milder approach utilized ammonium persulfate as an oxidant without the need of TEMPO to prepare carboxylated ChNCs, offering a more sustainable and economical route. [147] Lastly, even hydrolysis of mechanically-defibrillated chitin in H_2O_2 was shown to be able to prepare carboxylated ChNCs, which may become a more sustainable route in the future. [150]

A high surface charge, that facilitates conversion of chitin into ChNCs, can be also obtained by partial chitin deacetylation. [44] When controlled deacetylation is carried out, only surface amides to amines are converted, and at acidic pH the resulting large number of the amino groups provided a positive surface charge sufficiently large for mechanical agitation to break chitin into discrete ChNCs. This methodology, in principle, is analogous to carboxylation methods presented above, however, while carboxylation provides a negative surface charge, deacetylation gives rise to a positive surface charge. Nevertheless, the surface charge values are relatively large and may not be conductive for liquid crystalline behaviour of such ChNCs. Using lower surface charges, however, usually leads to production an entangled network chitin nanofibers or barely de-fibrillated chitin.

An alternative greener and more sustainable approach utilises deep eutectic solvents, composed of choline chloride and organic acids, to produce ChNCs. [151, 152] While the research in the use of such solvents is only now emerging, by altering the solvent systems and reaction temperature, the average produced ChNCs could be tuned to have the average length from 250 to 750 nm, and the average diameter of 45 nm. [151, 152] While the self-assembly properties of so prepared ChNCs have not been investigated yet, they were shown to be promising in stabilizing emulsions.

It is noteworthy to stress that virtually all the work related to chitin nanocrystals (ChNCs) is performed using crustacean derived chitin, which is partially because of its facile commercial availability. However, a significant variability in chitin physical properties originating from the chitin source can be expected, which is also supported by studies on CNCs produced different sources. [19, 31] The reports regarding ChNCs prepared from insects are virtually absent despite their abundance in variety and biomass. [118] In contrast, chitin and chitin nanomaterials extracted from fungi have started to grow in popularity, with exciting properties such as chitin nanopapers produced from fungi showing superior tensile properties compared with the crustacean derived analogous. [153–156] However, only a single study to date, have prepared actual fungal ChNCs. [157] The nanoparticles were prepared via acid hydrolysis at 3.0 M HCl at reflux for 90 minutes, and the resulting fungal ChNCs were reported to be 143 ± 24 nm long and 10 ± 2 nm wide, however, TEM images provided appear to be over-crowded and images at lower magnification indicate a lot of nanoparticles which are 1-2 μm long. Nevertheless, the use of such fungal ChNCs as a liquid crystalline material

was not explored, yet these results suggest that unique liquid crystalline properties can be expected.

3.2.3 CNC preparation

In contrast, the field of CNC research is well advanced, partly because of the studies, where the cellulose source, reaction temperature, duration, acidity. and the post treatment by tip sonication were systematically investigated and related to the physicochemical and self-assembly properties. First of all, it is well established that different sources of cellulose (e.g., cotton, wood pulp, ramie, etc.) will result in different sizes and shapes of CNCs even under comparable experimental conditions. [31, 32, 115, 158] When the same cellulose source is used, increasing reaction duration from 10 to 240 minutes, while keeping the temperature constant at 45 °and sulphuric concentration constant at 64 wt %, the CNCs produced decreased in length from 390 nm to 177 nm. [115] The reduction in length was most prominent during the initial 60 minutes of the reaction, followed by levelling off. The suspension, which was prepared by hydrolysis for only 10 minutes, was deemed to be underhydrolyzed, as it did not exhibit liquid crystalline properties. [115] Increasing acid to cellulose ratio is another strategy to reduce the average length of the CNCs. [32] By increasing the reaction temperature, the reaction ran a risk of over-hydrolysis (i.e., cellulose turning black) and similar results could be achieved by simply adjusting the reaction duration. When the reaction duration was fixed to 30 minutes, and temperature altered from 45 to 72 °C using 65 wt% sulphuric acid, the nanoparticle length shifted from 141 to 105 nm. [31] When considering these results, it is important to note that when applying apparently equivalent CNC preparation methods (45 °C, 64 wt% sulphuric acid, 30 minutes, cotton as cellulose source), the average reported values in two separate studies were 141 nm and 276 nm. [31, 115] The differences in the average values could originate from different tip sonication treatments and differences in sample preparation for TEM imaging and the result analysis. In fact, the energy input by tip sonication drastically reduces CNC dimensions, improving their dispersibility; however, there were associated increase in conductivity and decrease in pH, which are difficult to explain. [65, 75] Ultimately increased tip sonication application, resulted in self-assembly at higher concentrations and larger chiral nematic pitch, resulting in red-shifting in reflectance of the produced solid-state films. The surface charge of CNCs results from the sulphate half-ester groups which are grafted during the hydrolysis in sulphuric acid: in general, it is observed that the harsher reaction conditions lead to higher surface charge, independently of the other mentioned changed. Lastly, a recent study showed that by repeated separation of the anisotropic and isotropic phases, in different fractions the average nanoparticle size and their polydispersity can be tuned. [40] This approach allowed

to alter nanoparticle dimensions, while maintaining constant surface charge, which is not the case when the reaction conditions are changed. [31, 32, 115, 159]

Overall, these studies show that by altering the reaction conditions, the physical dimensions of CNCs can be tuned and as a results their ability to self-assemble into a chiral nematic state. Even with these optimisation studies, there is still a great variation in the CNCs that are commercially available despite apparent similarity in their reported preparation conditions. [142] Some of the issues originate from the inherent difficulty in characterising the material and, therefore, the standards are becoming to emerge. [140, 141] It is worth noting, that the concept of ideal CNCs, as well as ChNCs, is difficult to apply as it not only depends on the intended material use but, even for self-assembly applications, the "best" combination of physicochemical parameters is difficult to tell. If the material is intended to be used in lubricants, Pickering emulsions, or polymer fillers, a high yield may be chosen at the expense of dispersibility. On the other hand, for the liquid crystalline studies, it may be tempted to aim for completely individualized nanoparticles, however, the nanoparticle bundles may be critical in forming the chiral nematic liquid crystalline state. [160] Nevertheless, it is clear that cellulose needs to be sufficiently hydrolysed for it to be colloidally stable and to start forming liquid crystalline state. [115] In addition, even for the applications relying on self-assembly, depending on the nanoparticle properties larger or lower chiral nematic pitches can be attained or the development of the liquid crystalline phase can occur at lower or higher concentrations. [7] In essence, the ideal combination of parameters for ChNCs or CNCs should be considered synergistically to adapt the system for the desired application, yet liquid crystalline properties of CNCs and ChNCs are not fully understood and, in the case of ChNCs, the in-depth studies on ChNC preparation conditions relating to colloidal and liquid crystalline properties need to be done for such a selection to be possible.

3.3 Liquid crystalline properties of ChNCs

While there are numerous reports demonstrating the successful production of ChNCs, only a handful investigates their liquid crystalline properties. [8, 10, 24, 33, 61, 137, 161] The most notable researchers who shaped the current understanding of ChNC self-assembly are R.H. Marchessault, J.-F. Revol, J. Li, and E. Belamie. Even in these magnificent pieces of work, there is an unexplained variation in preparation in methodology with 2.5-4.0 M HCl at 90-104 °C and 90-180 minutes duration being used. Nevertheless, the preparation conditions generally yielded discrete ChNCs polydisperse in size, ranging from 50 to 300 nm in length and average width of 7 nm. ChNC suspension prepared in this manner were shown to separate into isotropic and chiral nematic phase at various nanoparticle concentrations,

which depended on pH and ionic strength, though the concentration range of interest was within 2 to 10 wt%. The effect of ionic strength and pH are much better explored in terms of the phase separation, while their effect on the chiral nematic pitch was not studied in depth, i.e., it was shown that by varying pH the chiral nematic pitch can be tuned from 250 µm to 20 µm in liquid state. [33] The values are significantly larger than what is attainable with CNCs, where 80-5 µm are normally achieved. [7, 46] Interestingly, only a single mention, to the best of our knowledge, exists on the possibility to retain the helicoidal architecture in the solid state upon ChNC evaporation: a drop of ChNC suspension upon drying showed a helicoidal pitch of 5 µm, [10] which is significantly larger than what has been reported for CNC films. [7, 46] Given the extremely large pitches achievable using ChNCs but not CNCs, it opens a niche for its exploration as a functional material. In addition, it poses the question whether the structural colouration readily obtainable using CNCs, can ever be obtained using ChNCs as well as whether there is a fundamental difference between ChNC and CNCs that results in such a large difference in the chiral nematic pitch as noted above. [162]

Overall, a handful of publications on ChNC self-assembly shows a stark contrast with a vast literature and numerous research groups working on CNC self-assembly, where the effect of material sources, preparation conditions, formulation parameters, additives, and miscellaneous treatments have been studied in function of CNC self-assembly for years and are well reviewed. [7, 46, 163] Although the general principles of self-assembly learnt from CNCs can be applied to ChNCs, there are plenty of differences which are not trivial to account for (e.g., significant differences in nanoparticle size, surface charge and its nature, preparation conditions, formulation parameters, chiral interactions in chiral nematic among many more). Therefore, in order to move forwards with preparing functional ChNC materials and to probe fundamental questions about the nature of self-assembly, it is imperative to establish to study ChNC self-assembly directly, for which the relationship between ChNC preparation conditions and their colloidal and liquid crystalline properties need to be established. It is worth mentioning that due to the lack of understanding it is not clear whether longer or shorter, more or less charged nanoparticles will assemble with larger or smaller pitch and more or less homogenous structure.

3.4 Other interesting applications of ChNCs

Beyond their ability to self-assemble, ChNCs are interesting for a number of other properties, with their ability to stabilise oil/water emulsions being worth a mention. [164–167] The food, cosmetics, and pharmaceutical industries heavily rely on emulsions in their products and while conventional molecular surfactants are still heavily used, a different type of

emulsions, known as Pickering, offer better stability even at low particle loading because of the irreversible adsorption of nanoparticles at interfaces, allowing to use smaller amounts of the stabilizer and thus making products not only cheaper but also more environmentally friendly. [139] In this respect, ChNCs have been shown to effectively stabilize oil/water emulsions, with factors such as nanoparticle size, surface charge, and formulation variables (i.e., ionic strength and pH) being important. At optimized conditions, ChNCs have surpass all the previously reported bio-based nanoparticles, even cellulose based ones, at emulsion stabilisation. [164]

Furthermore, emulsions prepared using ChNCs can be processed to produce porous functional aerogels. [168–170] Highly porous ChNC aerogels can then be carbonized to produce porous carbon, with a large surface area, which is a promising material as filter media, electric double-layer capacitors and highly efficient catalysts. [170] Aerogels and hydrogels made of ChNCs have also showed an exceptional performance in catalysing the aqueous Knoevenagel-condensation reaction. [171] The catalysis was chitin specific, as cellulose based analogous aerogels showed no catalytic activity.

Hydrogels can also be produced using ChNC suspensions. [172] One approach is to expose the suspension to ammonium vapor to quickly turn it into a gel. [161] Interestingly, this method can be used to prepare ChNC hydrogel with the chiral nematic architecture, which was used to explore of producing mechanically anisotropic composite materials by performing *in-situ* biomineralization of $CaCO_3$. This approach inspired by biomineralization is promising for the design of mechanically stable inorganic/organic hybrid materials and indicates the scope for such hydrogels for *in-situ* synthesis of, e.g., plasmonic nanoparticles in a chirally structured template.

ChNCs have been used in nanocomposites with synthetic polymers as a matrix. For example, a successful incorporation of ChNCs into latex of unvulcanized and prevulcanized natural rubber improved the mechanical performances of the composite. [122, 173] The improved mechanical performance depended on the distribution of ChNCs and their interfacial interaction with the matrix. In fact, ChNC were successfully incorporated in various polymer matrixes, e.g., poly(styrene-co-butyl acrylate), poly(caprolactone), soy protein isolate, poly(vinyl alcohol), chitosan, silk fibroin, alginate, starch, hyaluronan-gelatin, and waterborne polyurethane. [21, 139, 153]

Using ChNCs, a bio-inspired material was produced by adapting the strategy used by barnacle to adhere to rocks. [109] The adhesion originates from the specific chitin and protein interactions, which was mimicked by mixing ChNCs with hen egg white lysozyme in its amyloid form, resulting in bio-colloidal green adhesives. [109]

Lastly, ChNCs can serve well as a scaffold for enzymes. For example, porcine pancreatic lipase (PPL) can be linked onto ChNC surface. [174] Not only it allowed the expected reduction reaction to happen, attachment to ChNCs proved to make the enzyme less sensitive to pH and temperature, when compared to a free enzyme. [174] The use of ChNCs as a scaffold for enzymes also allowed easier retrieval of the enzyme after use.

3.5 Potential for ChNC chemical modifications

Chitin present a number of ways that it could be chemically modified to improve the material performance. Interesting properties which could be modified include metal ion binding, solubility in various solvents, thermal and mechanical durability, and altered self-assembly. A number of reaction may be used to functionalise chitin, thanks to the hydroxy and amine functional groups exposed to the fibril surface. The amine group is especially interesting as gives opportunities to perform reactions not readily available with cellulose. The reactions that could be carried out include a number of traditional reactions such as deacetylation, acylation, N-Phthaloylation, tosylation, alkylation, Schiff base formation, reductive alkylation, carboxyalkylation, silylation, sulphonation. [137, 175] A few reaction groups will be reviewed in more detail, though for a much more expansive introduction to the topic, the reader is directed to specialised excellent reviews on the topic. [102, 175–178]

The first thing to consider though is that chitin is insoluble and so most of the reactions must be carried out heterogeneously. Insolubility may result in problems with controlling the extent of the reaction, distribution of the modifications and may especially be an issue when working with polymer grafting onto chitin. [176] The chemical surface modifications of ChNCs are much more promising because of their high dispersibility and large surface area. While the number of hydroxy groups is fixed, the number of amine groups can be tailored by a process called deacetylation - a most commonly encountered chitin chemical modification.

3.5.1 Deacetylation

The most obvious modification that can be done on chitin, and thus ChNCs, is their deacetylation using a strong alkali. [25, 175] Chitin can be completely deacetylated when subjected to 40-50 wt% alkali (e.g., NaOH, KOH) at 80-160 °C for several hours. [15, 102, 175] Chitosan prepared in this way has virtually all of the amides hydrolysed (or deacetylated) to amines, making the polymer highly soluble in acidic aqueous condition and serving as an important polysaccharide for many studies of chemical modifications. In contrast, partial deacetylation can be achieved at 20-30 wt% of alkali where only the surface amides are relatively slowly

hydrolysed into amines. [24, 25] Though the degree of deacetylation levels off to about 40 %. Not only deacetylation allows to easily increase the surface charge of ChNCs, but also provides additional sites for interesting chemical modifications.

3.5.2 Schiff base formation

The Schiff base formation refers to reactions, where amines and carbonyls react to form imines. These reactions usually take place under mild conditions and the imine formed can then be easily reduced with mild reducing agent such as sodium cyanoborohydride or a slightly more aggressive but less selective sodium borohydride. [176] This pathway allows to selectively produce a variety of N-alkyl derivatives. [102, 175–177] One of the examples uses Schiff base formation in reductive amination reaction to produce a secondary (more nucleophilic) amine, followed by direct alkylation to produced quaternized amines on chitosan to make them charged irrespective of pH. [179]

Schiff base formation can also be used to protect more reactive amine groups so that the reactions would take place on hydroxy groups. Aldehydes, and especially N-aryl aldehydes, work great at protecting amines and thus making only hydroxy groups accessible for reaction. The deprotection can then be carried out at acidic pH, giving O-substituted chitosan derivatives with free amine groups, which help with solubility at acidic pH. [176]

3.5.3 Click chemistry

Click chemistry refers to a set of near perfect reactions, in which two components exclusively react with each other, and are less traditional reactions, which usually quick, occur at low temperatures and moderate pH values as well as give high yield and are insensitive to water and oxygen. [176] Such reactions include cycloaddition reactions (e.g., Huisgen reaction, hetero-Diels-Alder reaction), nucleophilic ring-opening reactions in strained heterocyclic electrophiles, carbonyl chemistry of the non-aldol type, and additions to carbon-carbon multiple bonds. Using click chemistry, chitosan derivatives with tunable thermosensitive, photochromic, pH-sensitive, solubility properties can be prepared. [176, 180, 181] For example, copper-catalysed azide-alkyne [3+2] cyloaddition reaction can be used to attach various functional moieties to chitin and chitosan after amine was converted to azide. [178]

Click chemistry is highly used in grafting polymers onto chitosan backbone. These reactions allows to selectively obtain N- or O-grafted chitosan-g-poly(ethylene glycol). [102, 175–177] PEGylated chitosan has been considered as a bioactive delivery carrier for insulin, DNA, heparin, and albumin, among other. [102, 175–177] In addition, click chemistry can be an excellent tool, which was shown to be useful in grafting various homopolymers grafted

onto the chitosan backbone, such as poly(N-isopropyl acrylamide), β-cyclodextrin (on O-6 position or the amine), poly(caprolactone), and others. [102, 175–177] For example, this approach was used to produce chitosan-poly(ethylene glycol) hybrid hydrogel microparticles, which were then conjugated with single-stranded DNAs via click chemistry via amine. [182] There are other chitosan derivatives developed via click chemistry reactions, exhibiting properties like antimicrobial, antifungal, enhanced solubility in acidic and basic conditions, antigen detection, coupling to graphene sheet and chitosan functionalized multi-walled carbon nanotubes. [176]

3.5.4 Inspiration from protein chemical modifications

A lot of inspiration for chemical modifications of chitin and chitosan can be drawn from protein and peptide chemistry as these reactions are often conducted on amines (via lysine) in aqueous and mild conditions required not to damage the protein. [183–185] In addition, the reactions are made to be chemoselective due to the presence of many alternative reactive functional groups (e.g. -SH, -OH). Possible reactions via amine can occur with electrophilic reagents such as activated acids, vinyl sulfones, sulfonyl chlorides, iso(thio)cyanates, and squaric acids. Alkylating chemicals, such as cyclohexene sulfonamide derivatives, can be used for the site-selective labelling of lysine in human serum albumin (HSA). [183] Indeed, the modification of amine on lysine is often the first of reaction, followed by a second bioorthogonal reaction (e.g., click chemistry). For example, a 6π-aza-electrocyclization reaction can be used for the asymmetric synthesis of pyridine/indole alkaloid-type natural products onto proteins. Another method for selective lysine chemical modification involves the use of 2-imino-2-methoxyethyl reagents (IME) through the formation of an amidine linkage. [183] Lastly, amines can also be easily arylated using a palladium mediated reaction. [185]

The number of available chemical modification strategies of chitin, chitosan, and ChNCs by relying on the amine, provide the potential for required properties to be imparted onto material. It may be of particular interest to consider such reactions *in-situ* in ChNC hydrogels with the preserved chiral nematic liquid crystalline state. [161]

Chapter 4

Experimental section

4.1 Chitin purification

4.1.1 Shrimp chitin

As received, shrimp chitin (Shrimp shell chitin, practical grade, Sigma-Aldrich) had a yellow colour as well as a shrimp-like odour. Thus, before use it was purified by a modification of previously reported methodologies. [120, 186]

1. Acid bath. Chitin powder was stirred in aqueous HCl (0.1 M, Sigma-Aldrich) at room temperature for 6 hours. Solid to solution ratio was 1 g to 30 mL. The pH did not change as measured using pH-indicator paper. The chitin solids were washed thrice by centrifugation (25 kg, 4 °C, 30 min) with the pellet being redispersed between the successive runs in Milli-Q water (Millipore Milli-Q gradient A10, resistivity >18 Mω/cm) .

2. Base treatment. Chitin pellet was treated with aqueous NaOH (5 wt%, Sigma-Aldrich) with $NaBH_4$ (0.3 wt%, Acros Organics) at 80 °C for 3 hours while stirring. Solid to solution ratio was 1 g to 20 mL. The reaction mixture was quenched by dilution with Milli-Q water. The solids were collected and washed as above.

3. Bleaching:

   (a) Acidic bleaching. Chitin was stirred in aqueous $NaClO_2$ (0.3 wt%, Sigma-Aldrich) at 80 °C for 3 hours. Solid to solution ratio was 1 g to 15 mL. The pH $\approx$ 3 was maintained by drop-wise addition of glacial acetic acid which resulted in bright yellow colouration of the reaction mixture, which paled over time. The reaction mixture was then purged with N_2 gas while cooling down to room

temperature. The solids were collected and washed as above. This treatment was used for samples prepared in Sections 5.1, 5.2, 5.3.1.

(b) Basic bleaching. Chitin was stirred in H_2O_2 solution (2.5 wt%) at 80 °C for 3 h. The pH $\approx$ 10 was maintained by drop-wise addition of NaOH solution. The reaction mixture was then allowed to cool down to room temperature. The solids were collected and washed as above. This treatment was used for samples prepared in Sections 5.3.2.

After purification, chitin was pelleted by centrifugation and then dialysed against Milli-Q water changing it once per day (Regenerated Cellulose dialysis tubing, MWCO 12-14 kDa, Scientific Laboratory supplies). Dialysis was stopped when the conductivity of the dialysis bath did not change overnight. Chitin slurry was then concentrated to a pellet ($\sim$ 10 wt%) by centrifugation and kept in fridge at 4 °C.

4.1.2 Fungal chitin purification

Fungal chitin was isolated following an analogous protocol to shrimp chitin. The starting material was the common white mushroom, *Agaricus bisporus*, acquired form a local supplier. They were first washed under warm tap water to remove debris, then boiled in tap water for 1 hour and collected. They were then blended in tap water using a household stick blender, yielding a purée, which was further boiled in water for 1 hour. The solids were collected and pressed in a nylon cloth (40 µm mesh) to obtain a brownish-grey pulp. This was then subject to three rounds of base treatment and basic bleaching as described above for the purification of shrimp chitin.

After purifications, fungal chitin was pelleted by centrifugation and dialysed against Milli-Q water changing it once per day. Dialysis was stopped when the conductivity of the dialysis bath did not change overnight. Chitin slurry was then concentrated to a pellet ($\sim$ 10 wt%) by centrifugation and stored at < 4 °C.

4.2 Concentration measurement

All chitin and ChNC weight fractions were measured by drying three to five aliquots in the oven at 55 °C until the mass became constant (usually 12 hours was sufficient). The samples were allowed to cool down to room temperature in a desiccator before the mass was recorded.

4.3 Chitin hydrolysis to ChNCs

A never-dried, purified chitin pellet at a concentration of ∼10 wt% was preheated to around 70 °C. Aqueous HCl (37 wt%, Sigma Aldrich) was mixed with the required volume of Milli-Q water minus the water included in the chitin pellet, such that, a final HCl concentration of 3.0 (or 5.0) M was achieved once chitin pellet was swiftly mixed into refluxing premixed HCl solution. Although reflux was interrupted when chitin pellet was added, it started again within 2 minutes. Thorough mixing was obtained using a mechanical overhead stirrer set to ∼700 rpm. Final chitin solid to liquid ratio was 1 g to 30 mL. The reaction time was commenced from the addition of chitin pellet. After a given time (60 - 540 minutes, with typically 540 min being used), the reaction mixture was quenched by diluting it threefold with ice-cold Milli-Q water. The solids were then washed and collected by centrifugation as above. However, the solid pellet had to be vigorously shaken for a long time to completely resuspend it in Milli-Q water. The resulting suspension was then dialysed against Milli-Q water until the conductivity of the water bath did not change overnight. The resulting milk-white ChNC suspension was dialysed against HCl (e.g. 1.0 mM HCl aqueous bath was used for 1.0 wt% ChNC suspension placed in a dialysis bag) to achieve 100 $mmol_{HCl}/kg_{ChNC}$ until the dialysis bath conductivity stabilised over-night. The prepared suspension was subsequently stored at <4 °C. A drop of chloroform was added to prevent bacterial growth. The same procedure was employed for both shrimp and fungal ChNCs.

4.4 Tip sonication

ChNC suspensions were treated with ultrasound by tip sonication (Fisher brand Ultrasonic disintegrator, max power 500 W, tip diameter 12.7 mm). The machine was operated at 30 % amplitude and in pulse mode (on:off = 10:15 s). All the samples were tip sonicated at a ChNC concentration of 1.00 wt% in 200 ± 5 g portions. The container was kept in an ice bath throughout to prevent the heating suspension. The resulting suspensions were then filtered thrice through both 8.0 µm and 0.8 µm filter papers (SCWP, Merck Millipore Ltd., AAWP, Merck Millipore Ltd., respectively).

4.5 Chitin deacetylation

Purified chitin was freeze-dried and then deacetylated in aqueous NaOH (40 wt%, 95 °C, 4h) in the presence of $NaBH_4$ (0.6 wt%). The chitin to solution ratio was 1 g to 25 g. Thorough mixing was obtained using a mechanical overhead stirrer set to ∼700 rpm. The reaction was

quenched by threefold dilution using ice-cold Milli-Q water. The solids were collected and washed three times by centrifugation, as before. Deacetylated chitin was dialysed against Milli-Q water changing it once per day. Dialysis was stopped when the conductivity of the dialysis bath did not change overnight. The chitin slurry was then concentrated to a pellet ($\sim$10 wt%) by centrifugation and stored at <4 °C.

4.6 Chitin nanocrystal deacetylation

A chitin nanocrystal suspension at concentration of $\sim$10 wt% was extensively dialysed against Milli-Q. The sample was then preheated to 70 °C and mixed with aqueous NaOH solution heated to 90 °C. The final concentration of NaOH was 33 wt%. The ChNC to aqueous NaOH solution (33 wt%) ratio was 1 g to 50 g. The reaction time was varied in 1 hour intervals to react samples from 0 to 4 hours at 90 °C, with 0 hours indicating the sample which was quenched immediately after mixing the ChNC suspension with the NaOH aqueous solution. Once the reaction was finished, it was immediately quenched by three-fold dilution with ice-cold Milli-Q water. The solids were collected and washed three times by centrifugation as before. Deacetylated ChNC suspensions were dialysed against Milli-Q water changing it once per day. Dialysis was stopped when the conductivity of the dialysis bath did not change overnight. Then all the samples, at 1.0 wt%, were dialysed in separate dialysis bags but in the same dialysis bath to set the ionic strength and pH with 50 $mmol_{HCl}/kg_{ChNC}$.

4.7 Ionic strength and pH tuning

Ionic strength and pH were set by dialysis against a bath with precisely adjusted pH and ionic strength using HCl (1.000 M, Titripur) and NaCl (1.000 M, Sigma Aldrich, Analytical grade). The dialysis was performed by changing the dialysis bath water once per day until pH and/or conductivity remained unchanged over night which typically took 7 days. The concentration of ions, unless otherwise stated, is described using $mmol_{electrolyte}/kg_{ChNC}$ indicating that the ratio between ChNC and the electrolyte is maintained constant which imitates the drying scenario.

The samples, which were investigated for effects other than the ionic strength or pH, were dialysed in different dialysis bags but in the same dialysis bath at the same ChNC concentration which remained virtually unchanged after dialysis. This was done to ensure invariability in ionic strength and pH.

Fungal ChNC suspensions with different amounts of surface charge and ionic strength were prepared by adding pre-calculated amounts of NaCl and/or HCl into the suspension that had been thoroughly dialysed against Milli-Q beforehand.

4.8 Chemical composition characterisation

All the samples analysed for their chemical composition were freeze-dried and ground using mortar and pestle.

4.8.1 ssNMR spectroscopy

Cross-polarisation magic angle spinning ^{13}C nuclear magnetic resonance spectroscopy (^{13}C-ssNMR) was recorded at room temperature using an Ultrashield 400 spectrometer (Bruker) with a rotor spinning at 14 kHz. Glycine was used as a reference. Relaxation delay of 2 s and a contact time of 1 ms were used for the acquisition of the spectra. [23] The experiments were set up with the help from the members of Prof. M. Duer's research group, Yusuf Hamied Department of Chemistry, University of Cambridge.

4.8.2 Powder X-ray diffraction

The samples were analysed by powder X-ray diffraction with spectra recorded at 2θ angles from 5 ° to 50 ° at 40 kV, 30 mA (Empyrean powder diffractometer, Malvern Panalytical). Data was smoothed using the Savitzky-Golay method of third-degree polynomial with a window size of 51. [23]

4.8.3 FTIR spectroscopy

Fourier Transform Infrared spectroscopy transmittance spectra was collected in the 600 - 4000 cm^{-1} range with 128 repeats and 4 cm^{-1} resolution (Spectrum 100 ATR spectrometer, PerkinElmer).

4.9 UV-vis spectroscopy

UV-Vis spectra of ChNC samples were acquired at 1.0 wt% in a quartz cuvette in transmission from 200 to 800 nm (Cary 4000 uv-vis spectrophotometer)

4.10 Microscopy

4.10.1 TEM

Sample preparation and imaging

A drop of ChNC suspension at 0.001 wt% was deposited onto a glow-discharged carbon-coated copper grid. After 90 seconds, the excess liquid was absorbed by using a piece of filter paper. Then a drop of 2.00 wt% aqueous uranyl acetate solution was added onto the grid for 90 seconds. The excess liquid was again removed using a piece of a filter paper. The grid was then left in air to dry. The sample was observed using a Tecnai G2 transmission electron microscope (FEI corp.) operating at 200 kV. Micrographs were recorded with a CCD camera. *TEM micrographs were acquired by Yu Ogawa, Gea van de Kerkhof and the author of this thesis with the assistance of Heather Greer.*

ChNC size measurements

TEM micrographs were analysed using ImageJ software. [187] The length and width of at least 500 particles were measure manually. The average aspect ratio was calculated from the individual aspect ratio of every particle, defined as the ratio between its length and width. The graphs present average values as full circles with the standard deviations calculated directly from the raw data and presented as error bars.

4.10.2 SEM

Sample preparation and imaging

ChNC solid-state films were pulled laterally until they fractured. ChNC flakes were then attached on an aluminium stub coated with a conductive carbon tape. The flakes were oriented so that the obtained cross-section could be imaged by SEM. The samples were sputter-coated with a 10 nm layer of Au/Pd (Quorum Q150T ES). For every ChNC film, several flakes were attached to the aluminium stub. SEM was performed using Leo Gemini 1530VP (Zeiss, Germany), operating at high vacuum mode at 3-5 kV with a 3-5 mm working distance. The cross-sections which exhibited helicoidal (also known as Bouligand) structure were analysed using ImageJ software, [187] The pitch was defined as twice the observed periodicity. The reported pitch is an average of measurements taken from several different flakes.

4.10.3 AFM

Atomic Force Microscopy (AFM, Agilent 5500 SPM) with an AFM tip (OTESPA-R3) was used to acquire the images. A square of MICA (1-4 cm^2) was glued onto the glass slide using a double-sided tape. Using a scotch tape MICA was freshly cleaved. ChNC sample (150 µL, 0.001 wt%, pH = 3) was deposited and incubated for 3 minutes before it was washed off with 1 mL of Milli-Q followed by drying with N_2 gun. Then so prepared sample were then further dried in the oven for 30 minutes at 50 °C. AFM raw data was analysed and processed using Gwyddion 2.8. [188]

4.10.4 Optical microscopy

All optical microscopy was performed using a customised microscope (Zeiss, Axio Scope A.1) (Figure 4.1).

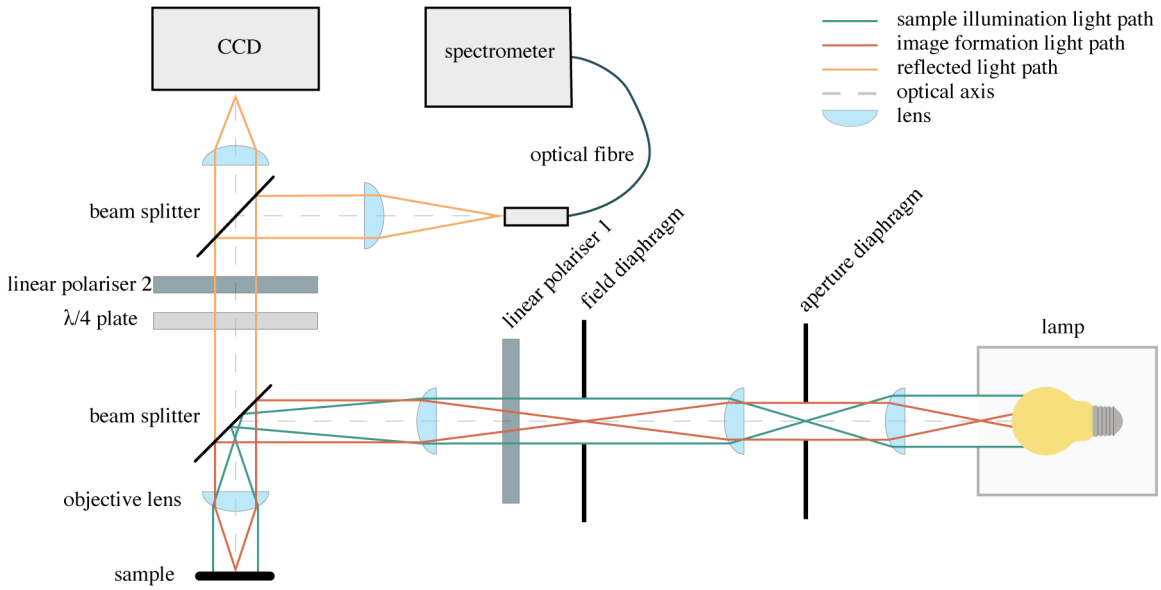

Figure 4.1 Polarised optical microscopy set-up. Crossed-linear polarisation measurements in reflection were acquired by only employing 1st and 2nd linear polarisers rotated perpendicular to each other. Reflectance of LCP/RCP light was measured by employing only the 2nd linear polariser and quarter-wave plate (abbreviated $\lambda/4$) rotated 45 ° to each other. Additional rotation of quarter wave-plate by 90 ° allowed to select the reflected of LCP or RCP light only.

For reflection measurements, bright-field imaging was employed with a 10x objective (Zeiss EC Epiplan-Apochromat 10X/03 HD DIC 422642-9960). The microscope was aligned before every session. [189] A halogen lamp (Hal 100) was used as a light source. The images were recorded with a CCD camera (UI-3580LE, IDS). The colour balance was set

against a standard white diffuser. Reflection spectra was collected using a spectrometer (Avantes, Ava-Spec-HS2048) which was coupled in using various standard optical fibres (e.g. FC-UV050-2 1305018). Spectra were normalised to the silver mirror (0.450 - 20 μm wavelength range, PF10-03-P01). Plotted spectra were smoothed using Savitzky-Golay method of third-degree polynomial with window size of 51.

Polarised optical microscopy in reflection with the sample placed between two crossed-linear polarisers (xLinP) was carried out using two perpendicularly arranged linear broadband wire-grid polarisers (WP25M-UB, Thorlabs) (Figure 4.1). The quarter-wave plate was not used for these measurements. Measurements in transmission were carried out in an analogous manner with the optical components and the light source, before the sample in reflection mode, being arranged below the sample. A super long working distance objective of 20X magnification was used (Nikon T Plan SLWD 20X/0.30, Japan).

Polarised optical microscopy with the selection of LCP or RCP reflected light was carried out by arranging linear polariser 2 at 45 ° to the quarter-wave plate ($\lambda/4$) via motorised controllers (Figure 4.1). The discrimination between LCP and RCP light was achieved by rotating the quarter-wave plate by 90 ° using a motorised controller. Linear polariser 1 was not used for these measurements.

Reported reflection spectra are selected to show typical measured spectra. For Figure 6.7 and Figure 6.6 average values of the peak positions are presented from at least 5 different recorded spectra.

4.11 Casting solid ChNC films

ChNC dry films were prepared by drying ChNC suspensions (4.0 g of 2.0 wt%) in a polystyrene Petri dish (35 mm inner diameter). Petri dishes with ChNC suspension were stored in a plastic box covered with a perforated lid. It took around 7 days for the suspensions to dry to form solid films.

4.11.1 Casting films on magnets

Some films were cast using magnets. Two different configurations were employed. Fungal ChNC suspension was dried in a Petri dish placed in-between two nickel-plated neodymium magnets (NdFeB, ref. F390-N42) of opposite polarity. Shrimp ChNC suspension (7.0 g, 2.0 wt%) was dried on a glass coverslip (Thermo Scientific Gold Seal, 48 x 65 mm, No. 1) which was cleaned before with concentrated sulphuric acid for 1 hour and washed with Milli-Q.

The coverslip was placed on the polymagnet (NdFeB, ref. 1000323, polymagnet) until the suspension dried completely.

4.12 ChNC film deacetylation

ChNC films were deacetylated by immersing them in an aqueous NaOH (50 wt%) solution, at 90 °C for 8 hours. Treated ChNC films were then extensively washed with Milli-Q water until neutral pH and left to dry at ambient conditions in polystyrene dishes.

4.13 Colloidal properties

4.13.1 Dynamic light scattering and zeta potential

Suspensions were characterised at 0.1 wt%, 21 °C, pH $\approx$ 3.0 (Zetasizer 3000, Malvern Instruments).

ChNC size was assessed by measuring Z-average in 3 repeats with 50 runs each. The graphs report Z-average values measured values and include the standard deviation, depicted as error bars. The standard deviation was determined by from the fitted normal distribution to the fitted normal distribution curve to the intensity data.

ζ-potential was measured using the Smoluchowski correction function, by performing three repeats with 50 runs each. The graphs are used to report average values with the standard deviation, provided by the original software, are depicted as error bars.

4.13.2 Conductometric titration

A precisely weighed amount (at least 10 g) of ChNC suspension at 1.00 wt% was transferred into a three-neck round bottom flask. 90 g of Milli-Q water was added. The suspension was stirred and then 0.5 mL of HCl (1.000 M, Titripur) was added followed by 50 µL of 500 mM NaCl solution. Conductivity measurements (InLab 752-6MM, Mettler Toledo) and the mass of NaOH solution (0.1000 M, Titripur) were recorded after every addition.

Alternatively, an automated titration system was also implemented (Metrohm, Dosing unit 807, 856 Conductivity Module). It was conducted in an analogous manner as the manual titration apart from the incrementally additions of NaOH (10 mM, Titripur). The two methods were consistent in the obtained experimental values.

The graphs report the measured conductometric value with the error bars depicting an estimated uncertainty of ± 20 mmol/kg to account from uncertainty in the concentration of ChNC suspensions, and NaOH, HCl solutions used in the experiments.

4.14 Liquid crystalline properties

4.14.1 Preparation of dilution series

ChNC suspensions were concentrated using a rotary evaporator operating at 55 °C, ∼20 mBa. To prevent ChNC skin formation on the flask, a hydrophobic perfluoroalkoxy alkane (PFA) flask was used. The skin would still form at higher ChNC as the viscosity increased and so it had to be closely monitored.

A concentration series was prepared by diluting a concentrated stock ChNC suspension with Milli-Q water to achieve the desired concentrations. Therefore, every point from the dilution series had a fixed ChNC to NaCl/HCl ratio. This approach allowed to replicate the conditions experienced by the ChNC suspension during drying to form a solid-state ChNC film.

4.14.2 Phase diagrams

ChNC suspensions, from the concentration series, were drawn into round glass capillaries (1.3 mm inner diameter). When capillary forces were insufficient, a low vacuum pump was applied to the end to draw in the suspension. The capillaries were sealed from both sides with nail varnish or candle wax. Capillaries were then left to stand vertically for a month to ensure that the phase separation had reached an equilibrium. Any changes in ChNC concentration due to water evaporation were corrected by comparing to lines, indicating the liquid-air interface, drawn on the capillary sealing day. Overall, the capillaries have an air gap at the bottom and top of the capillary and a ChNC suspension in-between, where the anisotropic phase sediments to the bottom of ChNC suspension when and if the anisotropic phase is formed.

Phase diagrams were obtained by observing the glass capillaries filled with ChNC suspension between crossed linear polarisers with back illumination (Figure 2.5 A). The photographs were taken with a standard camera (Nikon D3200, AF-S DX NIKKOR 18-55 mm f/3.5-5.6G VR lens) and further analysed using ImageJ software. [187] The anisotropic volume fraction was taken as the ratio between the height of the bright region and the height of the whole suspension. The graphs report values from a single series of experiments, except for experiments used to study hydrolysis conditions, where the average of three analogous

series is presented. The variation in the volume fraction in the anisotropic phase formed had 0-5 % standard deviation and therefore not included.

4.14.3 Pitch diagrams

Pitch diagrams were constructed by analysing the aforementioned capillaries by polarised optical microscopy (POM). Capillaries were placed between two crossed-linear polarisers in transmission and perpendicular to the observation direction. A super long working distance objective with 20X magnification (Nikon T Plan SLWD 20X/0.30, Japan) was used to observe the chiral nematic texture with the helix axis perpendicular to the viewing direction (Figure 2.5 B, C). No significant flow was observed when the capillaries were placed horizontally for imaging. At least 5 images were taken from the top to the bottom of the anisotropic phase for each capillary. To measure the chiral nematic pitch, the images were manually analysed using ImageJ software. The periodicity of the observed fingerprint pattern was taken to be equal to half the chiral nematic pitch. The graphs report average values with the standard deviations being typically 5-10 %, which are not included not to over-clutter the graphs.

Chapter 5

From chitin to chitin nanocrystals

Generally, the phase separation of rod-like polyelectrolytes such as ChNCs and CNCs depends on five parameters: the dimensions the particles, the shapes of the particles, the polydispersity in particle size, the surface charge, and the ionic strength of the system. [52, 58, 115] The first four parameters strongly depend on the nanoparticle preparation conditions, which are not well understood in the case of ChNCs. Therefore, for ChNCs to become regarded as an advanced functional and sustainable material, a good control over the ChNC properties need to be attained, much like was achieved with CNCs (c.f. section 3.2.3). The conversion of chitin to ChNCs typically involves three key processing steps:

- Acidic hydrolysis: to convert chitin into ChNC.
- Tip sonication: to disperse aggregates.
- Deacetylation: to control surface chemistry/charge.

Each step can have significant effects on the behaviour of the resultant ChNC suspension and as such they need to be studied and optimised synergistically. Thus, in this chapter the role of each step on colloidal and liquid crystalline properties is studied in detail, with key parameters explored systematically. The reaction temperature was kept constant throughout as it is more difficult to control, and it showed minimal difference in dimensions in CNC studies. [159] The reaction duration was varied from 90 to 540 minutes to span over a long range, and it is expected from CNC studies that the reaction starts to level-off. [115] Two different HCl acid concentrations were studied (3.0 and 5.0 M) since 3.0 M HCl has been used numerous times in successfully producing ChNC and a higher 5.0 M concentration to understand its effects (at c.a. 8.0 M HCl chitin dissolves). [10, 143] Three tip sonication times in large intervals were chosen to assess the effect that it will have on ChNC dimensions as it was demonstrated before to influence CNCs. [75] The effect of the increased surface

Table 5.1 A summary of ChNC suspensions prepared by various hydrolysis conditions. Tip sonication time was applied to 200 ± 5 g of suspension at 1.00 wt%. *5M270 sample showed significant discoloration, implying unwanted degradation or side-reactions, and, as a result, was excluded from further studies.

Sample name	[HCl] (M)	Duration (min)	Temperature (°C)	Tip sonication (min)	Yield (by weight)
3M90	3.0	90	104	4.5	88
3M270	3.0	270	104	4.5	79
3M540	3.0	540	104	4.5	70
5M90	5.0	90	104	4.5	75
5M180	5.0	180	104	4.5	65
5M270*	5.0	270	104	N/A	N/A

charge on the self-assembly was studied by using a controlled deacetylation reaction, which cannot be studied using CNCs due to the origin of the surface charge. Lastly, given that there is a significant variation in CNC physical dimensions based on the cellulose source, [31] ChNCs were prepared using shrimp and mushroom as a starting material.

5.1 Acidic hydrolysis

Acidic hydrolysis is the first and most crucial step in converting chitin fibrils into ChNCs. Reaction conditions such as acidity, duration, temperature, and reactant ratio can all have an effect on the physical attributes of the resultant ChNC colloids. With many variables to control, the reaction acidity and reaction duration were selected to be the key conditions to investigate. These were selected as they can be directly controllable as well as the acidity is expected to dominate the kinetics of the hydrolysis while the duration allows to probe different stages of this reaction. In contrast, the reaction temperature (reflux at 104 °C) and acid to chitin ratio (30 mL acid per 1 g chitin) were kept constant. This resulted in a series of six samples prepared from different hydrolysis conditions (Table 5.1). To maintain consistency, all the samples were post-processed following an identical procedure, namely tip sonication to aid colloidal dispersion (i.e., 4.5 min) and at a defined ionic strength and pH (i.e., 100 $mmol_{HCl}/kg_{ChNC}$).

5.1.1 Chemical composition

During hydrolysis, the white chitin slurry developed an off-white colour which, to an extent, persisted through to the final ChNC suspensions (Figure 5.4 A). However, 5M270 sample turned dark brown-grey which suggested a significant degradation of chitin crystalline

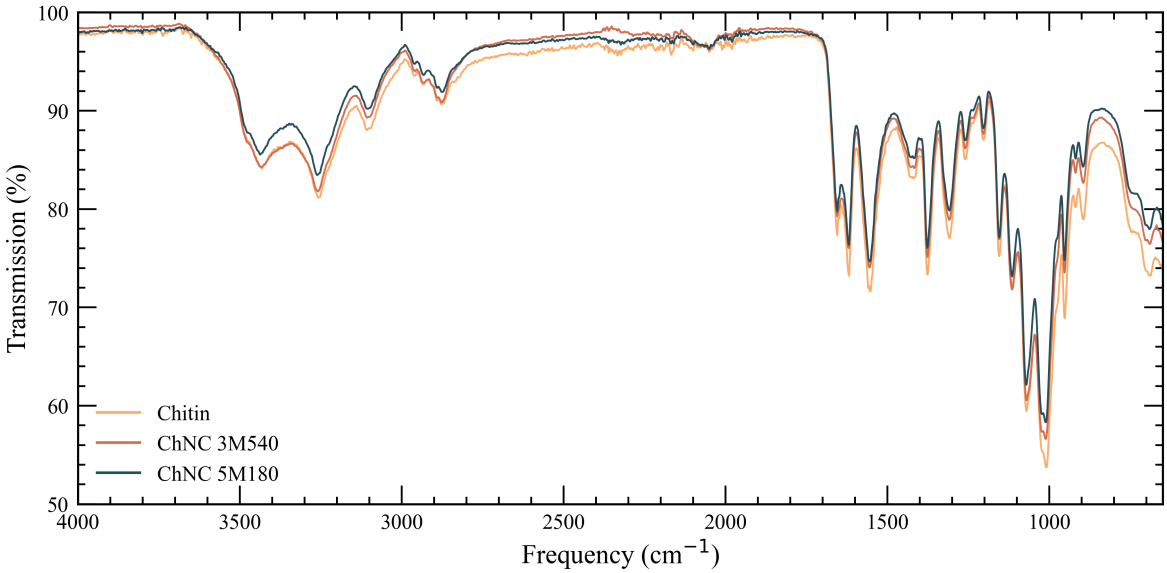

Figure 5.1 FTIR spectra of initial chitin and ChNCs. Vibrational stretches prove that the original material as well as the prepared ChNCs are chemically comparable and consistent with α-chitin structure.

structure or accumulation of side-reaction by-products. Consequently, it was excluded from further studying. Nevertheless, purified chitin along the ChNC samples of the most extreme conditions from each series, namely 3M540 and 5M180, were analysed for their chemical composition.

Fourier-Transform Infrared (FTIR) spectroscopy was used to assess the reaction outcome (Figure 5.1). The initial chitin as well as ChNCs prepared following the 3M540 and 5M180 protocols were found to exhibit comparable vibrational stretches, indicating that the molecular structure was unaltered during the hydrolysis and furthermore is consistent with the α-chitin allomorph. [16, 23] The vibrational stretches at 3440, 3260, and 3100 cm^{-1} correspond to hydroxy O-H, and amine N-H symmetric and antisymmetric stretches, respectively. [16] Weak peaks at ca. 2890 cm^{-1} were attributed to stretching of various C-H bonds. The pair of peaks at 1660 and 1620 cm^{-1} corresponding to amide C=O stretching (amide-I) which is split due to the hydrogen bonding and conformation in the α-chitin crystalline structure. This splitting is absent in the β-allomorph. [16, 22] Another significant peak at 1555 cm^{-1} is also associated with N-H deformation (amide-II). [16] In summary, these results indicate that the starting and the prepared samples are all composed of α-chitin with the molecular or crystalline structure largely unchanged during the acidic hydrolysis.

The samples were further investigated by powder X-ray diffraction (pXRD) (Figure 5.2). The diffractograms further validate that the starting material and the prepared ChNC samples

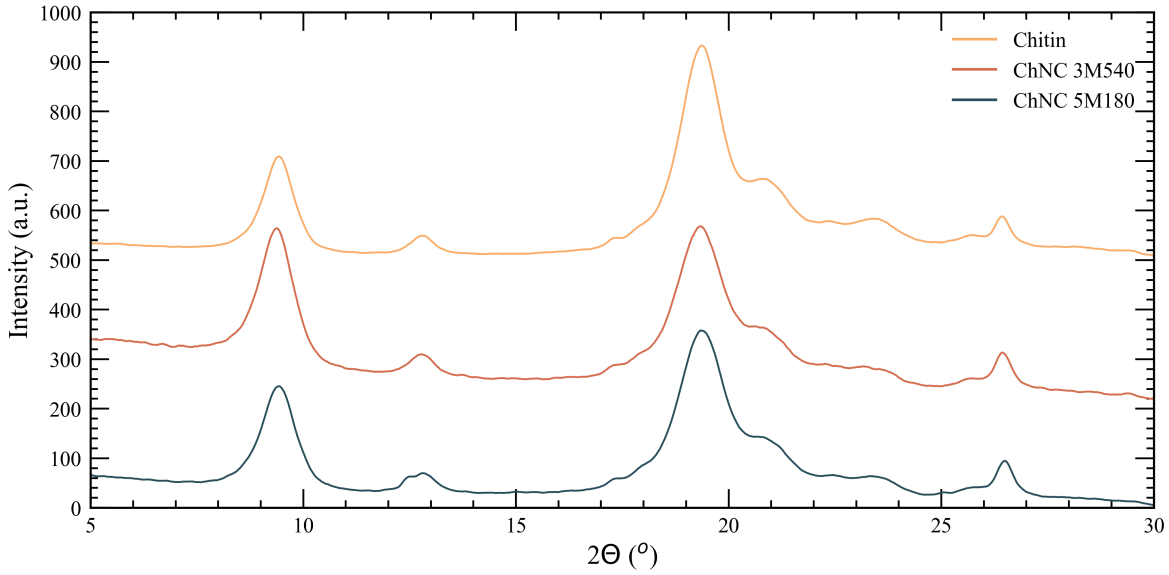

Figure 5.2 pXRD diffractograms of chitin and ChNCs. The diffraction peak positions are consistent with the reported values for α-chitin. The peak positions and broadness remain invariant as a result of hydrolysis, suggesting no change in crystal structure or crystallinity. The peaks are assigned in Table 5.2

Table 5.2 Assignment of diffractions peaks observed in pXRD diffractograms. These diffraction peaks are consistent with the α-chitin crystal structure and appear to be largely consistent between chitin, and two most extreme ChNC samples, 3M540 and 5M180. [23]

Diffraction angle (2Θ°)	9.4	12.8	19.4	20.9	23.4	26.5
Assigned crystal lattice plane	020	021	110	120	130	013

were α-chitin. Another important parameter which can be inferred is crystallinity. Chitin is a semicrystalline polymer with only part of it being comprised of ordered chitin chains which give rise to diffraction peaks observed by pXRD. Crystallinity thus can be used to determine the amount of the material that is crystalline with respect to the rest of the material. To assess crystallinity quantitatively and reliably is challenging, however the qualitative comparison can be done. [190] In fact, all the samples appeared to be similarly high in crystallinity, which remained virtually unchanged upon hydrolysis. All the samples presented diffraction peaks comparable in position and size to the starting material. These peaks indicate that all samples and the starting material are highly crystalline (Table 5.2). [23] It should be noted that the peaks are overall much wider than is commonly observed for inorganic crystalline materials, which is a result of a finite crystal size or crystal imperfections of semi-crystalline α-chitin samples. [191] For more quantitative interpretation of pXRD, tools are yet to be developed to reproducibly extract the value of crystallinity of *chitin* and *ChNCs*.

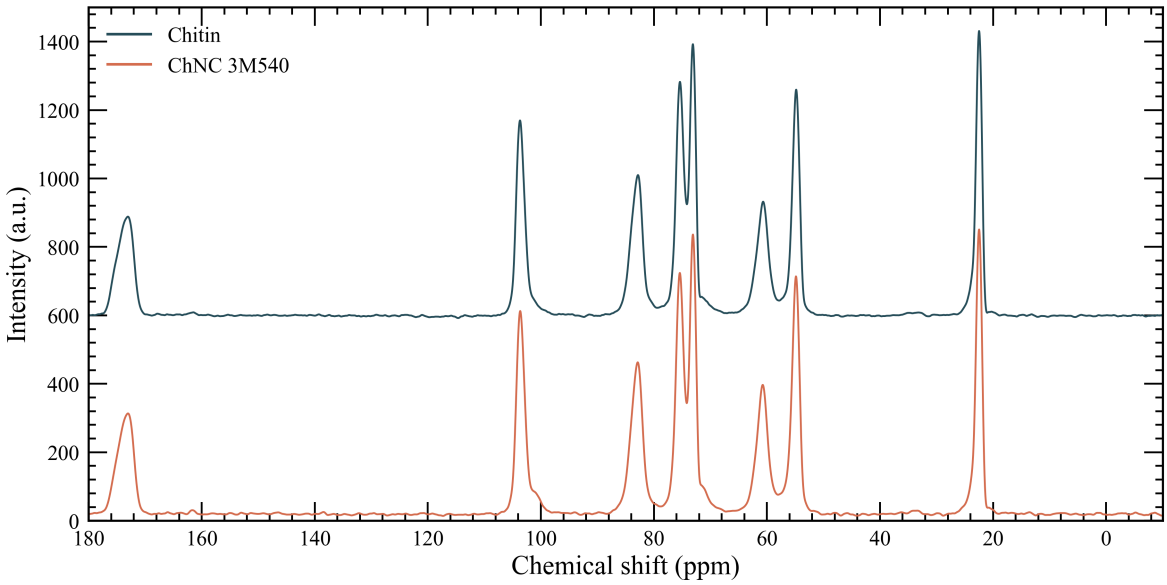

Figure 5.3 ^{13}C ssNMR spectra of chitin and ChNCs. The starting material and resulting 3M540 are identical and composed of chitin on a molecular level. Overall sharp peaks indicate a high level of crystallinity.

With FTIR and pXRD indicating that the raw chitin feedstock and the resulting ChNC are chemically identical, ^{13}C ssNMR was performed on the starting material and ChNC 3M540 sample to assess purity and the molecular structure of the samples (Figure 5.3). The peaks were assigned and fit well to the structure of chitin: ^{13}C ssNMR (200 MHz): δ ppm 173.0 C (of carbonyl), 104.0 (C1), 82.8 (C4), 75.5 (C5), 73.0 (C3), 60.7 (C6), 54.9 (C2), 22.7 (C (of -CH_3)). As expected, the starting material and 3M540 samples were composed of chitin on a molecular level while sharp peaks overall indicate a high degree of crystallinity which is in strong agreement with the FTIR and pXRD data. Elemental analysis (data not shown) reported negligible amounts of ash indicating that purified chitin and the prepared samples do not contain any mineral impurities.

In summary, acid hydrolysis of chitin does not affect the molecular or crystalline structure significantly as evidenced by FTIR, pXRD, and ^{13}C ssNMR analysis. It is worthwhile to note, that chitin is not soluble and does not swell much in the acidic aqueous conditions employed to produce ChNC, meaning that this reaction is heterogeneous. The chitin bundles and fibrils can only be initially reacted at the surface with the reaction preferentially occurring at more accessible regions, which have more amorphous character, rather than tightly packed crystalline parts. There are two main reactions which are possible: amide hydrolysis and hydrolysis of glycosidic bond. The latter reaction is thought to occur much more rapidly in amorphous or strained regions of the crystal structure, thus allowing for the reaction to

proceed and result in shortened chitin molecular chain lengths but leaving chitin otherwise virtually unchanged. This thus allows to cut otherwise long fibrils of chitin into shorter lath-like nanocrystals. Interestingly, any changes in crystallinity were insignificant, as otherwise they would be evident by qualitative comparison of diffractograms (Figure 5.2), and correlate well with the already high crystallinity of the starting material. The other possible reaction, the hydrolysis of the surface amide functional groups does not appear to be happening significantly enough to be observed at the resolution provided by ^{13}C ssNMR spectroscopy. In fact, it was semi-quantitatively determined, by comparing the integrals under the peaks, that the initial chitin had around 98 % of amides and 2 % of amines and this ratio remained unchanged after the acidic hydrolysis of chitin, which yielded ChNCs.

5.1.2 Colloidal properties

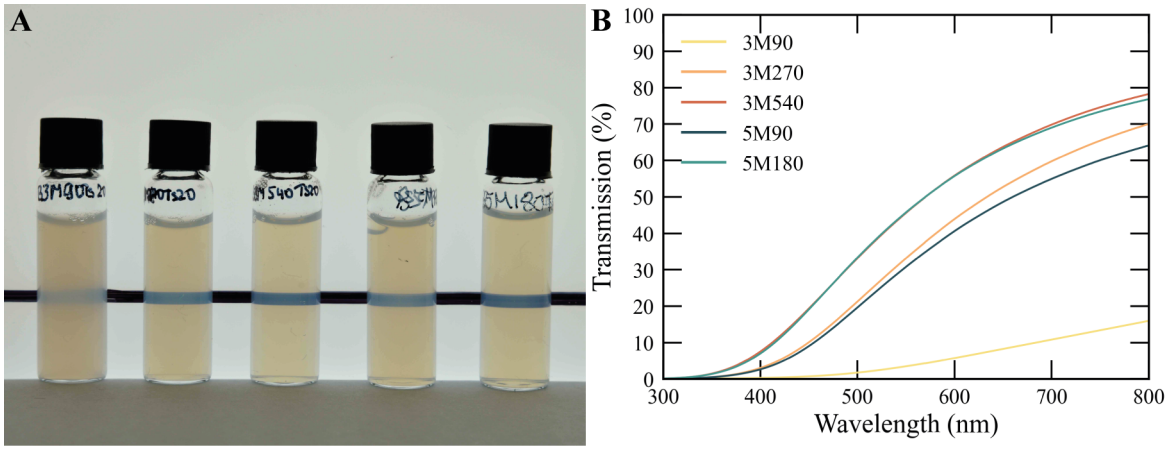

Figure 5.4 Turbidity of ChNCs prepared at different hydrolysis conditions. **A** A photograph of ChNC 3M90, 3M270, 3M540, 5M90, and 5M180 (left to right) samples at 1.00 wt% after shaking and then imaged with uniform back illumination. A black line was drawn on the illumination source to assess the sample turbidity. **B** UV-vis spectra of these samples showed that transmission increases with both the hydrolysis acidity and duration.

Inspecting the ChNC suspensions hydrolysed under different conditions, the 3M90 sample was clearly much more turbid (Figure 5.4 A). In contrast, the black line drawn on the illumination source could be clearly seen through all the other samples. This was quantitatively confirmed by measuring the transmission spectra (Figure 5.4 B). In general, the transmission declined for all the samples as the wavelength decreased which can be attributed to more efficient scattering of larger wavelength by small nanoparticles, corresponding to the Rayleigh approximation for scattered light. [84] The 3M90 sample, was significantly less transmissive then all the other samples with, for example, less than 20 % of light

transmitted at 800 nm compared to at least 60 % of light for all the other samples. This indicated that 3M90, unlike other samples, was poorly dispersed with many larger particles or aggregates still being present (Figure 5.6). Such objects cause strong scattering as they can be approximated as Mie scatterers, giving rise to the observed turbidity. [84] Furthermore, a degree of sedimentation was observed within days if 3M90 was left unperturbed. For the other samples, the trend in transmission suggests that longer hydrolysis durations result in smaller particles on average.

These observations agree with the particle size measurements obtained by dynamic light scattering (Figure 5.5 A). The large Z-average value of 3M90 sharply decreases as the hydrolysis is prolonged to longer timescales up to 3M270. Beyond this point, further hydrolysis had little effect on the particle size (Figure 5.5 A). In contrast, hydrolysis with a higher acid concentration (5.0 M) could reach a similarly small average particle, with 5M90 measured to have a Z-average particle size comparable to that of 3M270. The strong dependence on acidity is indicative of the hydrolysis of the glycosidic bond occurring at a higher rate when the acidity is increased. This interpretation also supports the observation that 5M270 turned dark brown/grey due to over-hydrolysis, in contrast to off-white coloured 3M540 sample. Thus, the higher acidity allowed for the much faster degradation of amorphous and crystalline structure of chitin leading to side reactions and over-hydrolysis. 3M540 and 5M180, on the other hand, both represent samples where most of the amorphous regions have been etched, with little effect on the crystal, as they exhibited the lowest turbidity and smallest average particle size (Figure 5.4, 5.5 A). A more in-depth analysis of the nanoparticle dimensions using transmission electron microscopy (TEM), agrees in general with these observations. 3M90 has significantly larger dimensions, in agreement with the previous turbidity and DLS analysis. For other samples, the nanoparticle length and width averaged to 180 and 14 nm, respectively, with the exception of 5M180 which yielded the smallest particles but with a comparable aspect ratio of 14 (Figure 5.5 D, E, F).

Beyond the differences in the nanoparticle dimensions, the surface charge was also influenced by the hydrolysis conditions (Figure 5.5 B, C). The large nanoparticles of 3M90 with a compromised stability were unsurprisingly accompanied by the lowest surface charge. More generally, the surface charge was found to increase with the reaction duration towards a limit of $\sim$280 $mmol_{-NH_3^+}/kg_{ChNC}$. Higher acidity had only marginal influence on the surface charge, which is consistent with the previous studies on small molecules that showed the rate of amide hydrolysis plateaued at similarly high hydrochloric acid concentrations. [192] Reaction duration was therefore considered to be the key parameter to control amide hydrolysis and thus the surface charge of the ChNCs.

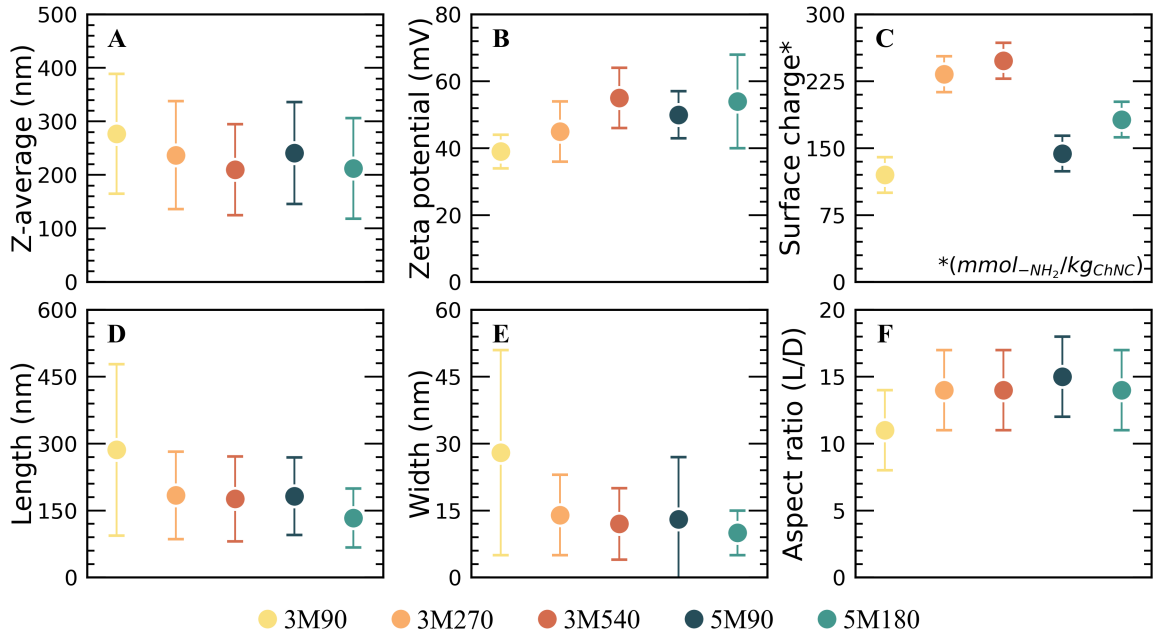

Figure 5.5 Colloidal properties of ChNCs prepared with different hydrolysis conditions. **A** Z-average and **B** $\zeta-$potential as measured by DLS. **C** Surface charge measured by conductometric titration. **D, E, F** Length, width, and aspect ratio, respectively, measured by TEM. *The error bars represent one standard deviation. TEM micrographs were acquired by Yu Ogawa.*

5.1.3 Liquid crystalline behaviour

Following the successful hydrolysis to prepare colloidally stable ChNC suspension, the ability to form a liquid crystalline phase was explored. All the ChNC samples reported in Table 5.1 exhibited liquid-crystalline behaviour, evidenced by the separation of two phases (Figure 5.7 A). The bottom one, anisotropic, appeared bright when looked at in transmission between crossed-linear polarisers. The ChNC 3M90 sample, however, failed to phase separate with a clear interface, which were related to its poorer dispersity, stability, and lower surface charge.

Macroscopic phase separation, as described before (Figure 2.3 A), was observed in all the samples above a concentration of $\sim$ 3.0 wt% (Figure 5.7 A). This marked the first threshold concentration, C_I, after which an anisotropic liquid crystalline phase formed and sedimented to the bottom of the capillary. At this concentration, primarily high aspect ratio or volume nanoparticles start the phase transition according to Onsager's theory for liquid crystalline behaviour of rod-like particles. [52, 53] All the prepared samples were polydisperse and had a fraction of large nanoparticles (or their bundles) which is evidence by the large standard deviations in length and width measurements acquired by TEM (Figure 5.5 D, E, F). Upon increasing the ChNC concentration, the volume fraction of the anisotropic phase within this

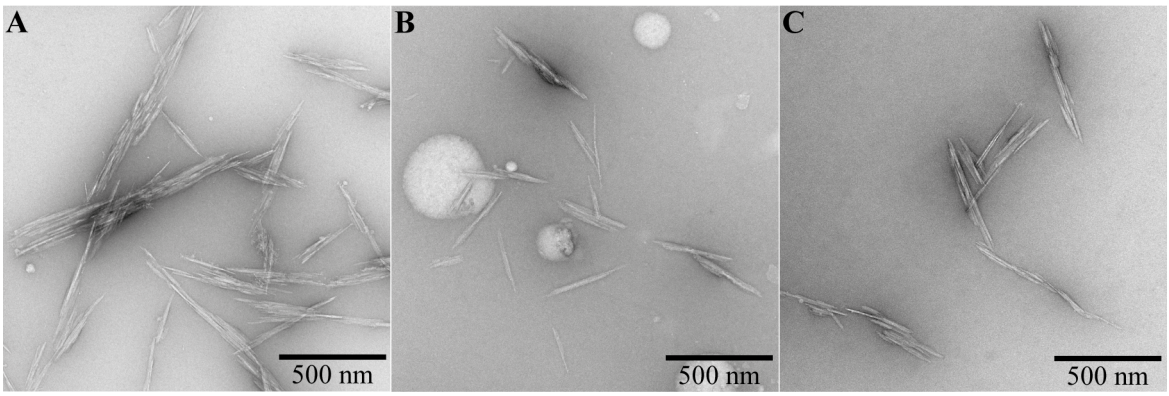

Figure 5.6 Transmission electron microscopy micrographs of ChNCs prepered at 3.0 M HCl with varied reaction duration. **A** Micrograph of 3M90 sample shows big bundle-like aggregates present. **B, C** Micrographs of 3M270 and 3M540 show that they have nanoparticles which are much more dispersed and less bundled into aggregates. *TEM micrographs were acquired by Yu Ogawa.*

biphasic regime grew linearly, until reaching a second threshold concentration, C_A, at which the entire suspension was anisotropic (Figure 5.7).

This second threshold concentration, in general, increased with hydrolysis duration. It correlates with decreasing size and surface charge of ChNCs. For example, C_A went up from 6.0 wt% to 7.0 wt% to 8.0 wt% as the hydrolysis duration was increased to obtain 3M90, 3M270, and 3M540 samples, respectively. These observations are consistent with the concept of an shrunk double-layer upon increasing surface charge (see Appendix A), which results in a smaller effective volume (Section 2.2). Given the ionic strength for each suspension was fixed uniformly to 100 $mmol_{HCl}/kg_{ChNC}$, the double-layer could only be modulated by the differences in the surface charge. This interpretation correctly predicts that the second threshold concentration of 5M90 should be lower than 5M180 and also that both samples should lie in-between 3M90 and 3M270.

A closer inspection into ChNC 3M90 sample revealed a sharp increase in the apparent volume fraction of the anisotropic phase at around 6.0 wt%. Below this concentration, a near-linear relationship was observed which suggests an interruption of the macroscopic phase separation via the formation of an attractive-gel formation. This could be because of overall poorer colloidal stability and significantly lower surface charge of 3M90 as compared to the rest.

Polarised optical microscopy (POM) of the anisotropic phase revealed the characteristic chiral nematic fingerprint pattern in all samples, confirming the nature of the liquid crystal phase (Figure 2.5, 5.7 B). The observed periodicity, and thus the chiral nematic pitch, could be measured and was found to decrease with increasing ChNC concentration. This

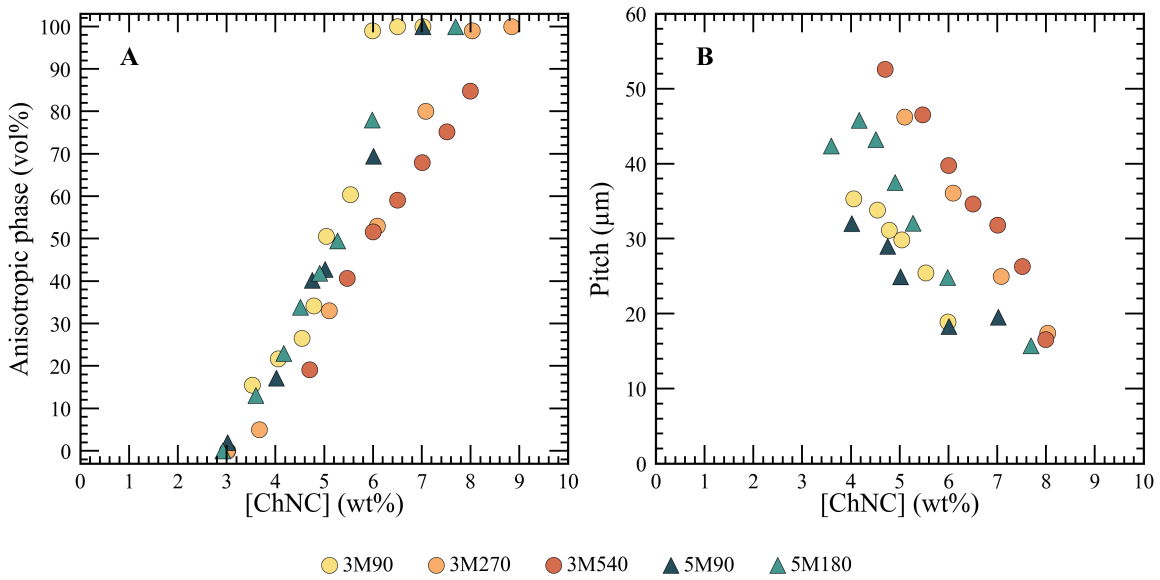

Figure 5.7 Liquid crystalline behaviour of ChNCs prepared at different hydrolysis conditions. **A** Phase diagrams showing the changes in the amount of anisotropic phase as a function of ChNC concentration. **B** Pitch diagram depicting decreasing chiral nematic pitch as a ChNC get concentrated.

is attributed to the ChNCs being forced into closer proximity to neighbouring nanoparticles and, consequently, exhibiting stronger chiral interactions. In addition, higher surface charge bearing samples exhibited a larger chiral nematic pitch, which can be explained by a more expanded double-layer enforcing greater separation between the physical nanorods, leading to weaker chiral interactions relatable to physical nanocrystals being forced to be further apart because of more expanded double-layer. Nevertheless, soon after the second threshold concentration the fingerprint was no longer observable despite the phase appearing anisotropic. At such high concentrations, the suspension is viscous and becomes aligned because of the shear experienced when the suspension is sucked into the glass capillary. Such an alignment explains that the suspension appears anisotropic when looked at in transmission between two crossed linear polarisers, however, there is a point where the suspension is so viscous that it behaves like a gel and, therefore, does not relax from the sheer-alignment to the thermodynamically preferred chiral nematic phase. This gelling behaviour, also known as kinetic arrest, allows the preservation of the order (or disorder) in the system when the concentration of the suspension reaches a critical point.

Overall, 3M270, 3M540, 5M90, and 5M180 were appropriate conditions to hydrolyse shrimp chitin to obtain well-dispersed and colloidally stable ChNC suspensions. Using 3.0 M HCl is more environmentally friendly, avoids the risk of over-hydrolysis, and gives higher ChNC yields, while giving nanoparticles of comparable dimensions but of a higher

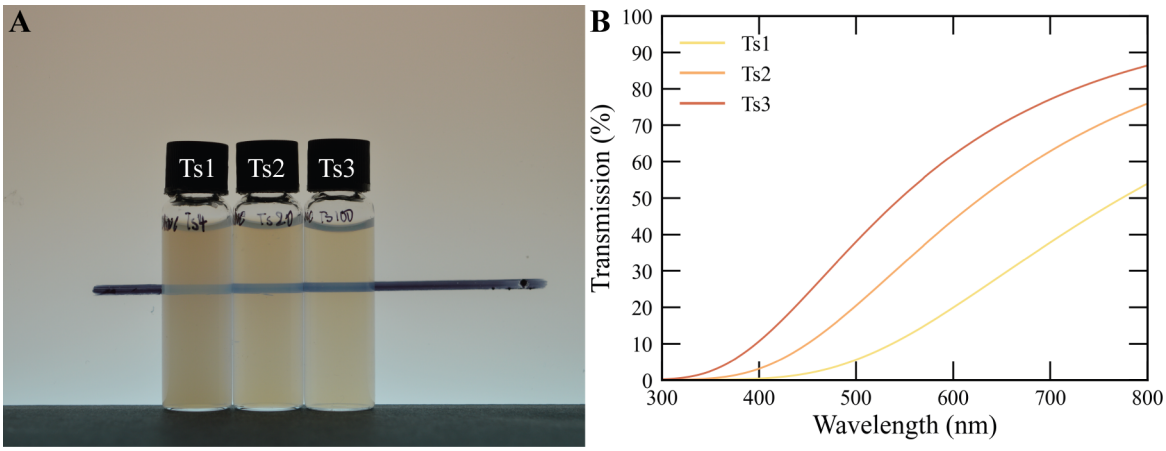

Figure 5.8 Turbidity of ChNCs processed with different tip sonication times. **A** A photograph of samples of Ts1, Ts2, and Ts3 (left to right) at 1.00 wt% after shaking and with uniform back illumination. A black line is included to assist in assessing the sample turbidity. **B** Transmission spectra show that transmission increased with extended tip sonication application.

surface charge, which aids with stabilisation of colloid. As such, given 3M540 had the highest surface charge and small particle size leading to the formation of a well-defined chiral nematic phase, this was chosen as the standard hydrolysis condition for the subsequent investigations into the production of ChNC.

5.2 Tip sonication

After hydrolysis and dialysis, even the best ChNC suspensions (e.g., 3M540) scatter a lot of white light due to the presence of larger particles. Nevertheless, they do not show any significant sedimentation which is observed for a previously discussed 3M90 sample. The aggregates which contribute to the scattering are made up of many individual ChNCs which can be dispersed by the mechanical treatment. Applying tip sonication to the ChNC suspension is one of the most convenient ways to do that. It results in high frequency and high energy sound waves propagating through suspension creating many points where cavities are formed and collapse, resulting in a big mechanical stress on the system. While it is commonly applied to ChNC suspensions, its effect is largely overlooked even though it can have a significant effect not only on the ChNC colloidal but also liquid crystalline properties. The latter phenomenon as was observed in CNCs where the application of tip sonication strongly affected the resulting nanoarchitecture and the structural colouration. [65, 75] Thus, overlooking this parameter as insignificant could hamper the reproducibility of ChNC studies and consequently limit the development of this field.

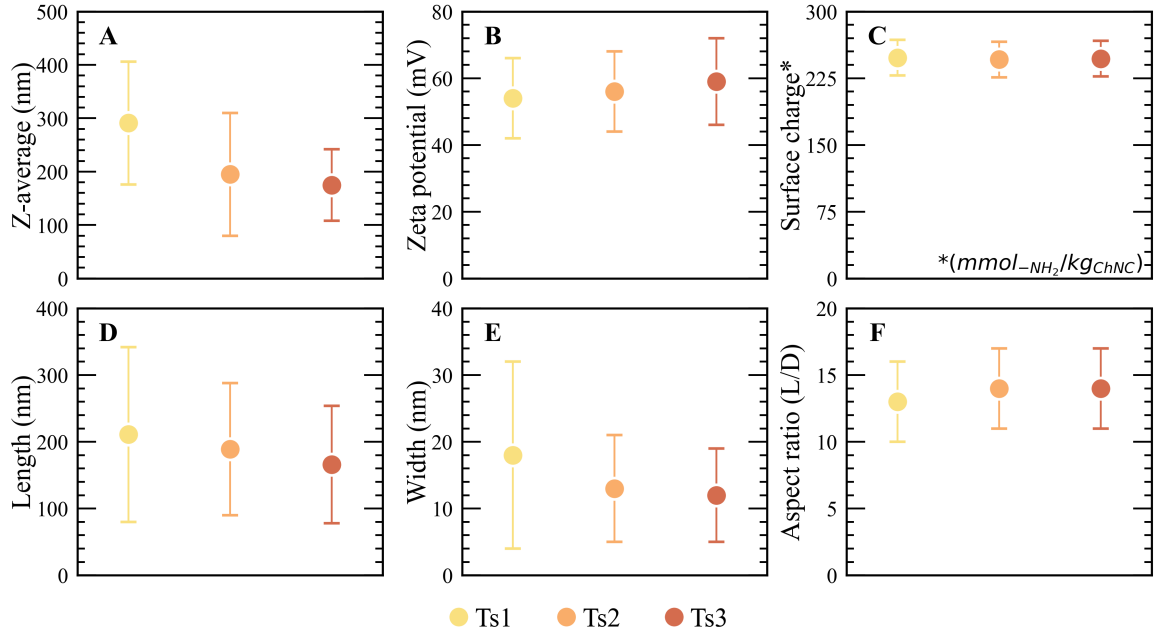

Figure 5.9 Colloidal properties of ChNCs prepared with different tip sonication conditions. **A** Size and **B** $\zeta-$potential as measured by DLS. **C** Surface charge measured by conductometric titration. **D, E, F** Length, width, and aspect ratio, respectively, measured by TEM. The error bars depict a standard deviation. *TEM micrographs were acquired by Yu Ogawa.*

The tip sonication treatment was studied by varying the application duration on a new batch of 3M540 suspension. Three tip sonication conditions were chosen: Ts1, Ts2, and Ts3, which refer to the tip sonication duration of 0.9, 4.5, and 22.5 min, respectively. For consistency, tip sonication was applied to suspensions in portions of the equivalent mass (200 ± 5 g) and concentrations (1.00 wt%). The ionic strength and pH were standardised to 100 $mmol_{HCl}/kg_{ChNC}$ by dialysing all suspensions at 1.00 wt% in separate dialysis bags but within the same bath. The heating of the samples during the tip sonication was avoided by using an ice-bath and appropriately spaced on and off intervals.

ChNC dispersibility improved with the continuous application of tip sonication (Figure 5.8). The initial immense effectiveness of tip sonication, however, started to level off with further application. These observations agreed with the decreasing average particle size as measured by DLS and TEM (Figure 5.9 A, D, E). This confirmed that the dimensions of the nanoparticles decreased as the ChNC bundles were dispersed. In contrast, the surface charge remained virtually unaffected and the slight increase in the ζ-potential could be associated with the nanoparticles getting smaller and thus more mobile (Figure 5.9 B, C).

When concentrated, these three samples spontaneously self-assembled into a liquid crystalline phase (Figure 5.10, 5.11A). The first threshold concentration was equivalent to

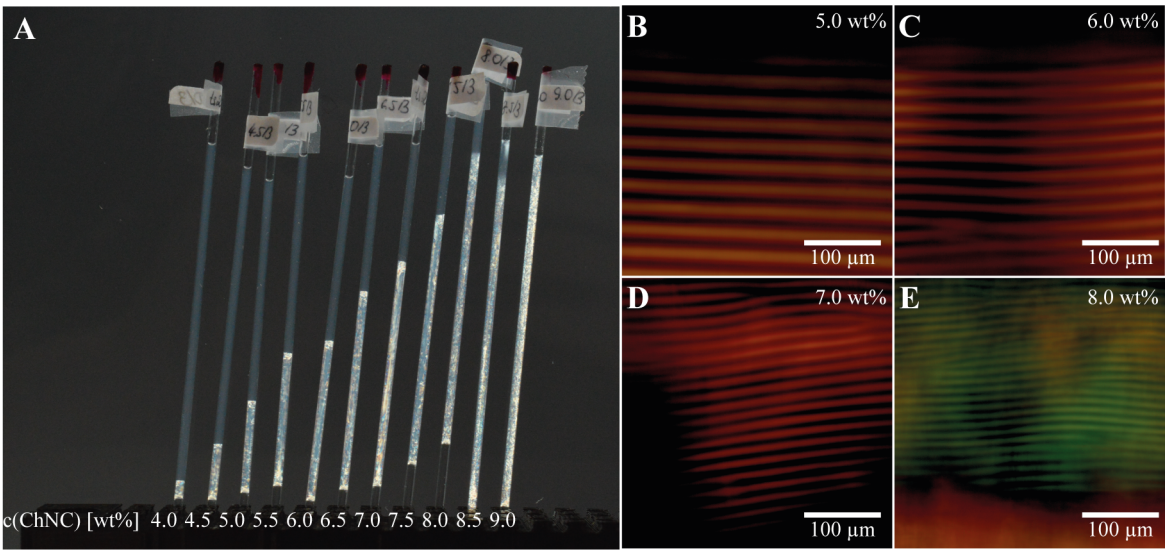

Figure 5.10 Liquid crystalline behaviour of ChNCs Ts2 sample. **A** A photograph of capillaries showing the phase separation with the increasing proportion of the anisotropic phase as the nanoparticle concentration was increased. Note that below and above the suspension in the capillary, there are air gaps. **B, C, D, E** Polarised optical microscopy micrographs of the anisotropic phase at increasing concentrations: 5.0, 6.0, 7.0, and 8.0 wt%, respectively.

$\sim$3.0 wt% with the anisotropic phase volume fraction gradually increasing until the second threshold concentration was reached. While Ts2 and Ts3 behaved comparably, Ts1 sample presented a slightly lower proportion of anisotropic phase at a given ChNC concentration. Given that the ionic strength, pH and surface charge are equivalent between the sample, and no changes in conductivity or pH were observed after tip sonication (unlike that reported for CNCs [65, 75]), only the changes in nanoparticle dimensions could be responsible. In fact, the application of tip sonication reduced the width of the nanoparticles more so than the length, leading to the aspect ratio of Ts1 being slightly smaller than for Ts2 and Ts3 (Figure 5.9 F). These observations agree with Onsager's theory for the self-assembly of rod-like nanoparticles that a smaller aspect ratio leads to the lower proportion of the anisotropic phase in a bi-phasic regime. [52]

The effect of tip sonication was even more pronounced when the pitch of chiral nematic phase of ChNCs was investigated (Figure 5.10 B, C, D, E, 5.11 B). The pitch for samples Ts2 and Ts3 was comparable, while that for Ts1 was significantly smaller, especially at lower nanoparticle concentrations. ChNCs investigated in-depth by TEM usually present numerous bundles which would be at least partly destroyed by such a mechanical treatment (Figure 5.6). The bundles have a stronger chiral shape, inducing stronger chiral interactions within the chiral nematic phase by behaving similarly to chiral dopants in molecular liquid crystals. [7] Dispersing them into smaller rod-like units makes their shape less chiral, explaining the

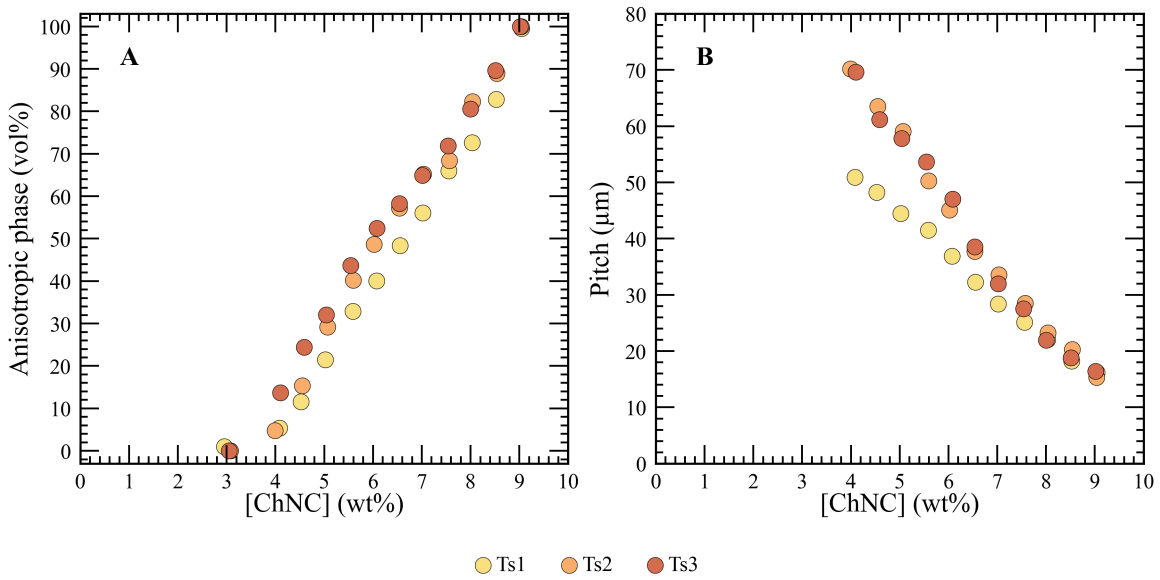

Figure 5.11 Self-assembly of ChNCs prepared with different tip sonication conditions. **A** Phase diagrams showing the increase in the amount of anisotropic phase as a function of ChNC concentration and tip sonication conditions. **B** Pitch diagrams showing the dependence of pitch on ChNC concentration and tip sonication conditions.

observed increase in pitch as the tip sonication duration was increased to Ts2. This energy input appears to be sufficient to disperse most of such chiral bundles as no further changes in pitch were observed for longer sonication times.

In summary, for good dispersibility and facile self-assembly properties, hydrolysis at 3M540 followed by Ts3 conditions is recommended. However, Ts2 in many ways is a sufficient and a much quicker process. It is notable that the tip sonication treatment would have to be readjusted if ChNC were prepared by different hydrolysis conditions as they highly influence the number of aggregates in the suspension before any treatment.

5.3 Deacetylation

As noted previously, the surface charge is an extremely important parameter that governs both the stability of the colloids and their interactions to form a chiral nematic liquid crystal. [24] In fact, the double-layer, which is key in preventing ChNC aggregation as well as modulating their self-assembly, originates from the protonation of the surface exposed amines. These, however, are not that numerous, because in chitin most of the substituents at carbon 2 are amides instead (Figure 2.1). Such "acetylated amines" cannot be ionised and thus do not contribute to the surface charge. However, hydrolysis can be employed to convert these

groups to amines, unlocking the potential for higher surface charges. While this effect can be controlled to a limited degree by acidic hydrolysis, as employed to initially prepare ChNCs, basic hydrolysis, also known as deacetylation, offers a finer control over the surface charge. [24]

However, when applying deacetylation on chitin, extra care needs to be employed. Chitin is a fibrillar material insoluble in aqueous solvents. The acidic hydrolysis, employed to produce ChNCs, is a heterogeneous reaction, which is key as the crystal structure of the original chitin is retained in preparation of the nanoparticles. These insoluble ChNCs can be colloidally dispersed because the surface amines can be protonated and provide electrostatic stabilisation in aqueous acidic conditions. In this case, essentially only the surface of ChNCs interact with the solvent and other nanoparticles. Similarly, basis hydrolysis can be used to increase the number of such amines, however, only if applied to the surface for which the reaction conditions need to be tailored. If it the deacetylation is done so that it occurs throughout the whole material, and not only on the surface, but it would also produce chitosan, which is soluble in aqueous acidic conditions and thus the nanoparticles would not be obtained. Therefore, to alter the colloidal and liquid crystalline properties of ChNCs, only the surface of such nanoparticles should be deacetylated.

Consequently, two alternative strategies were utilised to prepare ChNC samples with a range of surface charges, allowing its contribution to both the colloidal and liquid crystalline properties to be quantified.

5.3.1 Chitin deacetylation prior acidic hydrolysis

The first strategy required preparation of partially-deacetylated shrimp chitin (deAc-Chitin) from shrimp chitin (Ac-Chitin). Then, each chitin sample was subject to acidic hydrolysis following the 3M540-Ts3 protocol described above, to obtain chitin nanocrystals (Ac-ChNC) and deacetylated chitin nanocrystals (deAc-ChNC). Finally, the ionic strength and HCl concentration were set to 100 $mmol_{HCl}/kg_{ChNC}$ by dialysis in the same bath, as described previously.

Chemical composition

FTIR showed that the applied deacetylation process did not affect the α-chitin crystalline structure as both initial chitin samples had analogous spectra (Figure 5.12). pXRD analysis confirmed that the α-chitin crystalline structure was retained and therefore suggesting that if any effect happened it must have only affected the surface and not the bulk of the material (Figure 5.14). A significant difference would be expected if chitin was fully converted

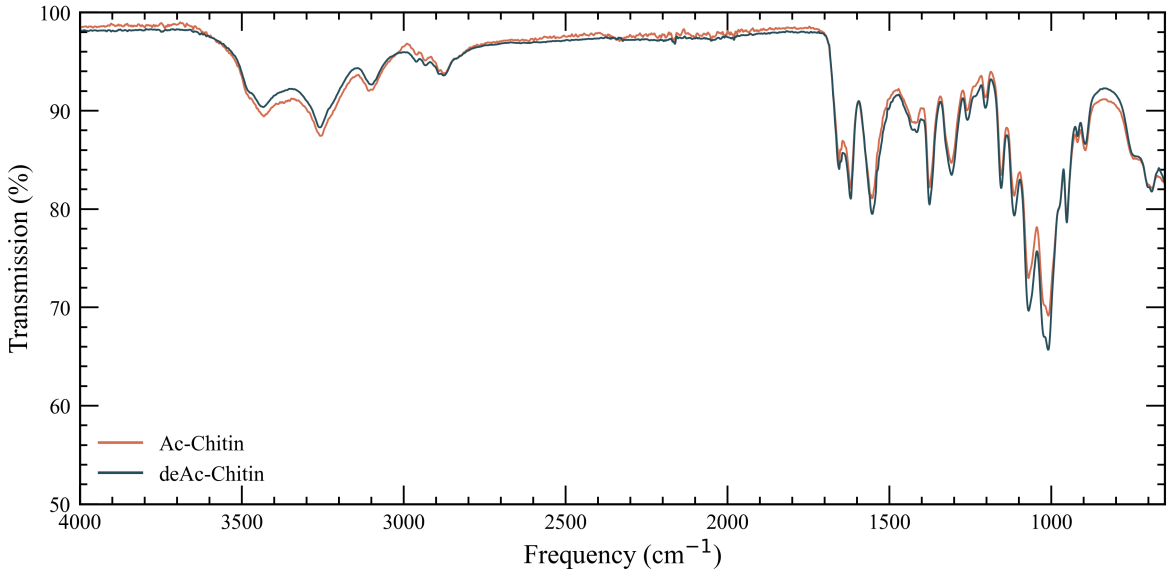

Figure 5.12 FTIR spectra of shrimp chitin in its original and partially deacetylated forms. The spectra show little change and indicate that α-chitin crystalline form was retained suggesting that only the surface was affected.

to chitosan. In fact, at these deacetylation conditions (aqueous NaOH (40 wt%) at 95 °C for 4 hours), the chitin crystalline structure, reportedly, does not swell and so only the surface should be affected. [25] The efficacy of the basic hydrolysis was confirmed by ^{13}C ssNMR, which showed that deAc-Chitin sample was partially deacetylated as compared to Ac-Chitin (Figure 5.13). Overall, these results suggest that at these conditions only the chitin molecules at the surface of chitin crystal were affected. This is crucial as the following acidic conditions, required to prepare ChNC from chitin, would dissolve the starting material if it was deacetylated throughout and, as a result, nanoparticles could not be produced at all.

In fact, ^{13}C ssNMR spectra could be used to semi-quantitatively determine the degree of acetylation (DA), which is defined as the ratio of the number amides over the combined number of amides and amines. This can be achieved when the pulse-sequence durations are chosen appropriate in the ^{13}C ssNMR experiment and a sufficiently long relaxation time. [23] Thereafter, the integral under the peak corresponding to the carbonyl carbon can be compared to the average integral under the peaks corresponding to the main chain carbons. From such an experiment, it was deduced that the initial DA for Ac-Chitin was ∼98 %, while a lower value of ∼90 % was obtained for deAc-Chitin, which was overall expected from the deacetylation reaction. Interestingly, however, after the acidic hydrolysis, both Ac-ChNC and deAc-ChNC samples had a DA of ∼98 %, which is highly comparable to the DA values for untreated chitin (Figure 5.13). A comparable number of surface amines was also confirmed

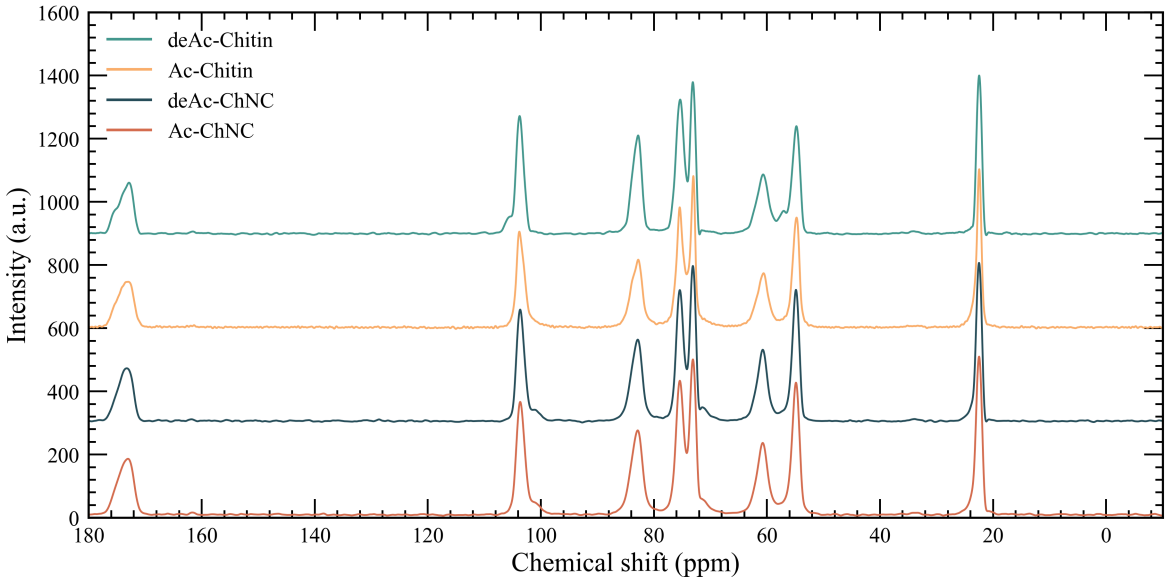

Figure 5.13 ^{13}C ssNMR spectra of partially deacetylated chitin and resulting ChNCs. Deacetylation was successful in increasing the number of amine groups on chitin. After acidic hydrolysis into ChNCs, the sample was indistinguishable from ordinary ChNC.

by employing a more sensitive conductometric titration which probes only the surface amines (Figure 5.15 C).

Colloidal properties

These observations were accompanied, however, by significantly smaller nanoparticles for the deAc-ChNC sample, which, was confirmed by both DLS and TEM (Figure 5.15 A, D, E). In particular, a detailed analysis by TEM revealed that while *both* length and width of deAc-ChNC were smaller, the relative change in the width was much more pronounced (Figure 5.15 D, E). These changes manifested in a significantly higher aspect ratio for deAc-ChNC (Figure 5.15 F). In other words, deacetylation followed by acidic hydrolysis provide the means to produce slenderer ChNCs with having a minute effect on their surface charge.

These results can be overall rationalised by considering that during deacetylation of chitin, only the surface of chitin crystals was affected, while the core remained largely unchanged, as suggested by ^{13}C ssNMR, FTIR, and pXRD data. Once the deacetylated chitin was subject to acidic hydrolysis, the expected hydrolysis of the more amorphous areas occurred resulting in ChNCs but besides this reaction, the deacetylated chitin molecules which were on the surface of chitin crystal were etched. The latter process occurred because deacetylated chitin is much more soluble in acidic aqueous conditions due to the numerous amine groups. In essence, the deacetylated surface of deAc-Chitin was etched during the acidic hydrolysis

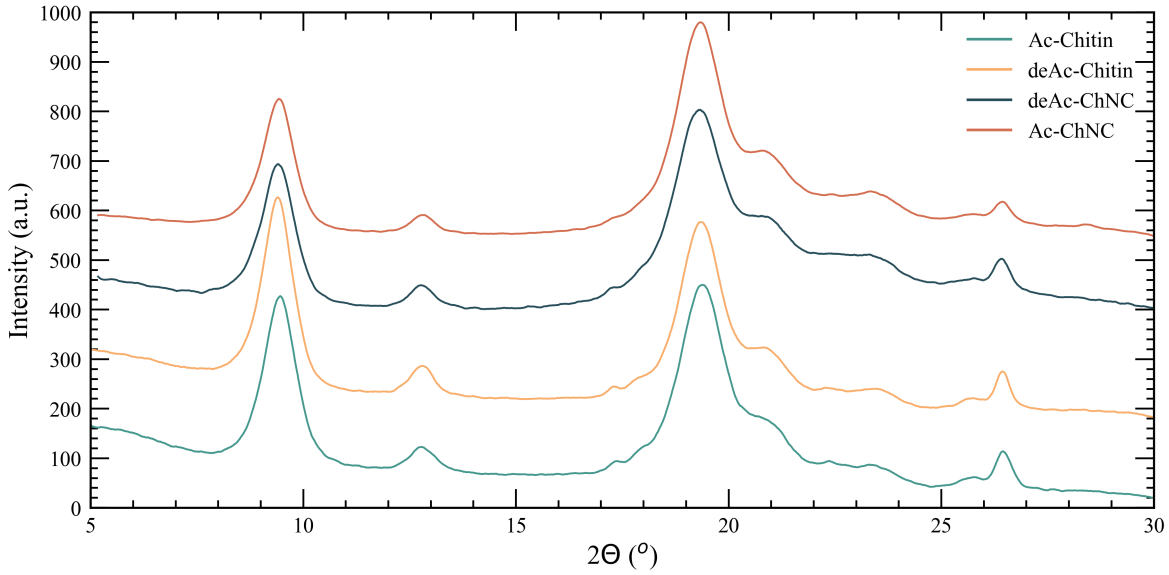

Figure 5.14 pXRD diffractograms of partially deacetylated chitin and resulting ChNCs. All the diffractograms were consistent with α-chitin crystalline structure, suggesting that the deacetylation occurred on the chitin fibril surface without penetrating and disturbing the crystalline structure.

resulting in slenderer deAc-ChNC than Ac-ChNC, but both having the surface comprised of unaffected chitin.

Liquid crystalline properties

The observed differences in the aspect ratio manifested in distinguishable liquid crystalline behaviours (Figure 5.16 A). While both suspensions had a similar first threshold concentrations of ≈3.0 wt%, the second threshold concentration was significantly lower for deAc-ChNCs. It is expected as Onsager's theory predicts a lower threshold concentration for rods of larger aspect ratios (Figure 5.15 F). Additionally, a significant difference in the chiral nematic pitch was observed (Figure 5.16 B). deAc-ChNC sample had a chiral nematic pitch ∼20 µm lower across the whole concentration series indicating stronger chiral interactions. These results from the prominent changes in thickness upon deacetylation, however, the exact the nature of this effect remains to be better understood as no theory to date explains the pitch evolution of chiral rods which are charged and disperse in size.

5.3.2 Chitin deacetylation after acidic hydrolysis

Despite being interesting, deacetylation of chitin prior to acidic hydrolysis, did not provide a practical way to controllably tune the surface charge of ChNCs. As such, the alternative

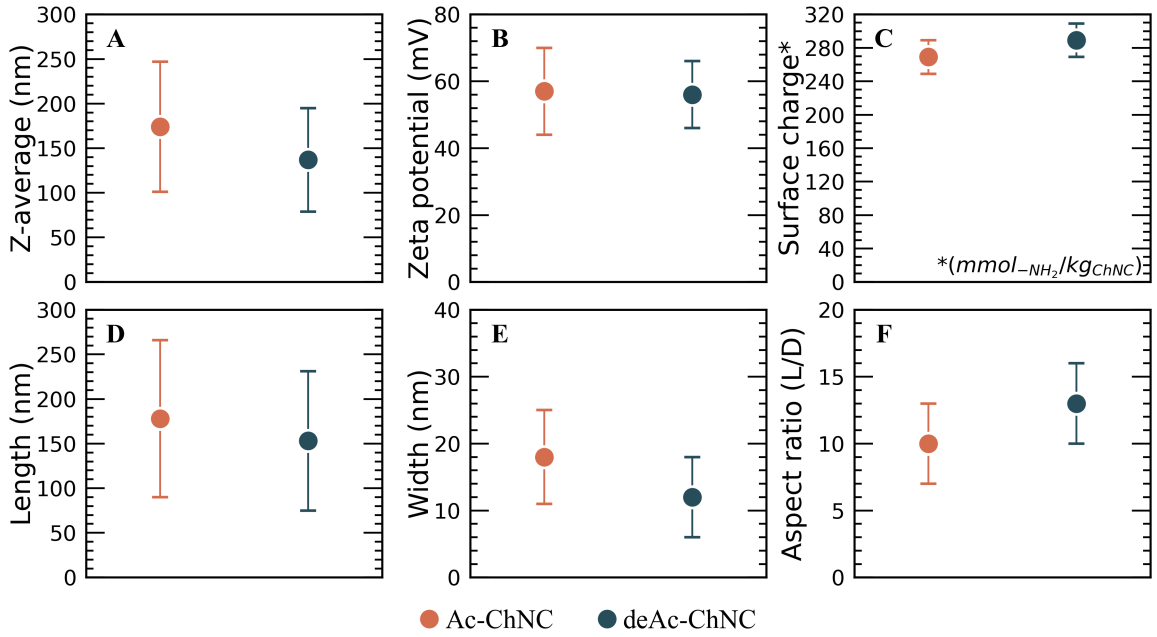

Figure 5.15 Colloidal properties of ChNCs prepared from partially deacetylated chitin. **A** Size and **B** $\zeta-$potential as measured by DLS. **C** Surface charge measured by conductometric titration. **D, E, F** Length, width, and aspect ratio, respectively, measured by TEM. *TEM micrographs were acquired by Yu Ogawa.*

strategy of post-deacetylation was explored. A new batch of ChNC suspension was prepared following the 3M540-Ts2, from which 4 samples were derived overall by running deacetylation directly on ChNCs for 0, 1, 2, and 3 hours. The 0h sample was prepared by immediately quenching the reaction once ChNC suspension was combined into the reaction mixture. Such a control experiment should allow for the effect of mixing ChNC into a high ionic strength and pH solution to be understood. Deacetylation conditions used here (33 wt% NaOH, 90 °C) were slightly milder than the ones used in section 5.3.1, which were confirmed to only alter the surface. These samples were also compared to a ChNC sample from the same batch but before (denoted as b4) deacetylation. The ionic strength and pH were standardised to 50 $mmol_{HCl}/kg_{ChNC}$ as well as equivalent tip sonication conditions (Ts2-like) were applied to all the samples. The samples treated with NaOH had to be tip sonicated after the deacetylation and dialysis against HCl as the experience of high ionic strength and pH caused them to aggregate.

Colloidal properties

Given that ChNC suspensions were subject to extreme ionic strengths and pH during the basic hydrolysis, issues such as irreversible aggregation could be expected. While all the

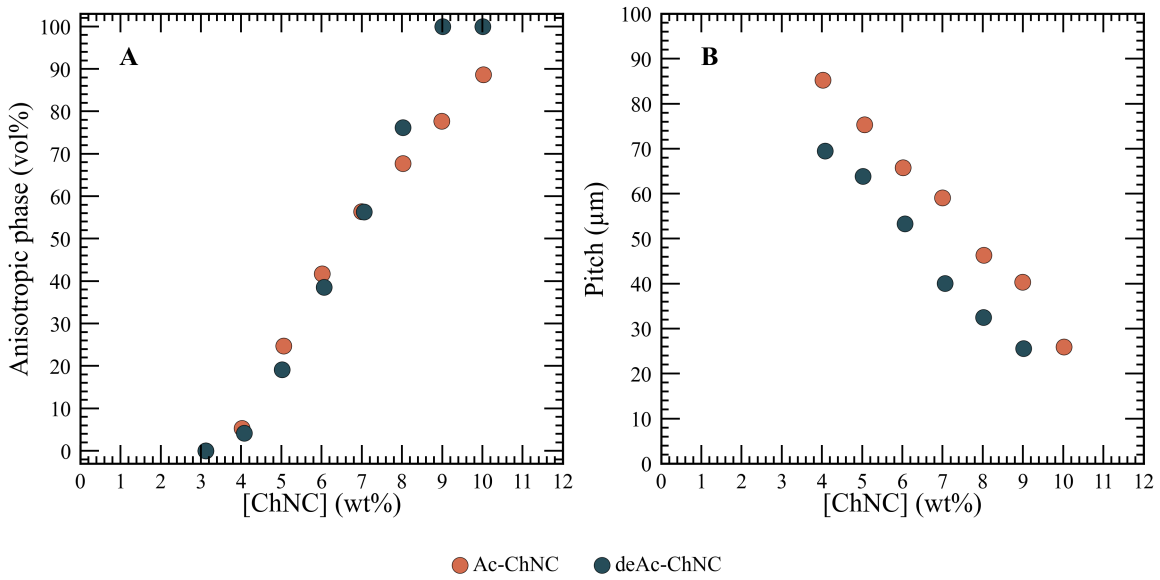

Figure 5.16 Liquid crystalline behaviour of ChNCs prepared from partially deacetylated chitin. **A** Phase diagrams showing that the deAc-ChNC sample had a lower second threshold concentration (C_a). **B** Pitch diagrams showing that the chiral nematic pitch decreased for samples prepared from deacetylated chitin.

samples dispersed well, with comparable ChNC sizes, they were consistently slightly higher than recorded for the suspension before deacetylation (Figure 5.17 A). These results were also confirmed by TEM analysis (Figure 5.17 D, E). In addition, all the resulting samples were stable and did not show any sedimentation within weeks.

While the dimensions changed only slightly, the surface charge could in fact be controllably tuned. The duration of this reaction was to a first approximation linear with respect to the surface charge, allowing to obtain surface charge spanning a range of values between 250 and 400 $mmol_{NH_3^+}/kg_{ChNC}$ (Figure 5.17 C). Interestingly, 0h-ChNC sample showed a lower surface charge which may be indicative of the dissolution and degradation of short oligosaccharides which could have been adsorbed onto ChNC surface when acidic hydrolysis reaction was quenched. Such short oligosaccharides were proved to exist on a CNC surface; however, different reaction conditions are usually employed in preparing them. [159]

Liquid crystalline behaviour

All the prepared samples exhibited phase separation but with significant differences (Figure 5.18 A). The first threshold concentration, C_I, indicative of the isotropic to biphasic transition, shifted to higher concentrations as the surface charge increased with an exception between b4-ChNC and 0h-ChNC samples. This deviation from the trend could be attributed

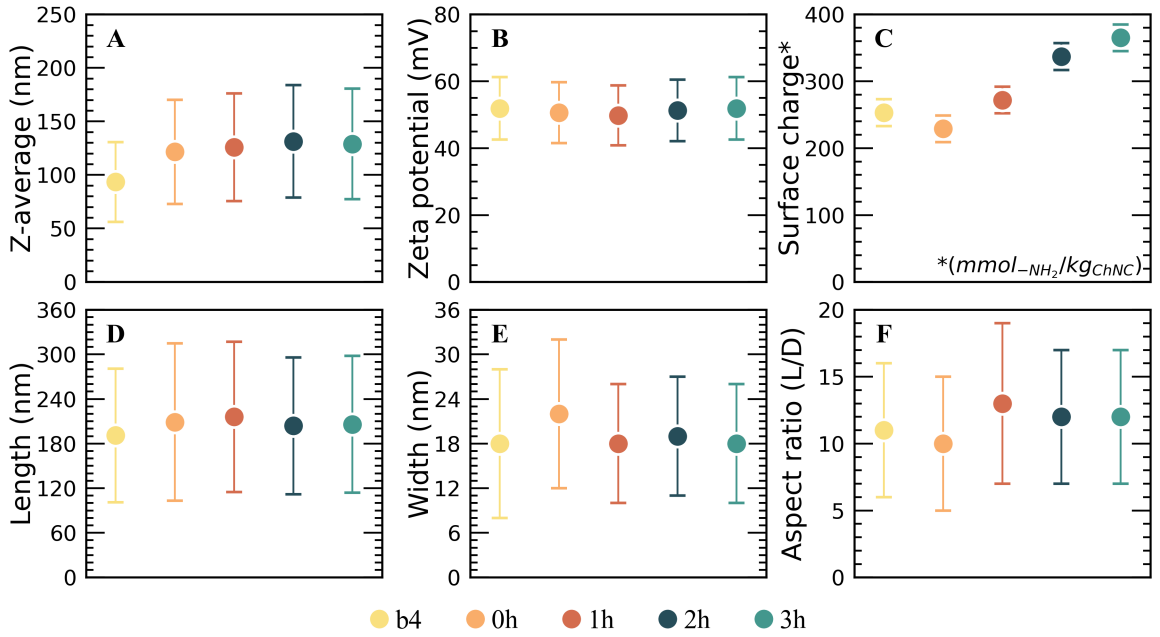

Figure 5.17 The effect of directly deacetylating ChNCs on their colloidal properties. **A** ChNC size increased due to deacetylation as measured by DLS. **B** ζ-potential remained largely unaffected. **C** Surface charge increased as a function of the reaction duration. **D, E, F** Length, width, and aspect ratio, respectively, as measured by TEM indicate an increase in particle size due to deacetylation treatment. *TEM micrographs were acquired with the help of Heather Greer*

to the slight increase in the particle size without a significant change in the surface charge, while the remainder of the samples showed that the surface charge increase dominated over the small increase in size. The remainder of the samples 0h through 1h, 2h, and 3h were all of similar dimensions so only the differences in the double-layer could have induced such differences in their liquid crystal properties. Based on the calculations presented in Appendix A, the double layer must have shrunk as a result of increased surface charge, resulting in lower effective nanoparticle volume. As such, the more charged nanoparticle had to get more concentrated before they started to experience crowding strong enough to start to phase separate, marking an increased C_I.

The biphasic regime followed the first threshold concentration, however, it only developed in ChNC suspensions with the surface charge below 300 $mmol_{-NH_3^+}/kg_{ChNC}$. For ChNC samples deacetylated for 2 h and 3 h samples, the apparent anisotropic phase volume fraction sharply reached 100 %, indicating that the suspension is gel-like, which prevented the relaxation of the shear alignment induced when the suspension was placed into capillaries (Figure 5.19). This should only be the result of the higher surface charge as the ionic strength

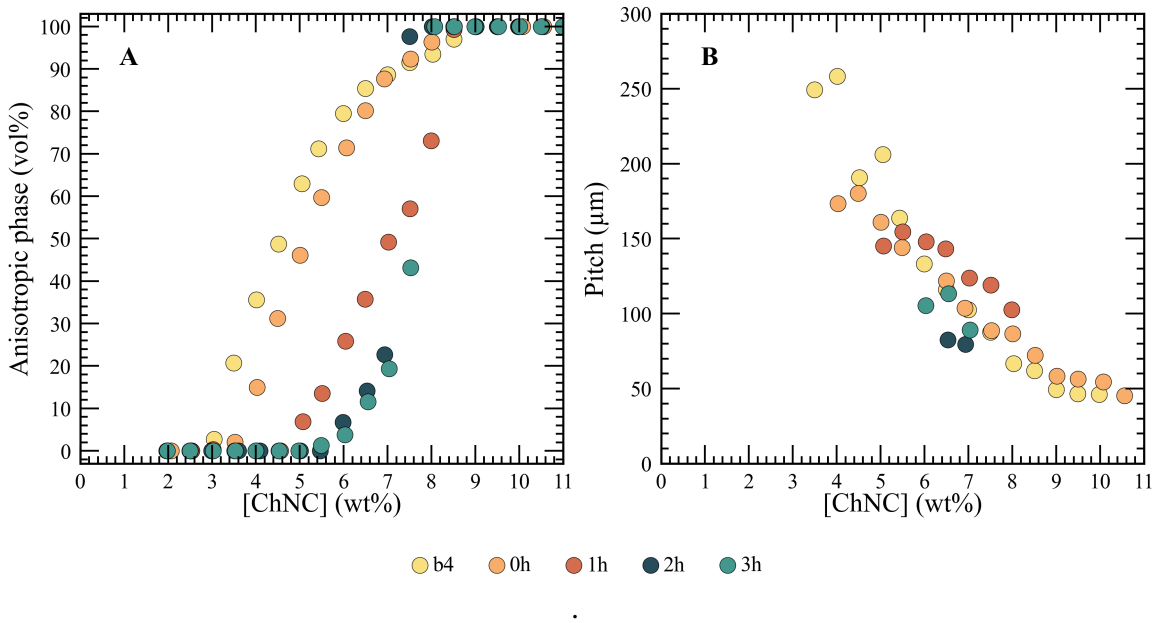

Figure 5.18 Liquid crystalline behaviour of directly deacetylated ChNCs. **A** Phase diagrams indicated that the threshold concentrations increased as a function of surface charge. ChNC samples deacetylated for 2 h and 3 h exhibited a sharp increase in the proportion to the apparent anisotropic phase which can be related to the suspension starting to behave like a gel past a certain concentration. **B** Pitch diagrams showed that only the b4, 0h, and 1h could consistently form chiral nematic phases.

or pH were set equivalently for all samples by dialysing together in the same dialysis bath but different dialysis bags.

The anisotropic phase was further studied by means of POM. In agreement with the attractive gel formation, the chiral nematic pitch could only be measured in samples only prior to the sharp increases in the amount of anisotropic phase (Figure 5.18 B). It appears that the changes in the surface charge, however, had a negligible effect on the chiral nematic pitch as at a given concentration, all the samples that formed a chiral nematic phase had a comparable pitch. In particular, having a high surface charge appears to be a hindrance in the formation of the chiral nematic phase as the suspension starts to become like a gel at concentrations lower than the threshold concentration for the formation of the chiral nematic phase.

5.4 Mushroom: a different source of chitin

The original idea to carry out the work, which culminated in this chapter, was conceived, and developed by the author of this thesis. The experiments were carried out together with

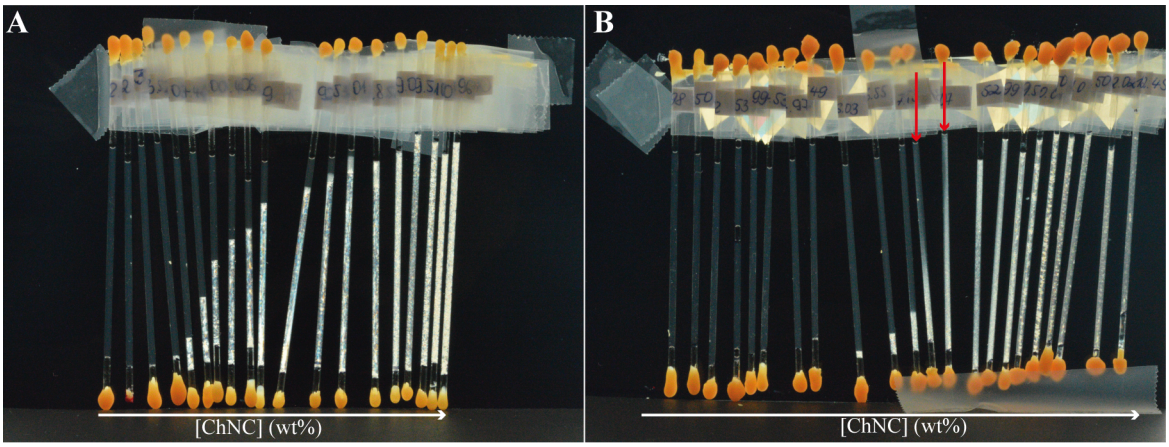

.

Figure 5.19 Phase separation of 0h and 3h deacetylated ChNC samples. **A** Concentration series for 0h deacetylated ChNC sample was constructed and exhibits clear phase-separation behaviour with a clear interface for each sample in the biphasic regime. **B** Concentration series for 3h deacetylated ChNC sample, however, shows that only initially the biphasic region exhibits a clear interface between isotropic and anisotropic phases. The red arrows indicate the capillaries which appear of incapable of phase separating and thus giving rising to a sharp rise in the apparent proportion of anisotropic phase.

Jordi Ferrer-Ori, a visiting Bachelor's student, who worked under close supervision by the author of this thesis.

Chitin can be found in a range of natural sources and here lies its advantages and limitations. The morphology and physical properties, such as swelling in aqueous conditions or crystal structure, can be source-dependent and cannot be changed. However, given the universality of chitin, it is hardly surprisingly that it can be used for different purposes as well as being biosynthesised by different enzymes. [193] Thus, it can be expected that changing the source of chitin, significant differences in chitin physical properties can be expected which could be translated into ChNCs which are of different dimensions, surface charge, crystal structure or crystallinity. This in turn can expand the range of colloidal and liquid crystalline properties of ChNCs by simply choosing a different source of chitin. Shrimps (belonging to crustacean phylum, the chitin source used so far in this study), are extremely distinct phylogenetic relatives to fungi which also utilise chitin. As such, *Agaricus bisporus*, a common spring mushroom, was chosen as an alternative raw starting material as it is cheap, widely available in big quantities, which is important to note, given that purified chitin constitutes only about 0.5 wt% of the initial wet mushroom mass. [194]

Table 5.3 A summary of fungal ChNC preparation conditions. Tip sonication was applied to suspensions at 1.00 wt% at a mass of 200 ± 5 .g

Sample	[HCl] (M)	Duration (min)	Temperature (°C)	Tip sonication (min)	Yield (by weight)
fChNC60	3.0	60	reflux	22.5	84
fChNC90	3.0	90	reflux	22.5	45
fChNC180	3.0	180	reflux	22.5	41
fChNC270	3.0	270	reflux	22.5	36

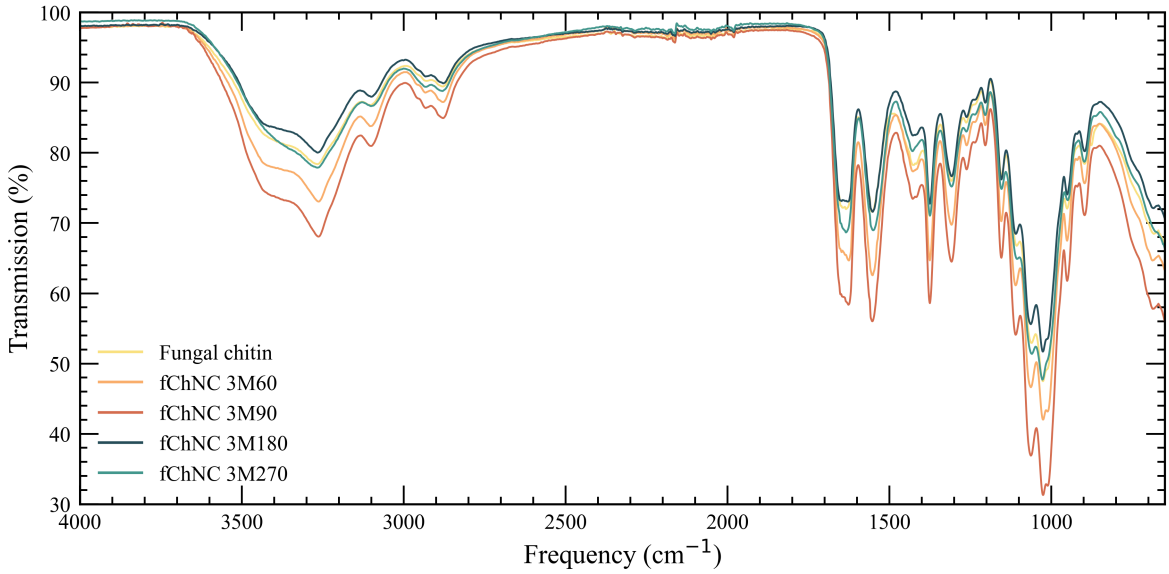

Figure 5.20 FTIR spectra of fungal chitin and the resulting fungal ChNCs. The spectra were consistent with α-chitin but the characteristic amide carbonyl splitting at 1660 and 1620 cm^{-1} were barely resolvable, possibly, due to lower crystallinity compared to shrimp chitin.

5.4.1 Preparing fungal ChNC suspensions

The starting material, from which purified fungal chitin was extracted, was raw mushrooms, as described in the experimental section. The first attempt at producing fungal-derived ChNCs (fChNCs) followed the established 3M540 protocol used for producing shrimp ChNCs. However, a strong dark-grey discoloration was observed following these conditions which immediately indicated that the hydrolysis conditions had to be re-optimised. Consequently, four different fChNC samples were prepared, as summarised in Table 5.3.

Thereafter, the source fungal chitin as well the resulting fChNCs were analysed, starting with their chemical composition. First, the FT-IR spectra show the vibrational stretches at the expected frequencies for α-chitin (Figure 5.20). However, the splitting of the peaks at 1660

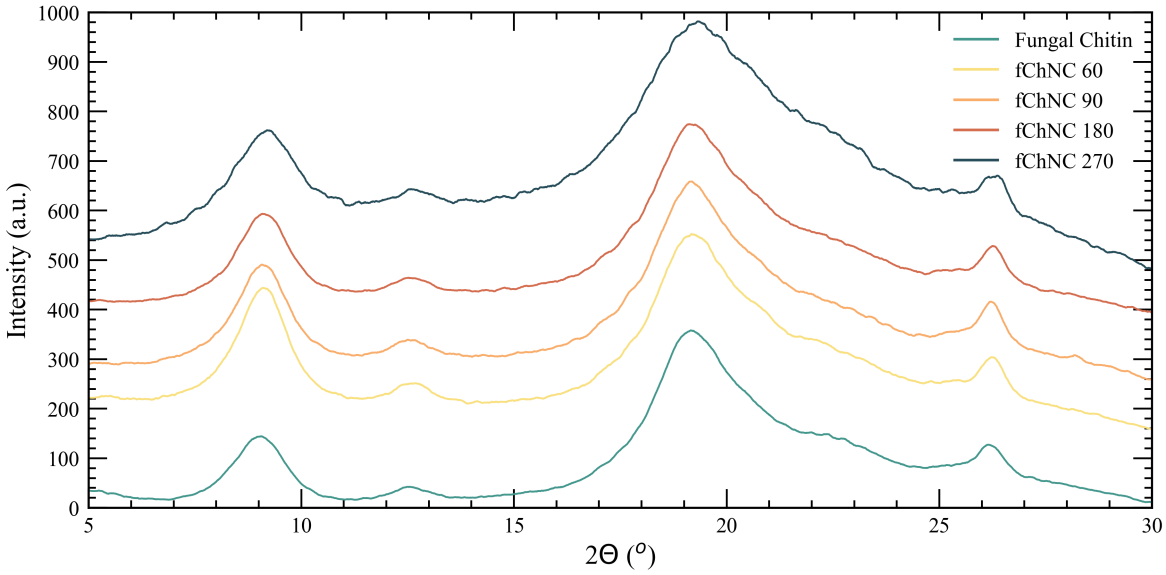

Figure 5.21 pXRD diffractograms of fungal chitin and resulting fungal ChNCs. All the samples have diffraction peaks characteristic for α-chitin (see Table 5.2). 3M270 exhibited broader and less resolved peaks due to over-hydrolysis.

and 1620 cm^{-1} indicative of α-chitin can be barely resolved in comparison to shrimp chitin and shrimp ChNC (Figure 5.1). This suggested a significantly lower crystallinity for fungal chitin and fChNC in comparison to the shrimp analogues. This was confirmed by pXRD diffractograms, which show broader, weak peaks yet in the same positions as recorded for the shrimp derived samples (Figure 5.21). This was most evident for the fChNC270 sample, with the remaining three fChNC samples, hydrolysed for a shorter time, displaying comparable and better defined diffractograms. The non-linearity of the yields with the reaction time also indicated an initial facile hydrolysis of the amorphous regions followed by slower etching of the crystallites, resulting in over-hydrolysis for fChNC270 sample (Table 5.3).

fChNC180 and fChNC270, were further characterised by ^{13}C ssNMR and compared to the source chitin (Figure 5.22). It was immediately evident that fungal chitin was successfully purified from the raw mushroom for it had the characteristic peaks for α-chitin, observed for shrimp chitin as well. However, a minuscule amount of remaining impurities were present, as evidenced by the small peaks at 17.6 and 57.1 ppm. While the spectra of fChNC180 was analogous to fungal chitin, fChNC270 had much broader peaks which were also slightly deviated from the expected positions for α-chitin.

Overall, these results agreed that fungal chitin and resulting fChNC have lower crystallinity in comparison to shrimp derived counterparts. Additionally, the fungal chitin acidic

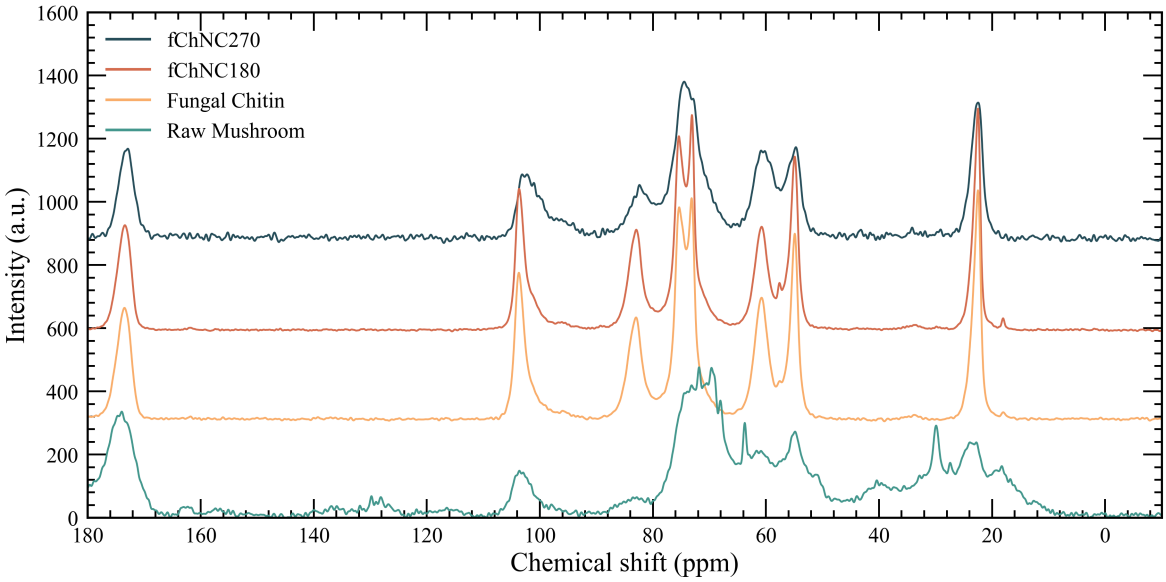

Figure 5.22 ssNMR spectra of fungal chitin and resulting fungal ChNCs. The purification of chitin was successful as indicated by the peaks characteristic for chitin. While 3M180 sample was indistinguishable from chitin, 3M270 showed peak broadening originating from over-hydrolysis.

hydrolysis even at 3.0 M HCl must be carefully timed as the crystal structure starts getting etched resulting in over-hydrolysis of the sample.

Colloidal properties of fungal ChNCs

All fChNC samples dispersed well in aqueous acidic conditions with the ionic strength and HCl concentration set to 60 $mmol_{HCl}/kg_{ChNC}$ by dialysis. The size of the fChNC averaged around 100 nm with it slightly decreasing with prolonged hydrolysis (Figure 5.23 A). TEM analysis revealed that fungal ChNCs were of longer and wider when compared to shrimp ChNCs while the aspect ratio remained the same (Figure 5.17, 5.23 D, E, F). Furthermore, while the ζ-potential as well as the surface charge were not affected much by the fChNC preparation conditions, they consistently had a slightly higher values than recorded for shrimp ChNCs (Figure 5.5 C, 5.23 C). This is likely the result of fungal chitin naturally being more deacetylated than shrimp chitin, however, this difference could not be resolved by ^{13}C ssNMR as the degree of acetylation for fungal chitin was $\sim$98 %.

Liquid crystalline behaviour of fungal ChNC

Concentration series of all four fChNC samples were prepared to study their liquid crystalline behaviour. However, only fChNC90 and fChNC180 exhibited liquid crystalline properties

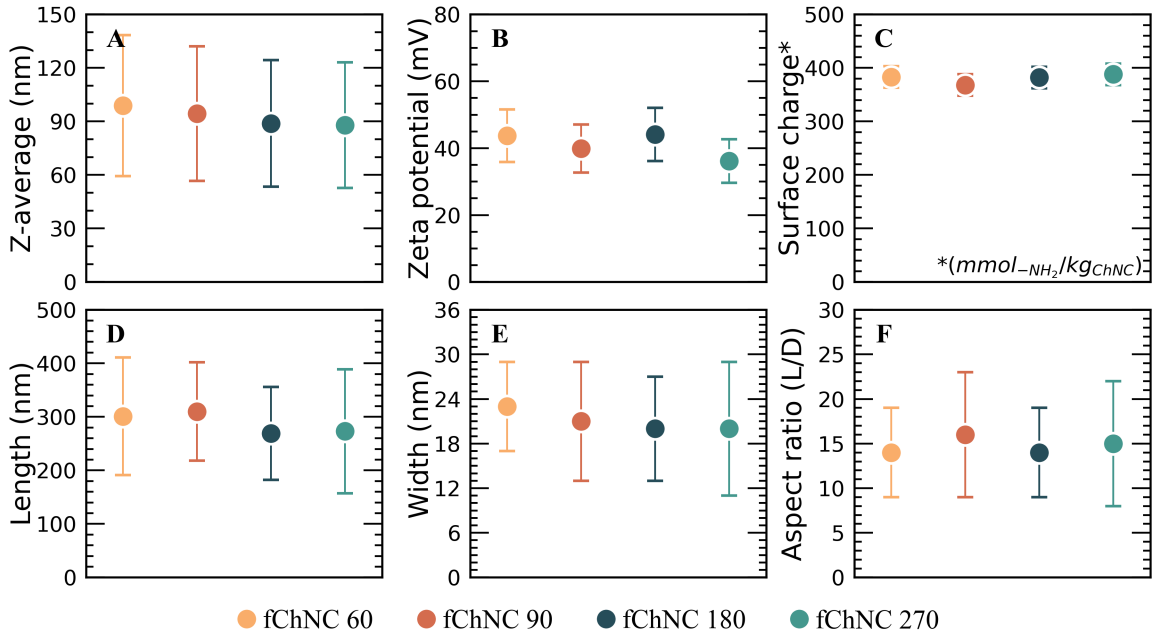

Figure 5.23 The effect of fungal ChNC preparation conditions on their colloidal properties. **A** The Z-average size was found to be around 100 nm on average and decreased only slightly as hydrolysis progressed. **B** ζ-potential indicated that the colloids were sufficiently charged enough to remain stable in suspension. **C** Surface charge as measured by conductometric titration did not depend on the hydrolysis duration and was consistently higher than for shrimp ChNCs reported previously. **D, E, F** TEM measurements of length, width, and aspect ratio were comparable for all the samples. *TEM micrographs were acquired by Gea van de Kerkhof.*

with clear first and second threshold concentrations (Figure 5.24 A). In contrast, fChNC60 and fChNC270 had a sharp transition from fully isotropic to completely anisotropic phases indicating the formation of a gel prior to forming a liquid crystalline phase. While the exact reasons are not clear for this behaviour, this is likely that fChNC60 was not sufficiently hydrolysed while the fChNC270 sample was over-hydrolysed. These findings exemplify that the choice of appropriate hydrolysis conditions for a colloidally stable ChNC suspension, may not be appropriate for the formation of the liquid crystalline phase.

Nevertheless, the intermediate samples, fChNC90 and fChNC180, exhibited a clear transition from isotropic to biphasic phase starting at ∼2.00 wt% (Figure 5.24 A). The amount of anisotropic phase increased as ChNCs were concentrated with fChNC90 becoming fully anisotropic by 3.5 wt%. In comparison, fChNC180 sample at ∼3.5 wt% started to deviate from apparently linear increase in the volume fraction of anisotropic phase, reaching the second threshold concentration at 4.5 wt% (Figure 5.24 A). TEM analysis showed that fChNC90 had on average longer and wider, and slightly lower aspect ratio nanocrystals,

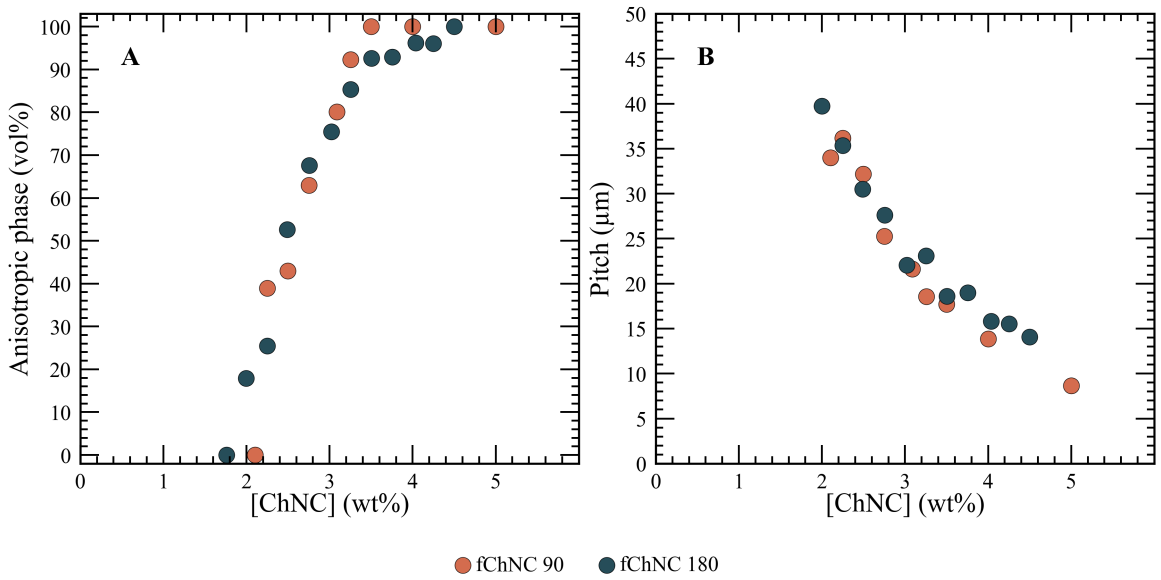

Figure 5.24 Liquid crystalline properties of fungal ChNCs. **A** The amount of anisotropic phase increased as a function of ChNC with both samples becoming fully anisotropic before a surprisingly low concentration of 5.0 wt%. **B** The chiral nematic pitch spanned the 40 to 15 µm range at these low ChNC concentrations.

suggesting a lower second threshold concentration (Figure 5.23). The origin of the deviation from linearity in the phase separation is, however, not entirely clear, but it was also observed for the shrimp ChNC studied at comparable conditions (c.f. b4 ChNC sample in Figure 5.18). It is likely that at the ionic strength and pH used, the contribution of the nanoparticles to the ionic strength becomes non-negligible when they reach higher concentrations. However, it remains unclear why fChNC90 did not exhibit such a behaviour. Further investigation by POM microscopy proved that that both fChNC90 and fChNC180 formed chiral nematic phase evidenced from the observed fingerprint pattern. The chiral nematic pitch diagrams were obtained, which displayed a comparable chiral nematic pitch for both samples spanning the range from ∼15 µm to ∼40 µm (Figure 5.24 B).

5.4.2 Comparing fChNCs and sChNCs

The difference between fChNC and sChNC can be seen from TEM images which when compared side-by-side show that the fChNC appear as longer nanoparticles which is also supported by the statistical analysis (Figure 5.25, 5.17 D, E, 5.23 D, E). This was even more evident from the AFM images, which showed that fChNC appear to be composed of longer fibrils which would also explain for the suspension appearing more viscous in comparison to the shrimp ChNC as it was qualitatively observed that fChNC were more viscous and prone

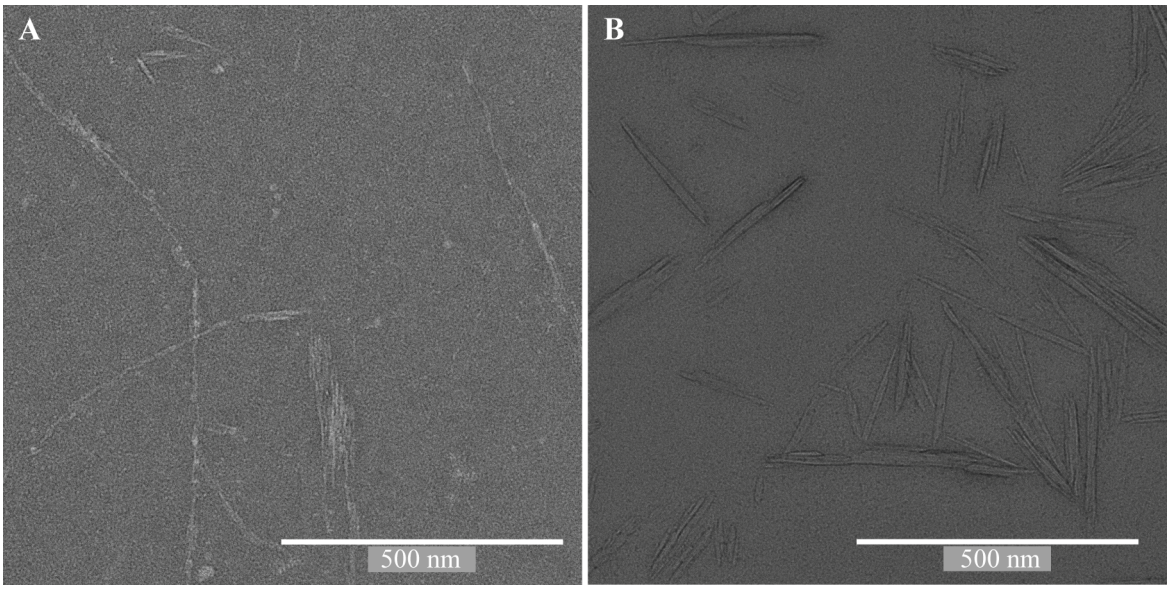

Figure 5.25 Comparison of liquid crystalline properties of fungal and shrimp ChNCs. **A** The amount of anisotropic phase increased as a function of ChNC with both samples becoming fully anisotropic before a surprisingly low concentration of 5.0 wt%. **B** The chiral nematic pitch spanned the 40 to 15 µm range at these low ChNC concentrations.

to trapping air bubbles, making them more difficult to work with (Figure 5.26). The samples also exhibited significant differences in terms of their liquid crystalline behaviour (Figure 5.27). Since the ionic strength and pH is expected to have an impact on the self-assembly and colloidal properties, the best meta-comparison can be established against the shrimp ChNC 3M540 (b4) suspension described in section 5.3.2. The general observations indicated that fungal ChNCs have lower first and second threshold concentrations with the chiral nematic pitch being significantly smaller. For example, at 5.00 wt% fChNC180 was fully anisotropic with the chiral nematic pitch of $\sim$15 µm, while the shrimp-derived equivalent was only $\sim$60 % anisotropic with a striking large chiral nematic pitch of $\sim$200 µm (Figure 5.27). Such a contrast must have resulted from the cumulative differences in surface charge, particle size (despite them having comparable aspect ratio), and crystallinity. Some reports indicate that fungal chitin is decorated with glucans which are similar to chitin, in molecular structure, and difficult to remove and they are even thought to be included in the crystal structure of chitin, which could overall contribute to the outstanding liquid crystalline behaviour of fungal ChNCs. [195, 196] Nevertheless, a direct comparative study would be required to get a better understanding as there is virtually no previous work done on liquid crystalline properties of fungal derived ChNC self-assembly.

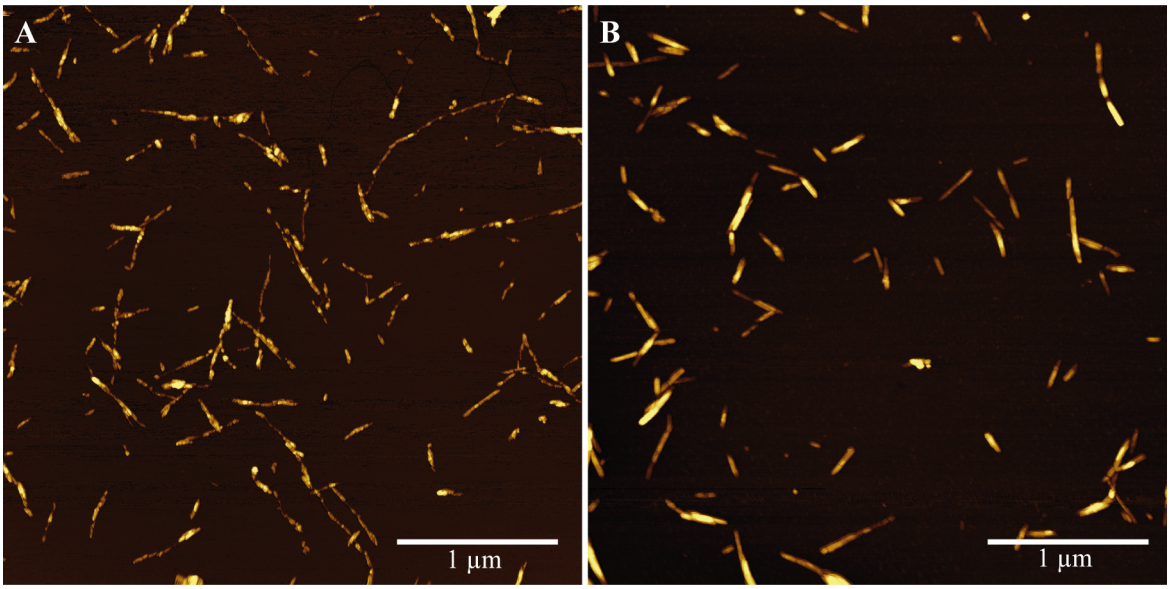

Figure 5.26 Atomic force microscopy imaging of shrimp and fungal ChNCs. **A** Micrograph of fChNCs showing long and thin nanoparticles . **B** Micrograph of sChNCs showing that they are generally better dispersed and appear less fibrillar in comparison to fChNCs.

5.5 Statistical significance

The data presented in this chapter had large standard deviations, which may pose questions regarding the statistical significance of the data. This is especially true in the measurements obtained by TEM (i.e., length, width, and aspect ratio) and DLS (i.e., Z-average). However, sizeable standard deviations originate from the inherent polydispersity of the samples and to establish statistically significant results, at least 500 nanoparticles were measured. Therefore, the fractional uncertainty of the results can be calculated as $\sqrt{N}^{-1}$, which, in this work, is lower than 5 %. [197] Therefore, the difference in average values higher than 5 % in TEM measurements is statistically significant. Large standard deviations on the other hand are useful to assess the polydispersity of the sample, which is believed to have an effect on the nanoparticle self-assembly. [115]

The large standard deviation values reported for Z-average measurements corroborate the polydispersity of ChNC samples. The scattering technique used, namely DLS, performs averaging on the sample since many nanoparticles contribute to measured photon counts when a laser beam illuminates them. In addition, 50 repeats were used to obtain a measurement, which was repeated three times. It is important to note, that the size value obtained is useful in comparing ChNCs prepared under different conditions because of their overall similarity in shape, size, and nature. However, it is erroneous to compare this value to the dimensions measured by TEM, because the value obtained from DLS results from fitting experimental

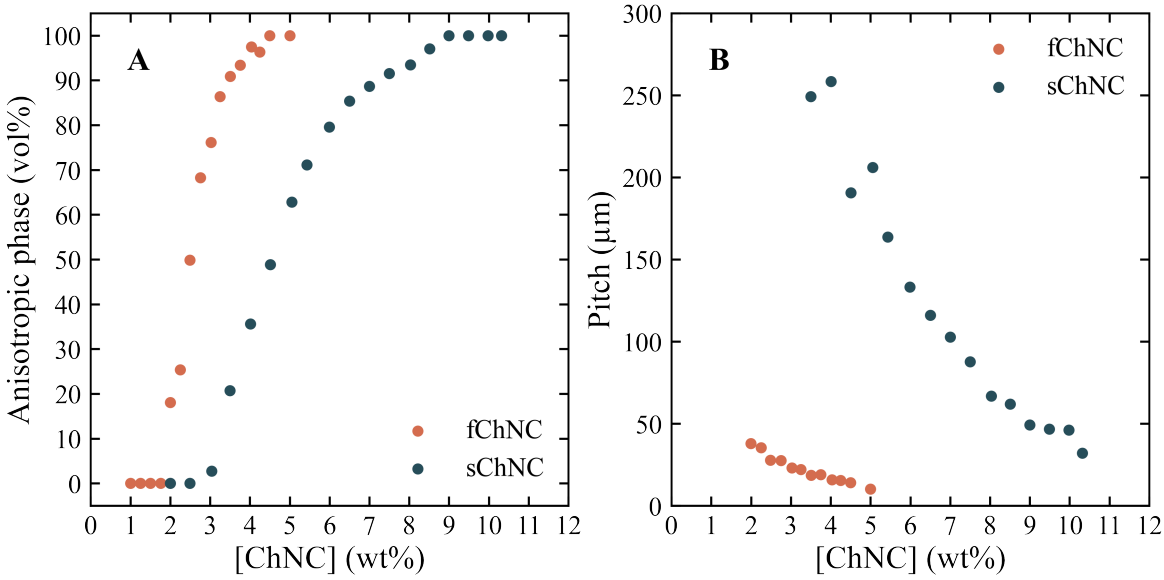

Figure 5.27 Comparison of liquid crystalline properties of fungal and shrimp ChNCs. **A** The amount of anisotropic phase increased as a function of ChNC concentration. Fungal ChNC become fully anisotropic at lower concentrations in comparison to shrimp ChNCs despite comparable ionic strength and pH. **B** The chiral nematic pitch spanned the 15 to 40 µm range for fungal ChNC, while much higher values were obtained for shrimp ChNCs.

results with theory which assumes the diffusion of the spherical body, while ChNCs are more cylindrical than spherical.

The reproducibility of the results can be inferred by comparison of 3M540 sample and Ts2 sample since they were prepared in separate experiments following the analogous preparation conditions (i.e. hydrolysis at refluxing 3.0 M HCl for 540 minutes, following by tip sonication for 4.5 minutes). The reported average TEM length for 3M540 and Ts2 samples were comparable 176 ± 95 nm and 189 ± 99 nm (average value ± standard deviation), respectively. The surface charge measured by conductometric titration were 248 and 246 $mmol_{NH_2}/kg_{ChNC}$. Other parameters like Z-average, width, aspect ratio etc. were equivalent. The same is true for the threshold concentration values for phase separation. Overall, by comparison of samples 3M540 and Ts2 it can be established that the preparation of ChNCs is reproducible. In addition, different fChNC180 suspensions following the same protocol were produced (data not shown) which showed identical self-assembly behaviour.

When comparing fChNC and sChNC suspension, the same standards were employed to when comparing different sChNC suspensions. Therefore, the differences in their size and self-assembly properties are statistically significantly. Nevertheless, it is important to note that fChNC were produced, using never dried chitin purified in the laboratory from the raw mushroom material, whereas sChNC were produced from practical grade shrimp chitin in a

form of dry chitin powder, which was further purified and never dried thereafter. Therefore, the fact that fungal chitin was never dried may contribute to the observed difference between two sources and further studies are needed to confirm the effect that drying and the effect of choosing a different origin. However, the difference in their chemical characterisation (i.e., FTIR, NMR, pXRD) indicate that only drying cannot account for all the differences in the material properties.

Chapter 6

Solid ChNC films

The previous chapter established the limits which the physical dimensions of ChNCs and their surface charge can take. This was the first key challenge to overcome since suspensions need to be colloidally stable to be useful as solid-state hierarchical materials. However, there are at least three additional challenges to be resolved to produce helicoidally structured materials. First, the suspension must form a chiral nematic phase. It was observed to spontaneously occur in many, but not all, of the prepared ChNC suspensions. Second, this liquid crystalline ordering needs to be retained when the suspension is dried to the solid-state. And third, the helicoidal pitch of the nanoarchitecture in solid-state has to be tunable as many of the properties, such as their interaction with visible light or the resistance to the crack propagation, directly depend on the pitch of these structures. [4–6, 17] Throughout this chapter, the ratio of the ionic strength to the ChNC amount is kept constant unless otherwise explicitly stated, to mimic the evolution of the suspension as it dries.

6.1 Ionic strength and pH

These three points are highly interconnected and are expected to depend on the ionic strength and pH during the casting of the film, as they dictate the thickness of ChNC double-layer. Some excellent work has already reported the effects that ionic strength and/or pH can have on ChNC liquid-crystalline behaviour. [10, 24, 33, 61] However, the effect of the ionic strength and pH on drying suspension is far from being fully elucidated, and how these properties in the liquid state influence the helicoidal structure and pitch in solid-state is still not clear. Therefore, the use of ionic strength and pH was used to further the insights on the behaviour changes in liquid crystalline system and they were linked to the solid-state so that the pitch in the solid-state, which influences its functionality, could be tuned.

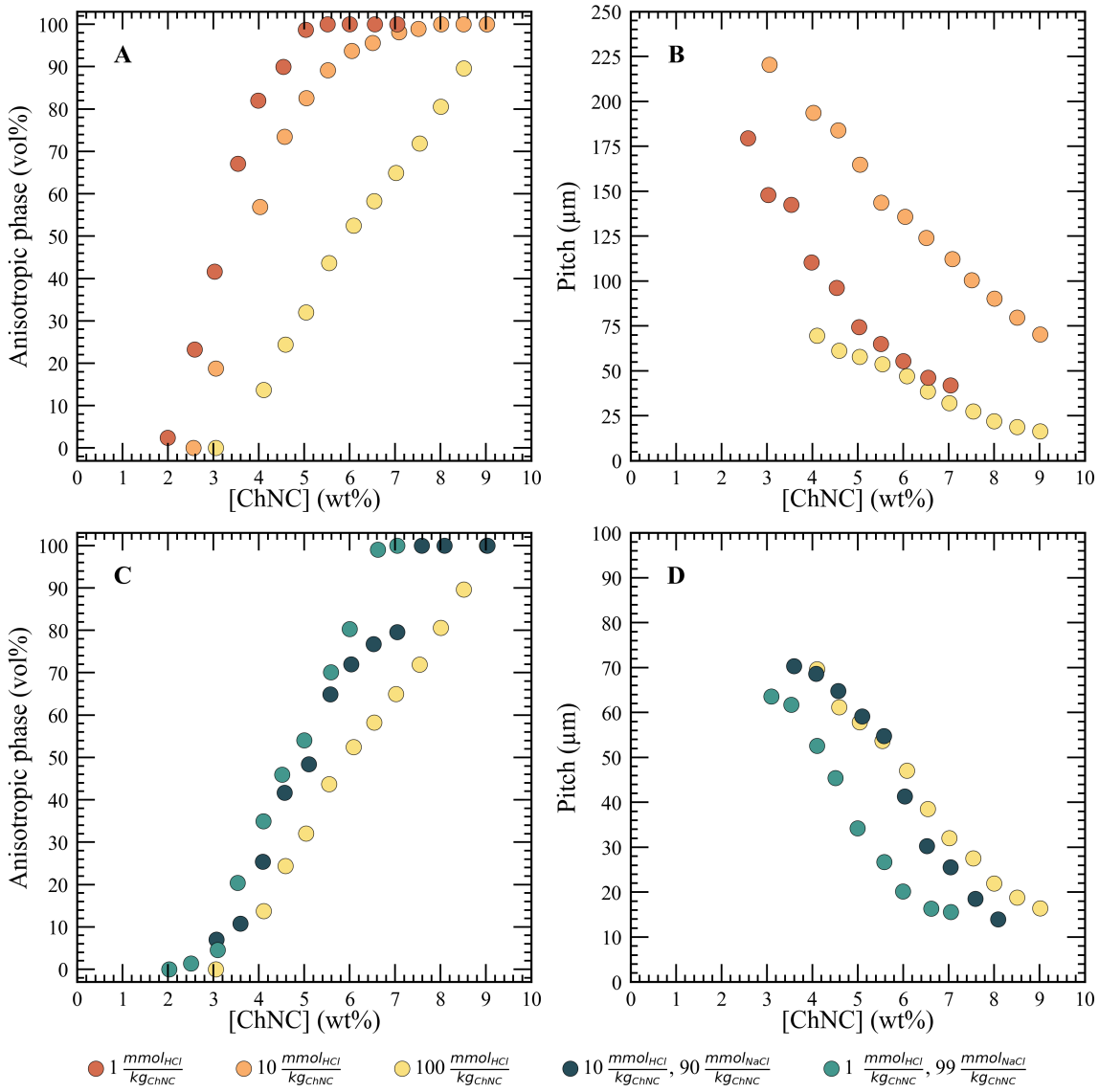

Figure 6.1 Tuning of ChNC self-assembly with ionic strength and pH. **A** Without fixing the ionic strength, increasing HCl concentration led to a higher second threshold concentrations. **B** Chiral nematic pitch first increased but then decreased when HCl concentration was increased without offsetting the ionic strength, making pitches as high as 250 µm and as low as 15 µm accessible. **C** Phase diagrams showed significant changes to the threshold concentrations when HCl concentration was varied with the ionic strength kept identical with NaCl. **D** Pitch diagrams indicated that lower HCl concentration while the ionic strength was kept the same lead to lower chiral nematic pitch

The pH of the suspension influences the surface charge of ChNCs via protonation of surface amines. This inherently affects the double-layer and thus has to be taken into consideration. However, modulation of the pH is also inevitably linked to the ionic strength

as both parameters depend on acid concentration. It is important to note the sensitivity of the system to the absolute ionic strength, which when above 25 mM, results in aggregation observed by the increased turbidity and viscosity. This is the primary reason of why buffer solutions, commonly used to get a robust pH value, cannot be used when working with ChNCs suspensions as their use requires high concentrations of ions resulting in the collapse of the double-layer which results in aggregation of the suspension. Therefore, to better understand the effects that ionic strength and pH have on the suspension and, importantly, the ultimate pitch in the dry state, shrimp ChNC 3M540 Ts3 suspension, which was described in section 5.2, was used.

To decouple the effects of pH and ionic strength, a series of ChNC suspensions were prepared with varied HCl concentration, but with a fixed total ionic strength. This was achieved by dialysing 1.00 wt% ChNC suspension against aqueous HCl and NaCl solution to achieve 100, 10, 1 $mmol_{HCl}/kg_{ChNC}$ (with the remaining ionic strength supplied with 0, 90, 99 $mmol_{NaCl}/kg_{ChNC}$, respectively). The amount of HCl or NaCl present here are normalised by the weight of dry ChNC mass, which remains constant when the suspension is dried, thus mimic the drying process required to produce solid-state films.

The HCl concentration exhibited an obvious influence on ChNC phase separation (Figure 6.1 A). The resulting phase separation behaviour is related to the aspect ratio, as originally suggested by Onsager. [52] However, when considering charged rods, such as ChNCs, the effective dimensions should be considered rather than their physical dimensions as measured by TEM. This is because each ChNC is charged and thus has its own double-layer. When the double-layers overlap, the ChNCs repel each other. The complete interaction energy profile is extremely complicated to calculate, and the approximation can be applied that the ChNCs with their double-layer behave as if they were just non-interacting nanoparticles which cannot intersect but are of larger dimensions than bare ChNCs as measured by TEM. Thus, the new dimensions of nanoparticles will be termed the effective diameter, D_{eff}, and effective length, L_{eff}. Assuming the cylindrical symmetry that such nanoparticles have, both effective dimensions can be assumed to be equal to the sum of the relevant physical dimension and twice the thickness of the double-layer. It is important to note that the size of the double-layer would contribute relatively less to L_{eff} than to D_{eff} because the physical diameter, as measured by TEM, is on the order of magnitude lower than the physical length.

By increasing HCl concentration, while keeping the ionic strength to nanoparticle concentration constant, a larger proportion of amines becomes protonated which results, contrary to an intuition, to a less expanded double-layer (see Appendix A). This is only true because the chosen HCl concentrations correspond to pH values ranging from 3 to 5, which are lower but still close to the average pKa_H of the chitin amine which is around 6.3. [10] Using an

approximation from Henderson-Hasselbalch equation, relating the degree of dissociation with the pH and pKa, it can be derived that at 1 $mmol_{HCl}/kg_{ChNC}$ (pH = 5 at 1.00 wt%) only about 80% of all amines will be protonated. However, it can be expected that actually slightly lower number of amines will be protonated at given conditions because two charged groups in close proximity would be less favoured, meaning that the protonation becomes less favoured as the protonation increases. This would mean that there may be in fact a slightly larger difference between the proportion of amines protonated when HCl is varied from 1 to 100 $mmol_{HCl}/kg_{ChNC}$ than simply expected from the above mentioned approximation.

The increase in protonation state, manifests in decreasing D_{eff} because of the increased surface charge (see Appendix A). Therefore, the effective nanoparticle volume gets smaller which is consistent with the observations that the second threshold concentration increased at higher HCl concentrations. In contrast, however, the first threshold concentration, C_I, remains constant, which is an expected behaviour since for the polydisperse ChNCs suspensions, the first nanoparticles to undergo phase separation are the large ones and given their large dimensions, the effective dimensions are only insignificantly affected by the double-layer term. Whereas the second-threshold concentration, dominated by the self-assembly of the smaller nanoparticles, shifts as a consequence of the double-layer having a significant contribution to the D_{eff} and thus effective volume (Figure 6.1 A).

The chiral nematic pitch was also strongly affected by the pH of the ChNC suspensions (Figure 6.1 B). The increasing HCl concentration, as described above, results in a more expanded double-layer. This, in turn, forces the *physical* ChNC particles to be spaced further apart on average. Consequently, the chiral interactions, like most, become weaker as the average distance between physical particles increased resulting in the overall weaker twisting and thus larger chiral nematic pitch. However, as pointed out above, the surface charge depends on HCl concentration in a non-linear fashion, raising it from 1 to 10 $mmol_{HCl}/kg_{ChNC}$ results in large increase in the proportion of protonated amine groups but any further increase in HCl concentration is expected to increase the surface charge only marginally. This helps to rationalise the changes in the chiral nematic pitch, which level off with further increase in HCl concentration (Figure 6.1 B).

Alternatively, the pH can be varied without maintaining a constant ionic strength to ChNC ratio, i.e., by varying the concentration of HCl without the addition of NaCl, which leads to a complex liquid crystalline behaviour. not only the pH but also the ionic strength to nanoparticle ratio varies at the same time leading to excitingly complex ChNC liquid crystalline behaviour (Figure 6.1 C, D). When the samples prepared with 1, 10, and 100 $mmol_{HCl}/kg_{ChNC}$ are compared, the second threshold concentration increased dramatically from 5.0 to 9.0 wt% (Figure 6.1 C). This signifies the importance of the ionic strength

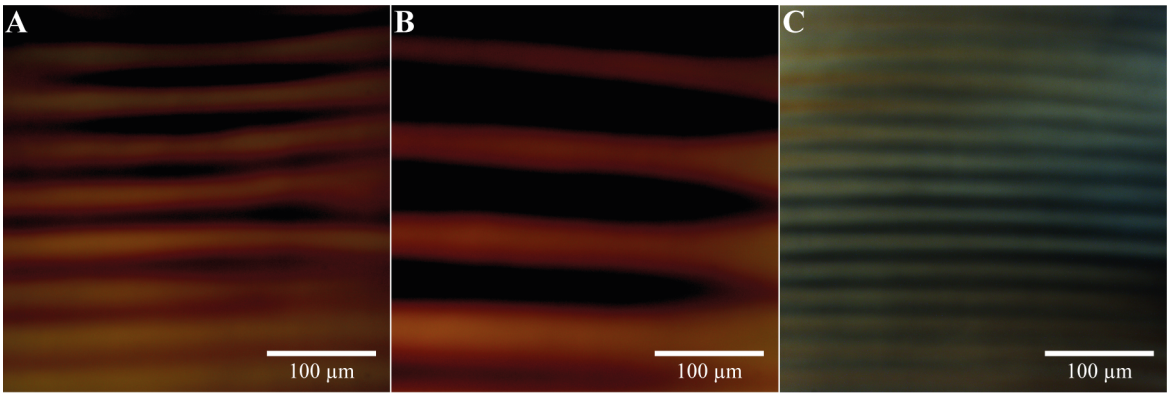

Figure 6.2 Polarised optical microscopy micrographs of ChNC suspensions at different HCl concentrations. **A, B, C** ChNC suspensions at 5.0 wt% dialysed to set the HCl concentration equivalent 1, 10, and 100 $mmol_{HCl}/kg_{ChNC}$, respectively, without correction for the differences in ionic strength to nanoparticle concentration by using NaCl. The chiral nematic pitch, defined as the twice periodicity, varies significantly depending on the suspension conditions used.

since, as previously described, by just varying the surface charge the same trend, but not as prominent, was observed. In contrast, the trends in the chiral nematic pitch diagrams appear more complex (Figure 6.2). ChNCs in the presence of 1 $mmol_{HCl}/kg_{ChNC}$ exhibit a large chiral nematic pitch on the order of tens to hundreds of micrometres. This already large chiral nematic pitch increased even further at ten-fold higher HCl concentration (Figure 6.1 D, 6.2). This can be explained by the changes in the surface charge dominating over the ionic strength at this regime. However, a further increase in HCl concentration to 100 $mmol_{HCl}/kg_{ChNC}$ resulted in a collapse of the chiral nematic pitch, giving the lowest values out of the three samples studied. From 10 to 100 $mmol_{HCl}/kg_{ChNC}$, only the ionic strength is expected to significantly increase, resulting in a contraction of the double-layer and so the physical nanoparticles could get in closer proximity, leading to stronger chiral interactions.

6.2 From a chiral nematic suspension to a solid film

Once control over the self-assembly process was established, these suspensions were then dried to yield solid-state films. When the cross-sections of these films were inspected by scanning electron microscopy (SEM), a helicoidal (also known as Bouligand [4]) structure was observed (Figure 6.3 B, C). This helicoidal structure, the chiral nematic structure equivalent in solid-state, was also found to have a variation in pitch depending on the initial suspension conditions (Figure 6.3 A). To understand these results, it is imperative to consider the processes, which occur during the suspension drying in the process of making such films.

5 different ChNCs suspensions, 4.0 g of each at 2.0 wt% concentration, were cast in separate Petri dishes. Over time, due to water evaporation, the ChNC concentration increased to reach the threshold concentration and the chiral nematic phase started to form. With continuous drying, the suspension became concentrated enough so that the entire suspension became chiral nematic. As the ChNC concentration continued to increase, the chiral nematic pitch continued to decrease as the system was readjusting itself to reach the thermodynamic minimum. However, eventually it reached the point known as the kinetic arrest.

At this point of kinetic arrest, the suspension becomes so viscous that the ChNCs nanoparticles are virtually trapped in their position. This can result from either the repulsive or attractive gel formation. The former occurs at ChNC concentration when the nanoparticles, with their extensive double-layers, are forced in such a close proximity to the neighbouring rods, that they cannot reorient, resulting in effectively kinetically trapping the system in place. Alternatively, an attractive gel can be formed if the double-layer shrinks so much that the physical nanoparticles can come in such a proximity so that the attractive van der Waals forces take over. Such attractive interactions can cause the formation of a percolating network of aggregated ChNCs, which also result in freezing the structure. The exact mechanism depends on the initial ionic strength since it increases with ChNC concentration as the suspension dries. Essentially, the point of kinetic arrest, regardless of the mechanism, occurs at the ChNC concentration at which the system cannot not develop to reach thermodynamic minimum anymore but is in the kinetic minimum and stays there. At this point of kinetic arrest, the suspension becomes like a gel with the trapped chiral nematic ordering of ChNCs. This is in contrast to molecular liquid crystals, which, despite being able to form chiral nematic phases in liquid state, cannot be gelled to retain the ordering.

Past the point of kinetic arrest, the gel-like suspension continues to dry and shrink. Since in this gelled state the chiral nematic phase is trapped, it is forced to shrink as well. [76] The amount by which the system shrinks depends on the volume change and the geometry. Since the suspensions were dried in Petri dishes as well as the suspension completely wetted the whole bottom surface (and remained fully wetting until it fully dried), only a unidirectional compression at the direction perpendicular to the suspension/air interface can be assumed. The amount by which the systems compresses can then be approximated to be directly proportional to the volume change. This can be expressed in terms of the change in ChNC concentration when expressed in volume, rather than weight, percentage, which can be done easily since the density of chitin has been reported previously to be 1.425. [198] From this follows that if the point of kinetic arrest is known, the amount by which the suspension, and the chiral nematic pitch, is compressed can be calculated. However, the actual effect on the chiral nematic pitch can be complicated by the alignment of the chiral nematic phase. [7] For

chiral nematic structure with the helical axis **m** perfectly parallel to the shrinkage direction, as is expected for ChNC suspension in a Petri dish, the chiral nematic pitch will be indeed compressed as expected. This compression then continues until the suspension is fully dry i.e., reaching 100 vol%.

Ultimately, starting from the formation of the chiral nematic phase to the point of kinetic arrest and the compression, solid-state films with helicoidal nanoarchitecture structure are formed 6.3). The helicoidal pitch is thus determined by the chiral nematic pitch at the point of kinetic arrest and the ChNC concentration at which this happens as it effectively determines the amount of the compression followed. In fact, the 5 different conditions used resulted in films with helicoidal pitch which could be tuned from ∼650 to ∼5,000 nm (Figure 6.3).

Alas, it is not trivial to determine the point of kinetic arrest. While rheology seems to be the obvious answer, it would be a tedious process requiring enormous amounts of material, concentrated at various concentrations and at various ionic strengths and pH. In addition, chiral nematic liquid crystals are known to exhibit shear thinning effects, meaning that their rheological measurement upon the application of shear may not be able to accurately determine the point of kinetic arrest in the first place. [136]

Nevertheless, it is possible to roughly approximate the point of kinetic arrest from the capillaries prepared to study ChNC liquid crystalline properties. The capillaries which appeared entirely anisotropic have exhibited fingerprint pattern, however, as the concentration was further increased the suspension was still anisotropic, yet the chiral nematic pattern would not develop. This indicates that the suspension is highly viscous, which inhibits it to relax from alignment of nanoparticles which was induced due to the shear experienced when the suspension was sucked into the glass capillary. Since the nanoparticles are, to a first approximation, rod shaped, they would align with their long axis along the shear direction. [33] Even after a month, the phase did not appear to relax into a chiral nematic phase as the fingerprint pattern could not be observed. The concentration at which this is first observed, was approximated as the point of kinetic arrest, (though it is likely to be a slight underestimate). While it gives the concentration at which the point of kinetic arrest occurs, it does not provide another crucial parameter - chiral nematic pitch. Therefore, to be able to predict the pitch in a solid-state it was necessary to assume the kinetic arrest to have happened at the highest ChNC concentration which still exhibited the chiral nematic ordering. From this point onwards, the pitch will decrease as $pitch = [ChNC]^{-1} + const.$ due to the unidirectional compression as described above.

This approach was applied to relate the liquid crystalline behaviour with the helicoidal nanoarchitecture in solid-state which was measured by SEM (Figure 6.3 A). On the log-log scale, the geometrical compression past the kinetic arrest appears as a straight line with

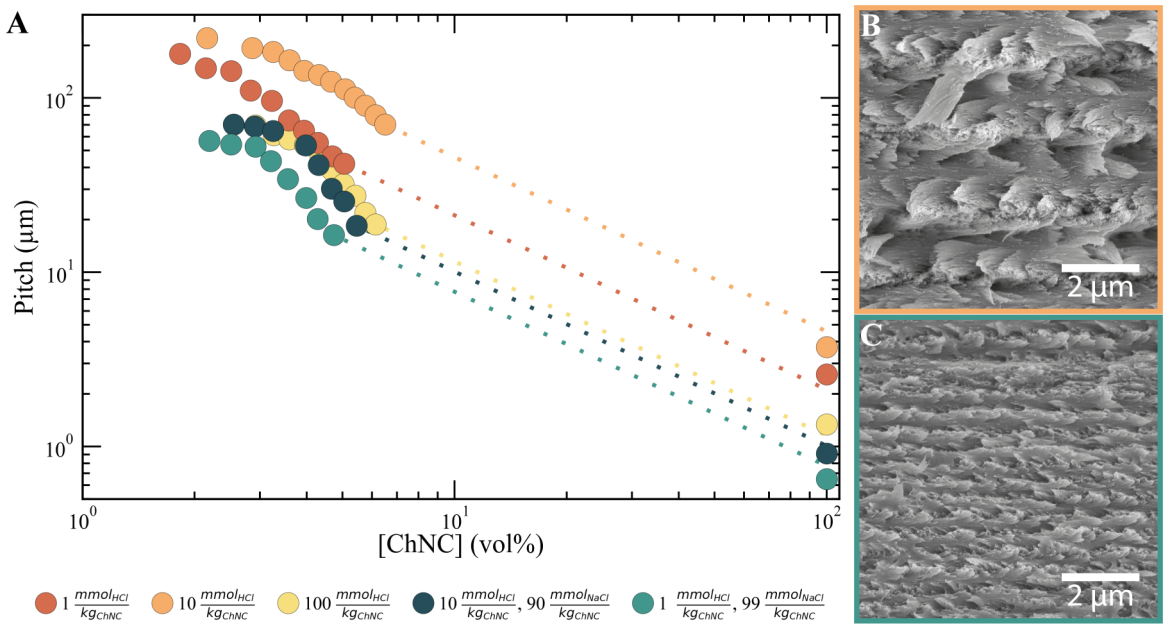

Figure 6.3 Tuning of the helicoidal pitch in solid-state films by tailored ChNC self-assembly and gelation. A ChNC of different ionic strength and pH exhibited different liquid-crystalline properties where the kinetic arrest was assumed to occur at concentration at the last measured point. A unidirectional compression was assumed to have followed during which the pitch decreased as $pitch = [ChNC]^{-1} + const.$ indicated by the dotted lines. This predicted the pitch in solid-state with 20% with respect to SEM measurements. **B, C** SEM cross-sectional images of the films with the largest and smallest pitches, respectively.

a slope equal to -1 (dotted lines in Figure 6.3 A). Such an extrapolation for suspensions of various pH and ionic strengths as studied, successfully explains the observed trends in the solid-state. The predicted pitch values at 100 vol% ChNCs reasonably agreed with the experimentally determined ones by cross-sectional SEM analysis (Figure 6.3 A). The error of $\sim$20 % between the predicted and measured values most likely resulted from the underestimation of the point of kinetic arrest and the solid-state films not being 100 vol% ChNC because of some residual water. Nevertheless, given its simplicity, this model allows for a reasonable correlation between the effects of various pH and ionic strengths on the liquid crystalline behaviour of the suspension with the helicoidal pitch in the solid-state ChNC films.

Materials with an exceptional resistance crack propagation is one of the possible applications for such helicoidally ordered films. This behaviour has been observed in crab shells and mantis shrimp claws where they have helicoidal structure with pitch as large as tens of micrometres. [4, 199] It would be indeed an interesting future direction to investigate the mechanical performance of ChNC helicoidal films as a function of helicoidal pitch size.

With the further suspension optimisation, the pitches reaching tens of micrometres may be possible to achieve which is what is found in mechanically robust natural helicoidal materials. [4]

Alternatively, the helicoidal structures with a pitch comparable to the wavelength of visible light is expected to yield structurally coloured materials. This has been observed in various beetles belonging to the scarabaeidae family, [17] The reflected wavelength of light from the helicoidal structure can be successfully predicted using Bragg's law: $\lambda = n_{avg} \times pitch$. Given that the average refractive index, n_{avg}, for chitin is 1.54, the ChNC film with the lowest helicoidal pitch of 650 nm, is expected to reflect light at $\lambda = 1,000$ nm. This wavelength corresponds to the near-IR and is invisible to the human eye. Thus, a solid-state film with a helicoidal pitch of <∼450 nm is required to obtain reflection at wavelengths visible to human eye <∼700 nm. To achieve that a ChNC suspension with significantly different liquid crystalline properties is required. Such suspensions were already studied in Section 5.4.

6.2.1 Fungal ChNC films

The use of the fChNC180 suspension described above in Section 5.4 was motivated because it undergoes phase separation at especially low ChNC concentrations with it becoming fully anisotropic at ∼4.5 wt%. The analogous suspension drying approach was used to predict the pitch in the solid-state resulting from fChNC180 suspension studied above. The point of kinetic arrest was approximated to occur at ChNC concentration of 4.5 wt% which is equivalent to 3.20 vol%. At this concentration, the chiral nematic pitch reached a value of 15 µm (Figure 5.24). Interestingly, throughout the whole study, the chiral nematic pitch values in ChNC suspensions never went beyond ∼15 µm. In fact, similarly low chiral nematic pitch values were observed for several different shrimp ChNC suspensions, but, in all the studied cases, it occurred at significantly higher ChNC concentration. This is crucial because, as described above, the point of kinetic arrest can be successfully assumed to occur at concentrations slightly higher than the concentration when the entire suspension becomes fully anisotropic. Essentially this fChNC180 suspension, the chiral nematic pitch is expected to be compressed more by geometrical compression because of the expected onset of the kinetic arrest at lower nanoparticle concentration in comparison to other sChNC suspensions.

Therefore, by considering the liquid crystalline behaviour followed by the kinetic arrest and geometric compression, for fChNC180 suspension dried in a Petri-dish with the chiral nematic structure perfectly aligned, the helicoidal pitch in a solid-state was predicted to reach ∼430 nm. With chitin average refractive index, n_{avg}, to be equal to 1.54, such a structure, based on Bragg diffraction formalism ($\lambda = n_{avg} \times pitch$), would be expected to reflect the

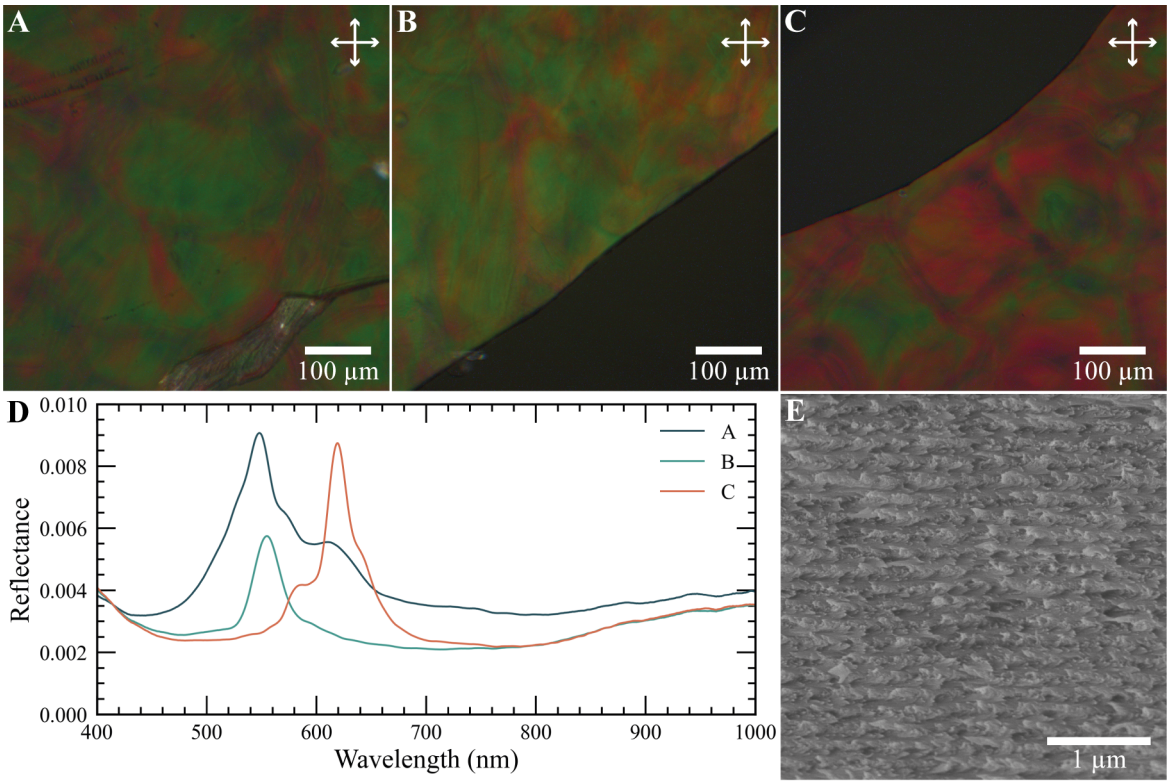

Figure 6.4 Structural colouration in fungal ChNC films. **A, B, C** Structural colouration was observed by optical microscopy when imaged in reflectance with crossed-linear polarisers. **D** Corresponding reflectance spectra. **E** The cross-section of such a film revealing helicoidal architecture with a small pitch.

light at the ∼660 nm wavelength. This corresponds to the red colour, visible to human eye, however, this film did not strike as particularly coloured and, frankly, they just looked plain and transparent. This is surprising given that SEM cross-sectional analysis of the film confirmed the presence of the helicoidal architecture with a pitch of 390 ($\sigma = 92$) nm (Figure 6.4 E).

This apparent dichotomy was resolved by employing polarised optical microscopy (Figure 6.4 A, B, C). Weak structural colouration became evident when the sample was imaged in reflection between two crossed linear polarisers. In this configuration, the specular reflection from the air/film interface, reflecting ∼10 % of visible light, was removed, allowing the exposure of the camera to be set high without a complete over-saturation, which revealed red and green domains, as expected from the pitch measured by SEM (Figure 6.4 A, B, C). The fact that there are domains of different colours indicates inhomogeneities in the solid-state as different helicoidal pitches are required for such a phenomenon to manifest. The continuous chiral nematic mesophase forms from merging ChNC tactoids, sphere like formations with

a higher local ChNC concentration, which form spontaneously followed by sedimentation. This continuous phase develops over time to become more uniform and while it is fast initially, the development slows down significantly over time as the system approaches a completely aligned and uniform phase. However, many separate domains develop, which have the same chiral nematic pitch but a tilted helical director, **m**, with respect to the air/suspension interface. Once the kinetic arrest happens, such domains with different tilts are locked and cannot reorient anymore to reach the ultimately homogeneous structure. Then, the following compression happens at a direction perpendicular to the air/liquid interface. If the chiral nematic helical director, **m**, is parallel to the compression direction, it gets maximally compressed and results in a smaller helicoidal pitch in solid-state. In contrast, as the angle between the compression direction and the helical director increases (i.e., the tilt increases), the chiral nematic pitch is compressed less, resulting in larger helicoidal pitches in solid-state. The continuous chiral nematic phase is overall well aligned and, therefore, only a limited distribution of tilts is expected, resulting in a limited variation in colour explaining the presence only of red and green. This variation was also captured but more quantitatively by measuring reflectance spectra (Figure 6.4 D). These measurements, performed with normalisation to the silver mirror, also revealed that this structurally coloured ChNC film reflected less than 1% of visible light, explaining the lack of visible colouration when observed by a naked eye.

Nevertheless, it was not apparent why the reflectance was so weak from a seemingly well-ordered helicoidal film (Figure 6.4), given that in nature similar structures lead to a variety of vivid colours. [17, 78] Similarly, helicoidally nanostructured films, made of cellulose nanocrystals (CNCs), are strongly reflective and brightly coloured (Figure 2.6). [13] Importantly, however, these results represent the first reported instance of structural colouration in a material made entirely of chitin and as such deemed interesting to investigate these films further. It is interesting to understand the reasons behind the weak reflectance from these structures as well as whether and how it could be improved. Besides, it is interesting whether the ionic strength and pH used to study fChNC180 previously was just a lucky coincidence resulting in pitch small enough to produce structural colouration. This latter point is investigated next.

Tuning of the reflected colour

As just discussed above, the reflected colour is directly related to the helicoidal pitch and the refractive index of the building blocks via Bragg's diffraction law: $\lambda = n_{avg} \times pitch$. The refractive index is a constant material property and cannot be changed unless the material itself is changed. In contrast, the helicoidal pitch can be tuned by adjusting the liquid

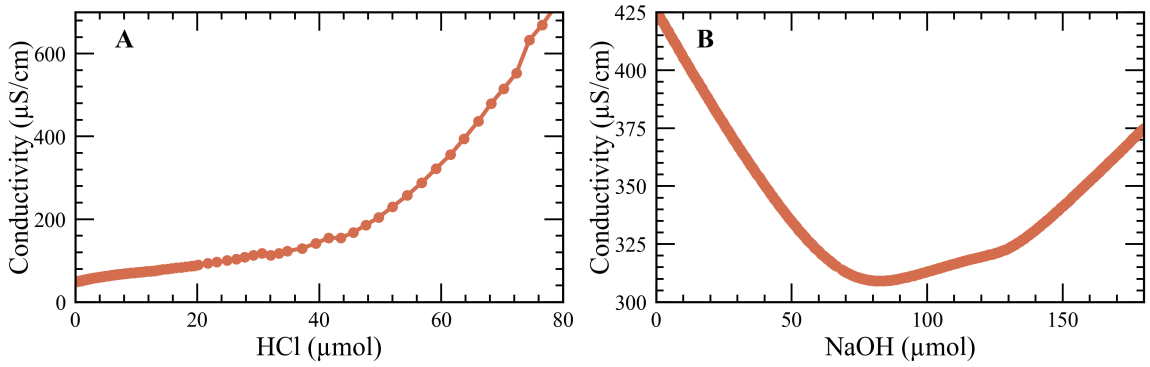

Figure 6.5 Fungal ChNC titrations used to fine tune surface charge. **A** Conductometric titration of fChNC, extensively dialysed against Milli-Q, with HCl. **B** Conductometric titration of fChNC using NaOH with a prior addition of HCl to determine the total number of amine groups.

crystalline properties as well as the onset of the kinetic arrest. In fact, this was already shown that by adjusting ionic strength and surface charge by protonating different proportions of surface amines, the helicoidal pitch can be controlled (see Section 6.2). However, while the previous approach to adjust the ionic strength and pH by dialysis has its merits, it is tedious, especially when several combinations are to be inspected. Hence, an alternative strategy was devised whereupon the fChNC180 suspension, at ∼3.0 wt% was extensively dialysed against Milli-Q water to ensure that only negligible amounts of ions remain. Then HCl and/or NaCl solutions were added directly into suspension to attain various ionic strengths and surface charges. However, to infer these parameters from the amount of added HCl and NaCl required two different types of titration experiments since HCl can increase the proportion of protonated amines as well as the ionic strength.

First, the suspension was titrated using HCl, where the conductivity was recorded after each incremental addition of HCl (Figure 6.5 A). The resulting conductometric titration curve appeared to have two regimes. Initially shallower slope indicates the slow increase in conductivity with added HCl, which refers to the absorption of HCl by surface amines, and thus only minimally increasing the concentration of freely moving ions, given the minute effect on the conductivity. Essentially, it was assumed that the ionic strength did not increase at this regime which was also supported by the fact that the viscosity of the suspension remained high, evidenced qualitatively by the suspension trapping air bubbles during stirring that remained stable for minutes if left undisturbed. This behaviour is indeed expected for ChNC suspensions at extremely low ionic strengths because of the extensive double-layer causing the nanoparticles to be crowded which macroscopically appears as repulsive gel (or Wigner glass). [35–37] With continuous addition of HCl a point was reached when the

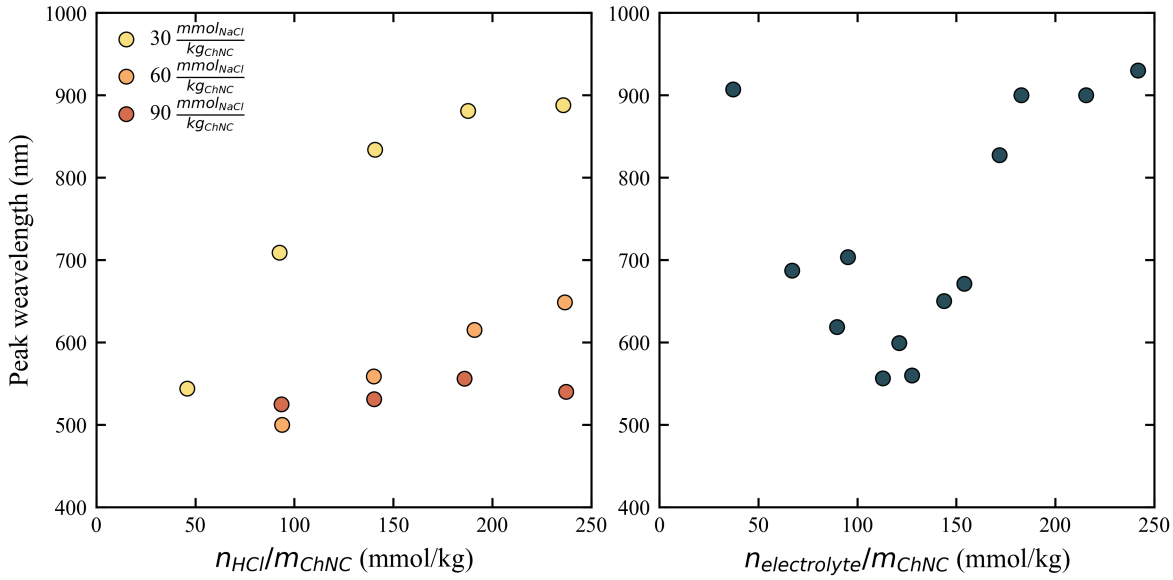

Figure 6.6 Controlling reflection the average bandwidth of fungal ChNC films using ionic strength and HCl. **A** Reflected average peak wavelength tuned as a function of added HCl which changed the surface charge at three different ionic strength conditions. **B** Reflected average peak wavelength tuned as a function of added electrolyte when all the surface amines are fully protonated.

suspension stopped trapping air bubbles indicating a significant decrease in viscosity, which can be related to an increase in ionic strength. In fact, at this point the titration curve shifted to the second regime, with a steeper slope, where added HCl acts simply as an electrolyte to increase the ionic strength. This titration gave the number of amines that can be protonated for the suspension equilibrated against Milli-Q.

Then, a second conductometric titration was performed using NaOH (Figure 6.5 B). The same fChNC suspension was titrated but supplemented with an excess of HCl before the experiment to ensure that all the surface amines are protonated. As a result, a titration curve with three regimes was obtained, indicating the titration of free HCl, followed by titration of protonated surface amines and finally the addition of NaOH, which merely increased the ionic strength. From this experiment, the number of all available surface amines could be determined.

When these two titration experiments were combined, it was determined that $\sim$100 $mmol/kg_{ChNC}$ of amines are protonated after the dialysis against Milli-Q while the maximum number of available amines for fChNC180 was 320 $mmol/kg_{ChNC}$. While reaching values below $\sim$100 $mmol/kg_{ChNC}$ quickly led to the colloidal aggregation, any value in between $\sim$100 and $\sim$320 was readily available by simple addition of pre-calculated amount of HCl. In addition, it allowed to also determine the proportion of added HCl that is in excess and

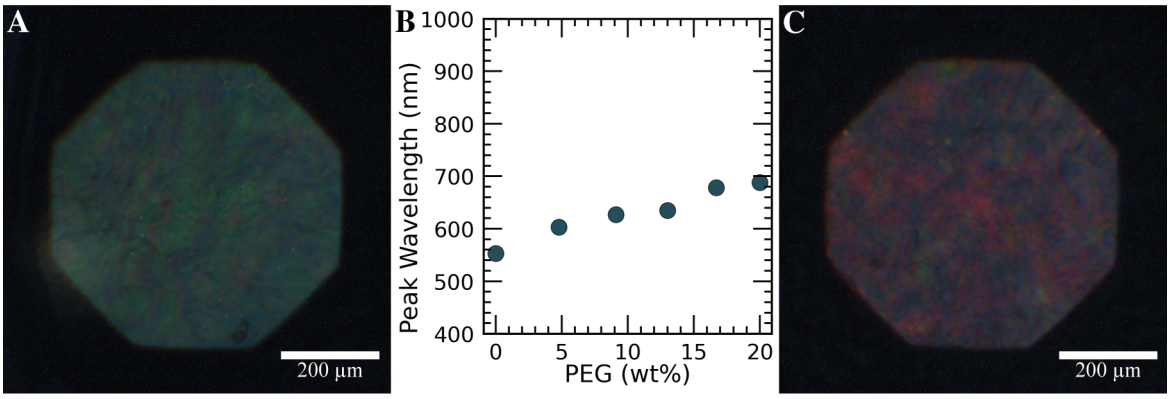

Figure 6.7 Tuning the reflection bandwidth of fungal ChNC films using PEG. **A** Initially the film appears green reflecting at around 550 nm. **B** Sequential addition of PEG causes a controllable red shift in reflection. **C** With 20 wt% PEG in the final structure, a red film can be obtained.

only contributes to the ionic strength. Since both excess HCl and NaCl are composed of monovalent ions, they equally contribute to the ionic strength and thus can be collectively referred to as the electrolyte, simplifying things.

Thereafter, several fChNC films were cast with various combinations of HCl and NaCl to tune the surface charge and ionic strength and, consequently, infer their effect on the reflected wavelength and helicoidal pitch. By increasing the amount of added HCl, the surface charge of fungal ChNCs was tuned resulting in a red shifting effect (Figure 6.6 A). To reduce the viscosity of the suspension, the ionic strength had to be increased by adding NaCl as otherwise the films with many air bubbles would be formed as well as risking the inhibition of the chiral nematic phase formation. Interestingly, it was found that by altering the surface charge at lower ionic strength (30 $mmol_{NaCl}/kg_{ChNC}$) the average peak reflected wavelength could be shifted from 550 to 900 nm. The effectiveness to tune the reflected colour by altering surface charge, however, diminished as the ionic strength was increased. This was attributed to the higher ionic strengths dominating over the changes in the double-layer size with the increase in the surface charge having a minimal effect. In effect, the increase in the ionic strength resulted in a blue shift in the reflected colour. In fact, it could be most clearly seen at a fully protonated ChNC suspension (Figure 6.6) B). Interestingly though, the blue-shifting effect only remained valid up to the ionic strength of $\sim$120 $mmol/kg_{ChNC}$. A further increase in the ionic strength, resulted in an opposite, red-shifting effect.

While such a way to tune helicoidal pitch must result from changes in liquid crystalline behaviour and the point of kinetic arrest, further work needs to be done to better understand it. Nevertheless, by simply adding HCl and/or NaCl it is possible to facilely tune the reflected light wavelengths from $\sim$550 to $\sim$950 nm.

Alternatively, adding a non-volatile component into the suspension proved to be an effective alternative strategy to red-shift the reflected colour (Figure 6.7). Poly-ethylene glycol (PEG, MW = 25 kDa) was used as it did not trigger any aggregation of ChNC and is unlikely to affect the self-assembly behaviour. It was determined that a gradual increase in reflected wavelength can be obtained with added PEG. This effect is rationalised as the reduction in compression of the ChNC chiral nematic phase upon drying as the non-volatile component remained when the ChNC suspension was dried, preventing ChNC concentration to reach 100%. A similar approach was previously exploited to tune the photonic CNC films. [200]

Reasons behind weak reflectance

Overall, a several various easy-to-implement strategies were successful to tune the reflected wavelength by fChNC films. However, films with helicoidal pitch small enough to appear blue were never achieved as well as the reflection consistently remained weak despite the number of conditions examined. To understand this, it is important to consider the polydomain nature of the sample. For that, a more sophisticated numerical calculation was used to simulate the reflectance spectra from fChNC films. [101]

As previously observed in POM, the films appeared to have different coloured regions (Figure 6.4). This observation suggests that the films are not completely homogeneous but composed of domains varying in its pitch and its thickness. In case of the polydomain sample, the average thickness of the different helicoidal domains needs to be considered as the unit interacting with light at a specific wavelength. This is because different domains having a different pitch, would reflect different wavelengths of light and the reflection would not add up to increase in intensity but rather the width of the apparent reflection peak. To address this point, a thorough SEM analysis was performed on the cross-sections of fChNC films. To obtain a statistically viable measurement, three identical fChNC films were cast. From each, a cross-section was obtained by pulling the film laterally until it fractured to obtain a cross-section which was all in the same plane. With numerous unsatisfactory cross-sections, three of them were sufficiently good to image the film from the top to the bottom surface, at a high magnification, to identify the domain sizes as well as the average pitch. The domain thickness was determined to range from 690 nm to 14 μm, which when normalised by its pitch, ranges from 3 to 90 pitch repeats. Consequently, the average domain thickness was calculated to be 21 (σ = 22) pitch repeats with the average pitch of 379 (σ = 93) nm.

Besides the domain thickness, the intrinsic chitin birefringence heavily influences the interaction of light with the helicoidal structure. Without any birefringence, there would be no coloured reflection of light as the structure would just appear as a uniform slab through

which the light would simply propagate. Birefringence describes the planar refractive index difference experienced by light propagating through the material such as a fChNC film. There are two types of birefringence. Intrinsic birefringence arises in materials due to the anisotropy in the way that the molecules are arranged, as in the case of ChNCs, the linear chitin molecules are arranged in parallel along the length of ChNCs, which results in an α crystal structure. When the light propagates along or perpendicular to the length of the ChNC, it would experience a different electronic structure and, therefore, a different refractive index. While it is expected that chitin (and so ChNCs) should have intrinsic birefringence, it is complicated to predict or measure the magnitude of this value. Another type of birefringence, form birefringence, arises in composites where one element, for example a rod, is dispersed in a material of a different refractive indexes. In fact, it is possible to get structural colouration from of a helicoidal structure made of silica, even though silica does not have intrinsic birefringence. [201] This is achieved by making an inverse replicate of a helicoidal film where the surrounding matrix is composed of silica and the positions previously taken up by CNCs, are now occupied by air.

Nevertheless, as fChNC films are made of pure chitin with limited porosity, mainly the intrinsic birefringence should be considered in understanding this weak reflectance. Besides pitch, domain thickness, and birefringence, the last two parameters required for the simulation are the angle of incidence of the light and the refractive index of chitin. Given that the POM was performed using a low magnification lens, which had a small numerical aperture, the light conditions can be assumed to be suitable for specular reflection with illumination and collection angle $\sim$0 °. Lastly, the refractive index of chitin has been reported to be $\sim$1.54. [17]

Given that the domain thickness and birefringence are the key parameters determining the reflectance from the helicoidal structures, a series of simulations were performed to construct a contour map of reflectance as a function of these two parameters (Figure 6.8 A). It was constructed by obtaining spectra from which the light reflection from the peak was used as a value to be plotted on the graph. The simulated reflectance spectra were consistent with the way that the measurements were carried out, namely by employed crossed-linear polarisers. Such simulations allowed to better understand the reflectance as a function of the thickness of the helicoidal structure as well as the birefringence of the component that makes it up. The contour lines indicate the fraction of light, which is expected to be reflected, with 0.01 line representing maximum experimental reflectance values obtained from fChNC films. Only birefringence values for chitin ranging between 0.001 to 0.005 could result in realistic reflectance values given the average thickness of the helicoidal domains was measured to be 21 pitch repeats thick. While the exact value of chitin birefringence is not that well

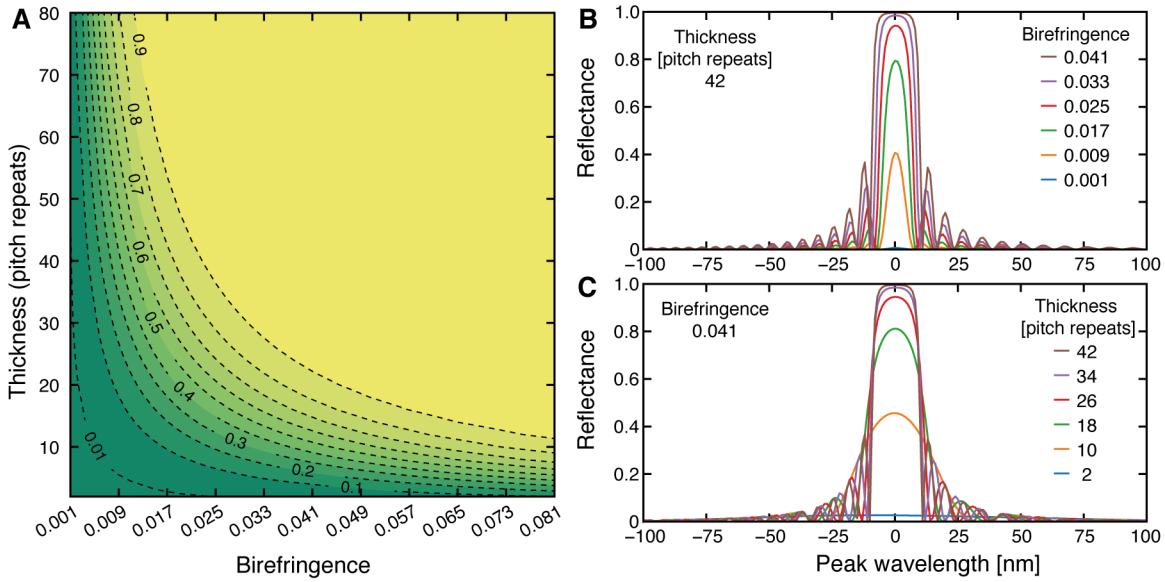

Figure 6.8 Optical simulations of reflectance spectra of helicoidal structures as a function of thickness and birefringence. **A** Optical simulations of reflectance spectra of helicoidal structures as a function of thickness and birefringence. Given the fixed pitch of 379 nm, average refractive index of 1.54, and angle of incidence of 0 °, a reflectance map was constructed using the maximum value of the reflectance peaks. The dashed lines indicate contours of equal reflectance corresponding to the written number. **B** Simulated spectra for a constant thickness but varied birefringence. It corresponds to reading the map in a horizontal direction. **C** The same as in B but birefringence was kept constant with the thickness being varied.

established in literature, similarly low values were reported for chitin previously. [17, 202] This clearly demonstrated that chitin, despite being similar to cellulose, cannot be simply treated as its analogue, given that cellulose birefringence is 0.081. [79, 87, 88]

The reflectance from these fChNC could be increased by making the helicoidal domains thicker. This requires a better alignment of the chiral nematic phase in liquid phase. For that purpose, it may be possible to use magnets to better align the chiral nematic phase as it was done with CNC. [42] It relies on the diamagnetic anisotropy of the material, and it was shown that ChNC can be aligned in extremely strong magnetic fields (9.4 T), the chiral nematic phase aligns so that the magnetic field is in parallel with the helical director, **m**. [33] This indicates that ChNC prefer to have their long dimension in a plane perpendicular to the magnetic field. Therefore, a Petri dish with suspension was placed with two magnets ($\sim$ 0.5 T) of opposite polarity below and above the dish. However, little improvement in the ordering was observed as the mixture of colours were observed, which was largely attributed to the fChNC180 suspension being too viscous (Figure 6.9). However, preliminary results

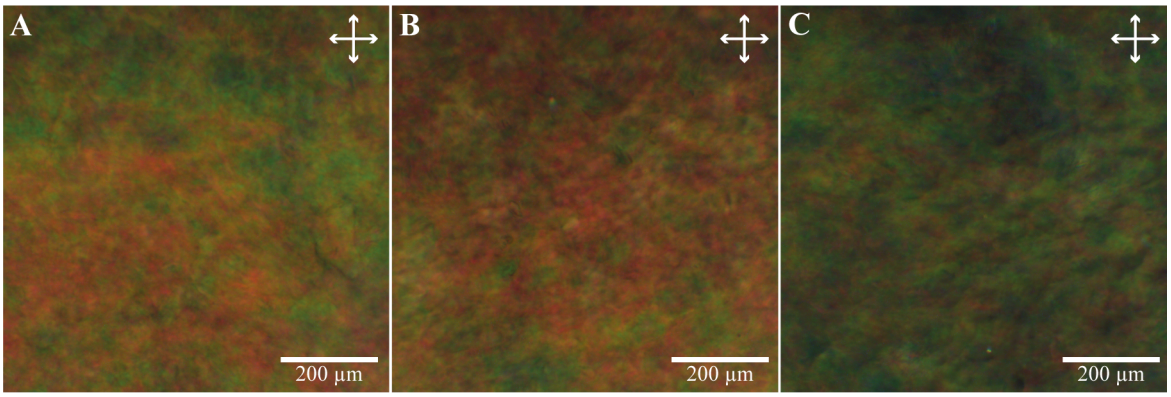

Figure 6.9 Polarised optical microscopy micrographs of fChNC films cast between two magnets. **A, B, C** Show that casting a film in the magnetic field did not result in a significant improvement in the helicoidal domain alignment as a mixture of colours was still observed.

using a patterned polymagnets with a shrimp derived ChNC suspension are promising in using magnets in obtaining patterned or aligned helicoidal films with simple and affordable magnets. Despite the lack of structural colouration due to the helicoidal pitch being too high in such a case, the pattern as the polymagnet one could be obtained if the suspension conditions (ionic strength and pH) were adequately adjusted (Figure 6.10). The influence of these weak magnets on sChNC liquid crystalline was justified given that these suspensions were overall much more fluid even when fully anisotropic in comparison to fChNC ones. The reorientation in the magnetic field requires that the anisotropic phase reorients, however, if the viscosity is too high this may be extremely slow and because of the concurrent evaporation, the suspension may reach the point of kinetic arrest before it can fully reorient. This is the likely explanation for the seemingly little effect on the fChNC suspensions.

However, even if the structures were obtained with helicoidal structures which would be 80 pitches repeat thick, the simulations indicate that with birefringence in the range 0.001-0.005, the reflectance would not reach high values (Figure 6.8 A). For instance, a helicoidal domain of 42 pitch repeats, can reflect more when the birefringence is even slightly increased (Figure 6.8 B). This can be done by increasing form or intrinsic birefringence. The former could come as a result of a high-volume fraction of additives of a significantly different refractive index from chitin which could be proteins or even uric acid as was found in structurally coloured beetles. [17] Addition of PEG, as previously described, did not show a significant increase in reflectance owing to the similarity of PEG and chitin refractive indexes. However, such additives can interfere with the colloidal stability and self-assembly prohibiting the formation of the helicoidal architecture at all. Alternatively, the intrinsic birefringence of chitin could be modified by means of altering its molecular and/or crystalline structure.

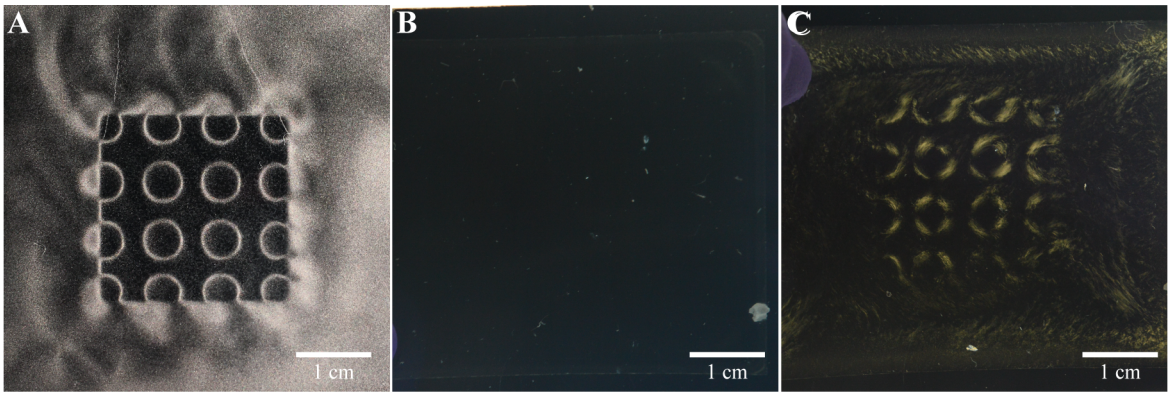

Figure 6.10 Shrimp derived ChNC films cast with patterned polymagnets magnets. **A** The pattern of the polymagnet that was observed using a field paper. **B** The film cast on a glass cover-slip, using 3M540 ChNC suspension extensively dialysed against Milli-Q water, did not appear to show any birefringence when viewed between crossed linear polarisers with back illumination, indicating that there was no alignment caused by the magnets. **C** The film cast on glass using the same suspension but with added HCl to make it runny, shows an analogous pattern to the polymagnet confirming that the ChNC liquid crystalline phase can be aligned and preserved in solid-state.

Deacetylation of fungal ChNC films

While modifications prior to the formation of the helicoidally structured solid-state films are likely to disturb colloidal and liquid-crystalline properties of ChNCs, the post-treatment on already helicoidally structured solid-state films could be a promising strategy.

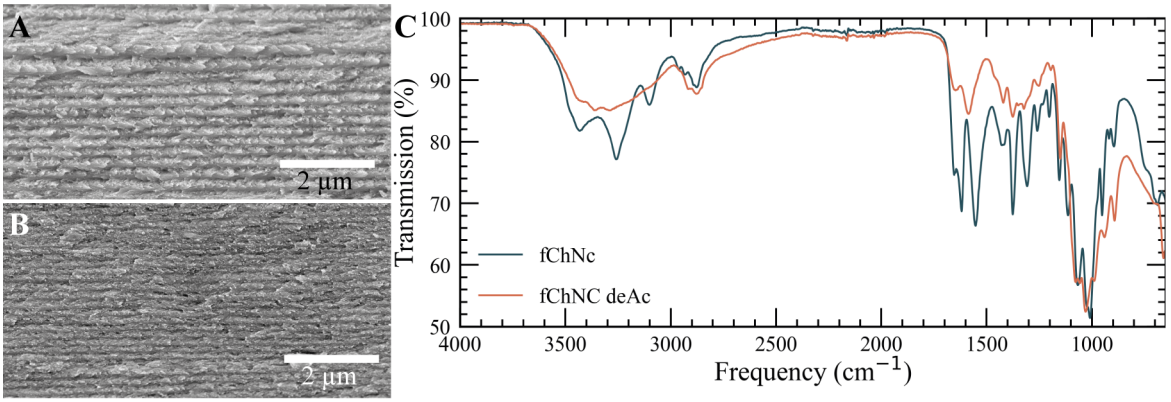

Figure 6.11 Cross-sectional SEM and FTIR of fungal ChNC before and after deacetylation. **A** fChNC before deacetylation showed that helicoidal structure was present throughout the whole film. **B** Cross-sectional SEM of deacetylated fChNC film showed the retention of helicoidal architecture with a decreased chiral nematic pitch. **C** FTIR spectra of fChNC before and after deacetylation, confirming the conversion to chitosan.

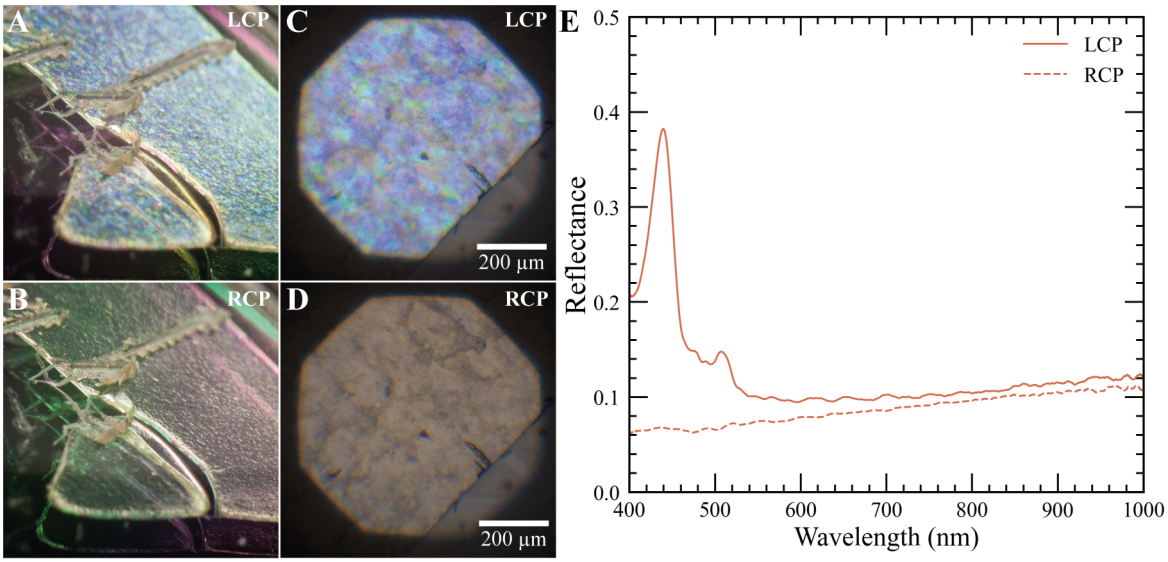

Figure 6.12 Increased reflectance after deacetylation of fChNC solid-state films. **A** Structural colouration can be observed by naked eye macroscopically in LCP channel. **B** Switching to RCP channel, structural colouration disappears, consistent with the expected optical behaviour of left-handed helicoidal structure. C, D This behaviour was confirmed by polarised optical microscopy **E** Corresponding spectra indicates a strong reflectance only in LCP channel.

In fact, chitin deacetylation to chitosan is one of the best known and established chitin modifications. [15, 19] The deacetylation reaction was, in fact, applied in the previous chapter to increase the surface charge of ChNC to study its influence on colloidal and liquid crystalline properties (Section 5.3.1). However, comparably mild conditions were chosen so that only the surface molecules would be partly converted from chitin to chitosan, its deacetylated derivative. However, to change the optical constants of the material, chitin needs to be completely converted to chitosan. While this could be applied to ChNCs prior to their self-assembly, the resulting material would simply dissolve in slightly acidic aqueous media to form a homogeneous solution of chitosan.

An alternative strategy to this, is to covert chitin into chitosan in already solid-state helicoidally nanostructured films. This was performed by taking a flake of this film and subjecting it to 50 % NaOH solution at 90 °C for 8 hours. At such conditions, the chitin crystal can swell and, therefore, deacetylation not only of the surface but the whole material can be obtained. The following steps of washing the material with Milli-Q and drying at ambient conditions avoids any acidic conditions, leaving the material intact, as otherwise chitosan would have dissolved. The success of the reaction was confirmed by FTIR where the spectra of chitin changed to the one consistent with chitosan (Figure 6.11 C).

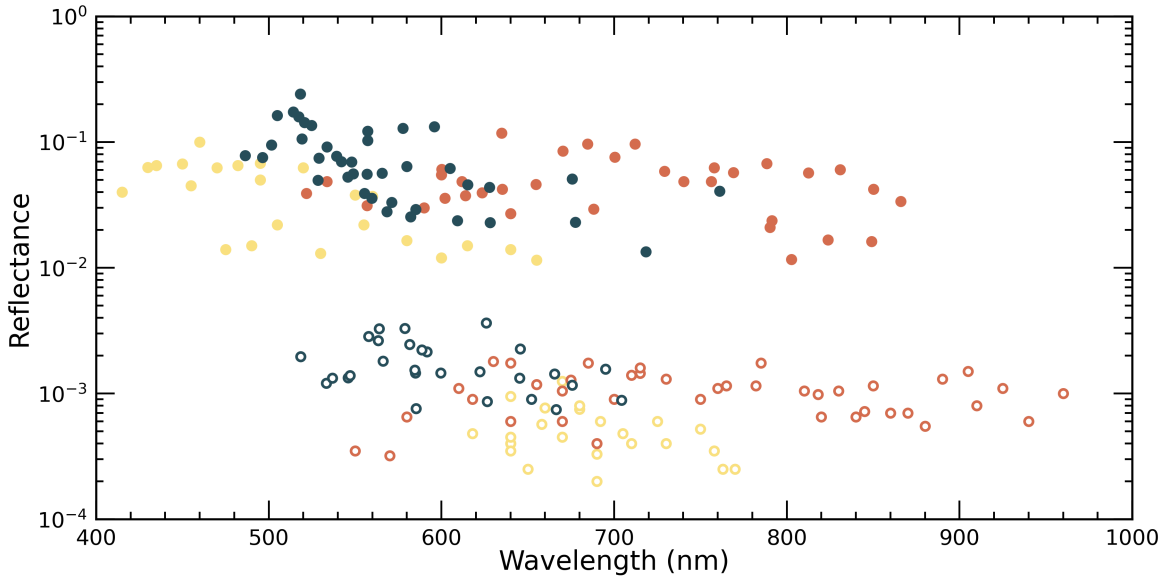

Figure 6.13 Comparison of optical properties of fungal ChNC films before and after deacetylation. **A** Distribution of the reflectance peaks before (open circle) and after deacetylation (full circle) for three different fChNC films with different starting reflecting colour. Measurements was acquired using crossed-linear polarisers.

Another important aspect was that this reaction is carried out heterogeneously by immersing a flake of fChNC in NaOH solution. The film retained its shape throughout the reaction with notable swelling given that initially solid film became akin to a gel. However, after the careful washing off of NaOH, the film was dried at ambient conditions. This allowed for the helicoidal structure in the initial film to be retained after its conversion to chitosan, which was evidenced by cross-sectional SEM analysis (Figure 6.11). However, this conversion led to a shrinkage of the helicoidal pitch from 379 (σ = 93) nm to 304 (σ = 80) nm (Figure 6.11 A, B). The shrinkage is likely to be caused by the loss of material which is expected to be around 20% by weight based on the difference of chitin and chitosan molecular formulas.

Nevertheless, because of this conversion the vivid structural colouration emerged (Figure 6.12 A). The colouration was evident was observed when looking through a left-circular polarisation (LCP) filter, while the colouration was extinguished when looking through a right-circular polarisation (RCP) filter (Figure 6.12). These results directly prove the structural colouration originating from the left-handed helicoidal architecture interacting only with LCP light at an appropriate wavelength. Such results were confirmed by POM observations which also showed that 30 % of LCP light can be reflected from such structures. Assuming that the helicoidal domains before and after deacetylation maintained the same number of pitch repeats (i.e., 21), the resulting intrinsic birefringence must have increased from 0.001 - 0.005 to 0.007 - 0.011 to explain the measured and simulated reflectance (Figure

6.8 A). The apparently small increase in birefringence, changed the material from barely to vividly coloured.

These changes were repeatedly observed by performing deacetylation on three different initial fChNC films (Figure 6.13). In all the cases, the average reflectance markedly improved and as well as the reflected colour blue shifted from the original (Figure 6.13). However, there are variations in the effectiveness that this treatment had, which could be related to the extent to which the deacetylation occurred as well as the inherent differences in the helicoidal domain average thickness when the casting conditions were changed. To get the better understanding of this treatment ideally an aligned film could be studied but for that a better understanding of how to apply magnets for producing structurally coloured films needs to be obtained.

Deacetylation of shrimp ChNC films

The observation that such a deacetylation treatment leads to a blue shift in reflected colour inspired to try it on shrimp ChNC films produced in Section 6.1. Out of the 5 samples, the one with the smallest pitch of $\sim$650 nm was tried as it was closest to be reflecting in the visible spectrum. A flake of this film was inserted in 50 wt% NaOH solution heated at 90 °C as before. After 8 hours of the reaction, the film appeared to be swelled much like in the case of treated fChNC films, however, not as fragile. After washing with Milli-Q and allowing it to dry at ambient conditions, the flake remained intact with observable colour (Figure 6.14 A). The SEM analysis of the cross-section confirmed that the helicoidal architecture was retained, however, it proved to be difficult to obtain a clean fracture required for good imaging (Figure 6.14 B). Polarised optical microscopy was used to establish a reflection of up to 30% only of left-circularly polarised light, corroborating the evidence of the left-handed helicoidal structure remaining intact (Figure 6.14 C, D, E). The reflection spectra show a number of peaks originating from domains with helical structure but different pitch, with at least half of the reflection still happening at near-IR wavelengths, thus invisible to the human eye. Yet, it remains to be seen if uniform strong reflection at different wavelengths of visible light can be obtained by relying on such deacetylation of films of shrimp ChNC which are more available and easier to modify using magnets for a better alignment.

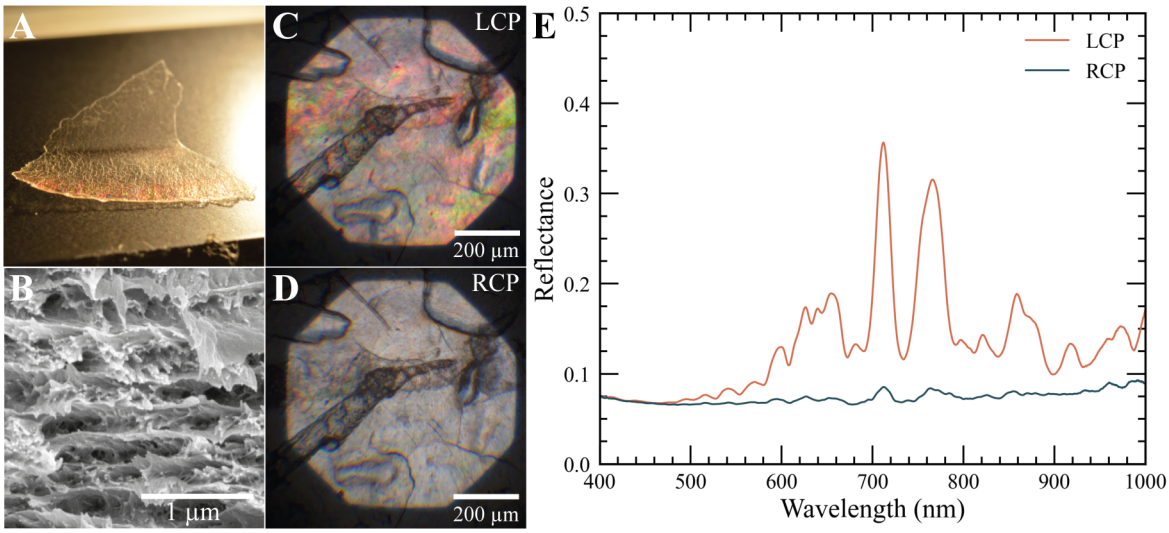

Figure 6.14 Structural colouration in shrimp derived ChNC films after deacetylation. **A** A photograph of a film produced from a shrimp ChNC after deacetylation. **B** Cross-section was analysed by SEM indicating that the layer structure is preserved after the treatment. **C, D** Polarised optical microscopy micrographs captured in reflection in left-circular polarisation (LCP) and right-circular polarisation (RCP) channels, respectively. **E** Corresponding reflection spectra, indicating a strong reflection in the LCP channel only.

Chapter 7

Conclusions

As one of the most abundant biopolymers on the planet, chitin is far from being well explored and utilised. Interestingly, this polysaccharide can be converted into colloidally stable nanoparticles able to self-assemble into a chiral nematic liquid crystalline phase which indicates a path to produce materials with structures and function akin to those employed by tough crabs and colourful beetles. However, to achieve such a goal, many questions regarding the self-assembly and colloidal properties of chitin nanocrystals (ChNCs) were investigated first.

Acidic hydrolysis was the starting point in preparing ChNCs. The hydrolysis conditions had a huge impact on colloidal and liquid crystalline properties. Hydrolysis at 5.0 M HCl at reflux posed a risk of over-hydrolysis of the material which was observed when running the reaction for 270 minutes, however, stopping it at 180 minutes resulted in the overall smallest ChNCs. In contrast, the largest nanoparticles compromising colloidal stability and the self-assembly were obtained by a commonly employed hydrolysis at 3.0 M HCl at reflux for 90 minutes. Longer hydrolysis for 270 and 540 minutes, resulted in suspensions which not only were colloidally stable but also easily self-assembled into a chiral nematic phase. Therefore, these conditions are recommended for further use.

In parallel to the hydrolysis, the suspension treatment played an important role. As an example, *tip sonication* was fundamental to properly disperse ChNCs in suspension. With tip sonication input, smaller and more dispersed nanoparticles were obtained without altering the aspect ratio which is important for the formation of the chiral nematic phase. However, tip sonication affected liquid-crystalline behaviour by, possibly, decreasing the presence of strongly chiral ChNC bundles inherently present in the suspension. The effectiveness of tip sonication was mostly observed initially with it levelling off. While the amount of tip sonication must be tailored to a given suspension, for the one prepared with 3.0M HCl at

reflux for 540 min, the tip sonication performed for 4.5 min or more on 200 g of 1.0 wt% suspension is recommended.

Chitin deacetylation prior to hydrolysis resulted in thinner ChNC with the length being affected less. It resulted from the deacetylated chitin crystal surface being converted to chitosan and getting etched during acidic hydrolysis. While the amount of etched deacetylated surface may depend on hydrolysis conditions, following 3M540 resulted in more slender nanocrystals of a higher aspect ratio but with comparable surface charge to ChNCs prepared from untreated chitin.

ChNC deacetylation post hydrolysis instead allowed to tune ChNC surface charge without compromising their colloidal stability. The surface charge increased with the duration of deacetylation, resulting in self-assembly at ever higher ChNC concentrations. This may cause problems for self-assembly into chiral nematic phase as the kinetic arrest may occur before the suspension is fully anisotropic. The surface charge of the ordinarily prepared ChNC was already close to the optimal one for the ChNC self-assembly as higher surface charges imparted problems with suspension gelling before a complete formation of chiral nematic phase.

Changing chitin source to *fungal chitin* resulted in ChNCs with significantly different behaviour and required to reinvestigation of hydrolysis conditions as hydrolysis for 3.0 M at reflux for 540 minutes resulted in over-hydrolysis. It was found that 90 and 180 minutes were sufficient conditions in preparing well dispersed ChNCs with colloidal and liquid crystalline properties significantly different from shrimp derived ChNC. Essentially, phase separation occurred at low ChNC concentrations with small chiral nematic pitches.

These results summarise the limits of the physical ChNC properties and how they affect the colloidal and liquid crystalline properties and paved the path in investigating the production of solid-state materials.

Shrimp ChNC solid-state materials were produced by simple evaporation in a Petri dish. The optimised ChNC preparation conditions allowed for the chiral nematic-like ordering to be preserved even in the dry phase. It resulted because of a complete formation of chiral nematic phase was followed by the kinetic arrest. These two processes were found to be strongly influenced by the ChNC double-layer, tunable with pH and ionic strength. As a consequence solid-state films with helicoidal pitch ranging from $\sim$650 to $\sim$5,000 nm were made. These high pitch values, hardly attainable with CNCs, may show promise in the use of this material for advanced materials with novel mechanical properties which can be observed in crustaceans and insects. [4] However, in nature many beetles use helicoidal structures made of chitin to obtain structural colouration. [17] Alas, shrimp ChNC films had the helicoidal pitch too high for reflection of visible light. In contrast, fungal ChNC solid-state

materials with structural colouration were prepared by relying on fungal ChNC unique liquid crystalline behaviour. The reflected colour was shown to be tunable by controlled addition of HCl, NaCl, and PEG. This marks the first instance for structurally coloured chitin material to be artificially made. Nevertheless, the reflected colour was not particularly intense which was expected based on seeing iridescent beetles and cellulose analogous.

Simulations of the interaction of light with such helicoidal structures were key to unravelling this peculiar behaviour. It was found that intrinsic birefringence of chitin $\sim$0.001-0.005 was too small to effectively reflect visible light if used in helicoidal structures. This limitation was effectively overcome by increasing intrinsic birefringence. Increased reflectance was obtained by completely converting dry structurally coloured ChNC films from chitin to chitosan since the helicoidal architecture was retained. Such deacetylated films showed structural colouration evident even to the naked eye, which indicating an increase in intrinsic birefringence. Concurrently, a blue-shift in the reflected colour provided additional means of tuning the reflected colour.

While this thesis showcases the potential that ChNCs have by covering a breadth of parameters by which their colloidal and liquid crystalline properties can be manipulated, it is only a basis onto which further research should be developed to exploit this material in a broader context. Overall, this thesis has explored several parameters which can affect the colloidal and liquid-crystalline properties of ChNCs which finally allow to manufacture and tune solid-state materials with helicoidal architecture made of chitin. The numerous nuances encountered in dealing with this system, exemplified by its unique surface chemistry, sensitivity to pH, as well as the extremely low birefringence, indicate that ChNC should not be looked like just CNC analogous. The system is interesting as structural colouration can be obtained and modified by post-treatment with base which is also not available for cellulose. On top of that, solid-state films with helicoidal pitches as large as 5 µm point at their potential usefulness in the future materials with resistance to crack propagation. The additional features of structuring for such solid-state structures may be possible by means of using magnets which can add another level of complexity which is observed in mantis shrimp. [199] Thus, this thesis enables the research to be continued to produce functional materials from an abundant, affordable, and, importantly, sustainable resource, named, chitin.

Chapter 8

Future work

While this work provides a strong foundation for further research into chitin nanocrystals (ChNCs), more work needs to be done to improve and consolidate the field. There are many interesting areas where ChNCs could be directed.

First, it is important to assess the influence that drying of the purified chitin starting material has on the resulting ChNCs. It was shown using cellulose that drying or pre-treating it can affect the resulting CNC properties. [203, 204] While this work used never dried material, it is inconvenient for long term storage and setting up hydrolysis. In addition, while this work provides a good foundation for the ChNC research, a more systematic approach could be employed to be able to confidently choose the appropriate reactions conditions (i.e., acidity, reaction temperature, and duration) to produce ChNCs of desired size, shape, surface charge. Better material characterisation standards are being developed for CNCs and so they should be adapted for ChNCs to improve reproducibility. [140, 141]

Thereafter, there are numerous organisms that contain chitin. [15] In this work, it was shown that choosing between shrimp or fungal chitin, the resulting ChNC properties can be heavily affected. Similar observations were established with CNCs. [31] A systematic comparison of the ChNCs from various sources (e.g., different crustaceans, insects, and fungi) would establish the range of ChNC that can be produced. Besides, while most of the chitin in nature is of α allomorph, β-chitin is found in Riftia tubes or squid pens. [15] When β-chitin is converted to its nanoform, it has an outstanding aspect ratio, which would be interesting to study for their self-assembly ability. [205] Besides, chitin chains are in parallel in β, whereas anti-parallel in α-chitin, it would be interesting to study if the material dipole arising from different chain orientation is important in inducing chiral interactions in liquid crystalline state.

The exploration of different chitin sources is also relevant from the sustainability perspective as insect farming is a promising future industry, which could provide chitin for its

conversion to ChNCs and other value added products (see section 3.1). The interest to use of insect chitin to produce ChNCs is only now starting to emerge. [118] The possibly interesting physicochemical properties of insect ChNCs are thus combined with more sustainable ChNC research. In addition, ChNCs could become truly environmentally friendly if instead of large quantities of mineral acids, new technologies using deep eutectic solvents are better studied and implemented in making ChNCs. [151, 152]

Hydrogels of ChNCs with chiral nematic architecture could be explored for a variety of interesting studies. One example is to is for *in-situ* biomineralization of $CaCO_3$ to mimic material such as crustacean shell. [161, 206] This strategy could be expanded for producing other composite materials with anisotropic mechanical properties or the use of the template for confined synthesis for metal nanoparticles.

In nature chitin is strongly associated with proteins, which are believed to play a crucial role in controlling the assembly of chitin in the arthropod cuticle. [207] The current hypothesis regarding the helicoidal architecture in the arthropod cuticle and control of the twisting power involves the transient liquid crystalline state, which is modified by a variety of proteins which have a specific chitin binding motif. [6, 107, 108, 207] Such proteins are found in the arthropod cuticle and while their overall structure may significantly vary, the specific chitin binding motif is strongly conserved throughout the whole Arthropod phylum. As such, studying ChNCs, their self-assembly and, possibly, co-assembling them with such proteins, may give clues on how the natural assembly process occurs and such strategies to be used to produce high-end products.

References

[1] J. Aizenberg and P. Fratzl, "New materials through bioinspiration and nanoscience," *Adv. Funct. Mater.*, vol. 23, pp. 4398–4399, 2013.

[2] U. G. K. Wegst, H. Bai, E. Saiz, A. P. Tomsia, and R. O. Ritchie, "Bioinspired structural materials," *Nat. Mater*, vol. 14, no. 1, pp. 23–36, 2015.

[3] M. Eder, S. Amini, and P. Fratzl, "Biological composites—complex structures for functional diversity," *Science*, vol. 362, no. 6414, pp. 543–547, 2018.

[4] Y. Bouligand, "Sur une architecture torsadée répandue dans de nombreuses cuticules d'Arthopodes," *C. R. Acad. Sci.*, vol. 261, pp. 3665–3666, 1965.

[5] B. D. Wilts, H. M. Whitney, B. J. Glover, U. Steiner, and S. Vignolini, "Natural helicoidal structures: Morphology, self-assembly and optical properties," *Mater. Today Proc.*, vol. 1, pp. 177–185, 2014.

[6] M. Mitov, "Cholesteric liquid crystals in living matter," *Soft Matter*, vol. 13, no. 23, pp. 4176–4209, 2017.

[7] R. M. Parker, G. Guidetti, C. A. Williams, T. Zhao, A. Narkevicius, S. Vignolini, and B. Frka-Petešić, "The Self-Assembly of Cellulose Nanocrystals: Hierarchical Design of Visual Appearance," *Adv. Mater.*, vol. 30, no. 19, p. 1704477, 2018.

[8] R. H. Marchessault, F. F. Morehead, and N. M. Walter, "Liquid crystal systems from fibrillar polysaccharides," *Nature*, vol. 184, no. 4686, pp. 632–633, 1959.

[9] J. Revol, H. Bradford, J. Giasson, R. H. Marchessault, and D. G. Gray, "Helicoidal self-ordering of cellulose microfibrils in aqueous suspension," *Int. J. Biol. Macromol.*, vol. 14, no. 3, pp. 170–172, 1992.

[10] J. Revol and R. H. Marchessault, "In vitro chiral nematic ordering of chitin crystallites," *Int. J. Biol. Macromol*, vol. 15, no. 6, pp. 329–335, 1993.

[11] R. S. Werbowyj and D. G. Gray, "Liquid Crystalline Structure in Aqueous Hydroxypropyl Cellulose Solutions.," *Mol Cryst Liq Cryst*, vol. 34, no. 4, pp. 97–103, 1976.

[12] R. S. Werbowyj and D. G. Gray, "Optical Properties of (Hydroxypropyl)cellulose Liquid Crystals. Choleseric Pitch and Polymer Concentration," *Macromolecules*, vol. 17, no. 8, pp. 1512–1520, 1984.

[13] A. G. Dumanli, H. M. van der Kooij, G. Kamita, E. Reisner, J. J. Baumberg, U. Steiner, and S. Vignolini, "Digital color in cellulose nanocrystal films," *ACS Appl. Mater. Interfaces*, vol. 6, no. 15, pp. 12302–12306, 2014.

[14] N. Lin, J. Huang, and A. Dufresne, "Preparation, properties and applications of polysaccharide nanocrystals in advanced functional nanomaterials: A review," *Nanoscale*, vol. 4, no. 11, pp. 3274–3294, 2012.

[15] M. Rinaudo, "Chitin and chitosan: Properties and applications," *Prog. Polym. Sci*, vol. 31, no. 7, pp. 603–632, 2006.

[16] A. C. Neville, *Biology of the arthropod cuticle*, vol. 4. Springer Science & Business Media, 2012.

[17] S. Caveney, "Cuticle Reflectivity and Optical Activity in Scarab Beetles: The Role of Uric Acid," *Proc. R. Soc. B Biol. Sci.*, vol. 178, no. 1051, pp. 205–225, 1971.

[18] L. K. Grunenfelder, S. Herrera, and D. Kisailus, "Crustacean-derived biomimetic components and nanostructured composites," *Small*, vol. 10, no. 16, pp. 3207–3232, 2014.

[19] M. Mincea, A. Negrulescu, and V. Ostafe, "Preparation, modification, and applications of chitin nanowhiskers: a review," *Rev. Adv. Mater. Sci*, vol. 30, no. 3, pp. 225–242, 2012.

[20] G. A. F. Roberts, "Thirty years of progress in chitin and chitosan," *Progress on chemistry and application of chitin and its derivatives*, vol. 13, pp. 7–15, 2008.

[21] J.-B. Zeng, Y.-S. He, S.-L. Li, and Y.-Z. Wang, "Chitin whiskers: An overview," *Biomacromolecules*, vol. 13, no. 1, pp. 1–11, 2012.

[22] F. Gaill, J. Persson, J. Sugiyama, R. Vuong, and H. Chanzy, "The chitin system in the tubes of deep sea hydrothermal vent worms," *J. Struct. Biol.*, vol. 109, no. 2, pp. 116–128, 1992.

[23] J. D. Goodrich and W. T. Winter, "α-Chitin nanocrystals prepared from shrimp shells and their specific surface area measurement," *Biomacromolecules*, vol. 8, no. 1, pp. 252–257, 2007.

[24] J. Li, J. Revol, and R. H. H. Marchessault, "Effect of degree of deacetylation of chitin on the properties of chitin crystallites," *J. Appl. Polym. Sci.*, vol. 65, no. 2, pp. 373–380, 1997.

[25] A. G. B. Pereira, E. C. Muniz, and Y.-L. Hsieh, "Chitosan-sheath and chitin-core nanowhiskers," *Carbohydrate polymers*, vol. 107, pp. 158–166, 2014.

[26] N. Yaghobi and F. Hormozi, "Multistage deacetylation of chitin: Kinetics study," *Carbohydrate Polymers*, vol. 81, no. 4, pp. 892–896, 2010.

[27] M. N. V. R. Kumar, R. A. A. Muzzarelli, C. Muzzarelli, H. Sashiwa, and A. J. Domb, "Chitosan chemistry and pharmaceutical perspectives," *Chemical reviews*, vol. 104, no. 12, pp. 6017–6084, 2004.

[28] S. M. Mukherjee and H. J. Woods, "X-ray and electron microscope studies of the degradation of cellulose by sulphuric acid," *Biochim. Biophys. Acta*, vol. 10, pp. 499–511, 1953.

[29] B. G. Ranby, A. Banderet, and L. G. Sillen, "Aqueous colloidal solutions of cellulose micelles," 1949.

[30] D. H. Everett, *Basic Principles of Colloid Science*. Royal Society of Chemistry, 1988.

[31] S. Elazzouzi-Hafraoui, Y. Nishiyama, J.-L. Putaux, L. Heux, F. Dubreuil, and C. Rochas, "The shape and size distribution of crystalline nanoparticles prepared by acid hydrolysis of native cellulose.," *Biomacromolecules*, vol. 9, no. 1, pp. 57–65, 2008.

[32] S. Beck-Candanedo, M. Roman, and D. G. Gray, "Effect of reaction conditions on the properties and behavior of wood cellulose nanocrystal suspensions," *Biomacromolecules*, vol. 6, no. 2, pp. 1048–1054, 2005.

[33] E. Belamie, P. Davidson, and M. M. Giraud-Guille, "Structure and chirality of the nematic phase in α-chitin suspensions," *J. Phys. Chem. B*, vol. 108, no. 39, pp. 14991–15000, 2004.

[34] R. M. Parker, B. Frka-Petešić, G. Guidetti, G. Kamita, G. Consani, C. Abell, and S. Vignolini, "Hierarchical Self-Assembly of Cellulose Nanocrystals in a Confined Geometry," *ACS Nano*, vol. 10, no. 9, pp. 8443–8449, 2016.

[35] D. Bonn, H. Tanaka, G. Wegdam, H. Kellay, and J. Meunier, "Aging of a colloidal "Wigner" glass," *Europhys. Lett.*, vol. 45, no. 1, pp. 52–57, 1999.

[36] E. Zaccarelli, "Colloidal gels: Equilibrium and non-equilibrium routes," *J. Phys. Condens. Matter*, vol. 19, no. 32, p. 323101, 2007.

[37] M. Nordenström, A. Fall, G. Nyström, and L. Wågberg, "Formation of Colloidal Nanocellulose Glasses and Gels," *Langmuir*, vol. 33, no. 38, pp. 9772–9780, 2017.

[38] S. Shafiei-Sabet, W. Y. Hamad, and S. G. Hatzikiriakos, "Ionic strength effects on the microstructure and shear rheology of cellulose nanocrystal suspensions," *Cellulose*, vol. 21, no. 5, pp. 3347–3359, 2014.

[39] M. S. Reid, S. A. Kedzior, M. Villalobos, and E. D. Cranston, "Effect of Ionic Strength and Surface Charge Density on the Kinetics of Cellulose Nanocrystal Thin Film Swelling," *Langmuir*, vol. 33, no. 30, pp. 7403–7411, 2017.

[40] C. Honorato-Rios, C. Lehr, C. Schütz, R. Sanctuary, M. A. Osipov, J. Baller, and J. P. F. Lagerwall, "Fractionation of cellulose nanocrystals: enhancing liquid crystal ordering without promoting gelation," *NPG Asia Mater.*, vol. 10, no. 5, pp. 455–465, 2018.

[41] L. Heux, G. Chauve, and C. Bonini, "Nonflocculating and chiral-nematic self-ordering of cellulose microcrystals suspensions in nonpolar solvents," *Langmuir*, vol. 16, no. 21, pp. 8210–8212, 2000.

[42] B. Frka-Petešić, G. Guidetti, G. Kamita, and S. Vignolini, "Controlling the Photonic Properties of Cholesteric Cellulose Nanocrystal Films with Magnets," *Adv. Mater.*, vol. 29, no. 32, pp. 1–7, 2017.

[43] S. Ifuku, T. Hori, H. Izawa, M. Morimoto, and H. Saimoto, "Preparation of zwitterionically charged nanocrystals by surface TEMPO-mediated oxidation and partial deacetylation of α-chitin," *Carbohydr. Polym.*, vol. 122, pp. 1–4, 2015.

[44] Y. Fan, T. Saito, and A. Isogai, "Individual chitin nano-whiskers prepared from partially deacetylated α-chitin by fibril surface cationization," *Carbohydr. Polym.*, vol. 79, no. 4, pp. 1046–1051, 2010.

[45] S. Beck and J. Bouchard, "Auto-catalyzed acidic desulfation of cellulose nanocrystals," *Nord. Pulp Pap. Res. J.*, vol. 29, no. 1, pp. 6–14, 2014.

[46] C. Schütz, J. R. Bruckner, C. Honorato-Rios, Z. Tosheva, M. Anyfantakis, and J. P. F. Lagerwall, "From equilibrium liquid crystal formation and kinetic arrest to photonic bandgap films using suspensions of cellulose nanocrystals," *Crystals*, vol. 10, no. 3, p. 199, 2020.

[47] A. G. Dumanli, G. Kamita, J. Landman, H. van der Kooij, B. J. Glover, J. J. Baumberg, U. Steiner, and S. Vignolini, "Controlled, bio-inspired self-assembly of cellulose-based chiral reflectors," *Adv. Opt. Mater.*, vol. 2, no. 7, pp. 646–650, 2014.

[48] J. H. Park, J. H. Noh, C. Schütz, G. Salazar-Alvarez, G. Scalia, L. Bergström, and J. Lagerwall, "Macroscopic control of helix orientation in films dried from cholesteric liquid-crystalline cellulose nanocrystal suspensions," *ChemPhysChem*, vol. 15, no. 7, pp. 1477–1484, 2014.

[49] M. D. Xue, T. Kimura, J. Revol, and D. G. Gray, "Effects of ionic strength on the isotropic-chiral nematic phase transition of suspensions of cellulose crystallites," *Langmuir*, vol. 12, no. 8, pp. 2076–2082, 1996.

[50] P. X. Wang, W. Y. Hamad, and M. J. MacLachlan, "Polymer and Mesoporous Silica Microspheres with Chiral Nematic Order from Cellulose Nanocrystals," *Angewandte Chemie*, vol. 55, no. 40, pp. 12460–12464, 2016.

[51] C. Schütz, M. Agthe, A. B. Fall, K. Gordeyeva, V. Guccini, M. Salajková, T. S. Plivelic, J. P. F. Lagerwall, G. Salazar-Alvarez, and L. Bergström, "Rod Packing in Chiral Nematic Cellulose Nanocrystal Dispersions Studied by Small-Angle X-ray Scattering and Laser Diffraction," *Langmuir*, vol. 31, no. 23, pp. 6507–6513, 2015.

[52] L. Onsager, "The Effects of Shape on the Interaction of Colloidal Particles," *Ann. N. Y. Acad. Sci.*, vol. 51, no. 4, pp. 627–659, 1949.

[53] D. Frenkel, "Order through entropy," *Nat. Mater.*, vol. 14, no. 1, pp. 9–12, 2015.

[54] G. J. Vroege and H. N. W. Lekkerkerker, "Phase transitions in lyotropic liquid crystals: bilayer and micelle stability," *Reports Prog. Phys.*, vol. 55, no. July 1991, pp. 1241–1309, 1992.

[55] J. V. Selinger, *Introduction to the theory of soft matter: from ideal gases to liquid crystals*. Springer, 2015.

[56] A. Stroobants, H. N. W. Lekkerkerker, and T. Odijk, "Effect of Electrostatic Interaction on the Liquid Crystal Phase Transition in Solutions of Rodlike Polyelectrolytes," *Macromolecules*, vol. 19, no. 8, pp. 2232–2238, 1986.

[57] H. H. Wensink and G. J. Vroege, "Isotropic-nematic phase behavior of length-polydisperse hard rods," *J. Chem. Phys.*, vol. 119, no. 13, pp. 6868–6882, 2003.

[58] T. Odijk, "Theory of Lyotropic Polymer Liquid Crystals," *Macromolecules*, vol. 19, no. 9, pp. 2313–2329, 1986.

[59] S. D. Lee, "A numerical investigation of nematic ordering based on a simple hard-rod model," *J. Chem. Phys.*, vol. 87, no. 8, pp. 4972–4974, 1987.

[60] X. Xiao and P. Sheng, "Generalized onsager theory of liquid crystals," *Physical Review E*, vol. 88, no. 6, p. 062501, 2013.

[61] J. Li, J. Revol, E. Naranjo, and R. H. Marchessault, "Effect of electrostatic interaction on phase separation behaviour of chitin crystallite suspensions," *Int. J. Biol. Macromol.*, vol. 18, no. 3, pp. 177–187, 1996.

[62] C. Honorato-Rios, A. Kuhnhold, J. R. Bruckner, R. Dannert, T. Schilling, and J. P. F. Lagerwall, "Equilibrium liquid crystal phase diagrams and detection of kinetic arrest in cellulose nanocrystal suspensions," *Front. Mater.*, vol. 3, no. May, pp. 1–13, 2016.

[63] T. Abitbol, D. Kam, Y. Levi-Kalisman, D. G. Gray, and O. Shoseyov, "Surface Charge Influence on the Phase Separation and Viscosity of Cellulose Nanocrystals," *Langmuir*, vol. 34, no. 13, pp. 3925–3933, 2018.

[64] W. Bai, J. Holbery, and K. Li, "A technique for production of nanocrystalline cellulose with a narrow size distribution," *Cellulose*, vol. 16, no. 3, pp. 455–465, 2009.

[65] J. F. Revol, D. L. Godbout, and D. G. Gray, "Solidified liquid crystals of cellulose with optically variable properties," *US Pat. 5,629,055*, vol. 28, no. 14, p. 9, 1997.

[66] J. Araki and S. Kuga, "Effect of trace electrolyte on liquid crystal type of cellulose microcrystals," *Langmuir*, vol. 17, no. 15, pp. 4493–4496, 2001.

[67] R. S. Werbowyj and D. G. Gray, "Ordered phase formation in concentrated hydroxpropylcellulose solutions," *Macromolecules*, vol. 13, no. 1, pp. 69–73, 1980.

[68] W. J. Orts, L. Godbout, R. H. Marchessault, and J. Revol, "Enhanced ordering of liquid crystalline suspensions of cellulose microfibrils: A small angle neutron scattering study," *Macromolecules*, vol. 31, no. 17, pp. 5717–5725, 1998.

[69] G. Nyström, M. Arcari, J. Adamcik, I. Usov, and R. Mezzenga, "Nanocellulose Fragmentation Mechanisms and Inversion of Chirality from the Single Particle to the Cholesteric Phase," *ACS Nano*, vol. 12, no. 6, pp. 5141–5148, 2018.

[70] I. Usov, G. Nyström, J. Adamcik, S. Handschin, C. Schütz, A. Fall, L. Bergström, and R. Mezzenga, "Understanding nanocellulose chirality and structure-properties relationship at the single fibril level," *Nat. Commun*, vol. 6, no. 1, 2015.

[71] K. Conley, L. Godbout, M. A. Whitehead, and T. G. M. van De Ven, "Origin of the twist of cellulosic materials," *Carbohydr. Polym.*, vol. 135, pp. 285–299, 2016.

[72] M. Khandelwal and A. Windle, "Origin of chiral interactions in cellulose supramolecular microfibrils," *Carbohydr. Polym.*, vol. 106, no. 1, pp. 128–131, 2014.

[73] X. M. Dong and D. G. Gray, "Effect of Counterions on Ordered Phase Formation in Suspensions of Charged Rodlike Cellulose Crystallites," *Langmuir*, vol. 13, no. 8, pp. 2404–2409, 1997.

[74] J. Pan, W. Y. Hamad, and S. K. Straus, "Parameters affecting the chiral nematic phase of nanocrystalline cellulose films," *Macromolecules*, vol. 43, no. 8, pp. 3851–3858, 2010.

[75] S. Beck, J. Bouchard, and R. Berry, "Controlling the reflection wavelength of iridescent solid films of nanocrystalline cellulose," *Biomacromolecules*, vol. 12, no. 1, pp. 167–172, 2011.

[76] B. Frka-Petešić, G. Kamita, G. Guidetti, and S. Vignolini, "Angular optical response of cellulose nanocrystal films explained by the distortion of the arrested suspension upon drying," *Phys. Rev. Mater.*, vol. 3, no. 4, p. 045601, 2019.

[77] S. Vignolini, T. Gregory, M. Kolle, A. Lethbridge, E. Moyroud, U. Steiner, B. J. Glover, P. Vukusic, and P. J. Rudall, "Structural colour from helicoidal cell-wall architecture in fruits of margaritaria nobilis," *J R Soc Interface*, vol. 13, no. 124, p. 20160645, 2016.

[78] S. Vignolini, P. J. Rudall, A. V. Rowland, A. Reed, E. Moyroud, R. B. Faden, J. J. Baumberg, B. J. Glover, and U. Steiner, "Pointillist structural color in pollia fruit," *PNAS*, vol. 109, no. 39, pp. 15712–15715, 2012.

[79] B. Frka-Petešić, J. Sugiyama, S. Kimura, H. Chanzy, and G. Maret, "Negative Diamagnetic Anisotropy and Birefringence of Cellulose Nanocrystals," *Macromolecules*, vol. 48, no. 24, pp. 8844–8857, 2015.

[80] J. Brodie, C. J. Ingham, and S. Vignolini, "Does structural color exist in true fungi?," *J. Fungi*, vol. 7, no. 2, pp. 1–5, 2021.

[81] S. M. Doucet and M. G. Meadows, "Iridescence: A functional perspective," *J. R. Soc. Interface*, vol. 6, no. SUPPL. 2, 2009.

[82] S. L. Burg and A. J. Parnell, "Self-assembling structural colour in nature," *J. Phys. Condens. Matter*, vol. 30, no. 41, 2018.

[83] T. H. Zhao, R. M. Parker, C. A. Williams, K. T. Lim, B. Frka-Petesic, and S. Vignolini, "Printing of Responsive Photonic Cellulose Nanocrystal Microfilm Arrays," *Adv. Funct. Mater.*, vol. 29, no. 21, 2019.

[84] E. Hecht, *Optics*. Pearson Education, 2017.

[85] F. Träger, *Springer handbook of lasers and optics*. Springer Science & Business Media, 2012.

[86] E. S. Castle, "The double refraction of chitin," *J. Gen. Physiol.*, vol. 19, no. 5, pp. 797–805, 1936.

[87] P. H. Hermans, "Contribution to the physics of cellulose fibres," *Nature*, vol. 159, no. 4042, pp. 519–520, 1946.

[88] K. R. K. Iyer, P. Neelakantan, and T. Radhakrishnan, "Birefringence of native cellulosic fibers. i. untreated cotton and ramie," *J. Polym. Sci., Part B: Polym. Phys.*, vol. 6, no. 10, pp. 1747–1758, 1968.

[89] M. S. Reid, M. Villalobos, and E. D. Cranston, "Cellulose nanocrystal interactions probed by thin film swelling to predict dispersibility," *Nanoscale*, vol. 8, no. 24, pp. 12247–12257, 2016.

[90] E. D. Cranston and D. G. Gray, "Birefringence in spin-coated films containing cellulose nanocrystals," *Colloids Surfaces A Physicochem. Eng. Asp.*, vol. 325, no. 1-2, pp. 44–51, 2008.

[91] A. Leforestier and F. Livolant, "Supramolecular ordering of DNA in the cholesteric liquid crystalline phase: an ultrastructural study," *Biophys. J.*, vol. 65, no. 1, pp. 56–72, 1993.

[92] J. L. Fergason, "Cholesteric Structure-1 Optical Properties," *Mol. Cryst.*, vol. 1, no. 2, pp. 293–307, 1966.

[93] C. L. C. Chan, M. M. Bay, G. Jacucci, R. Vadrucci, C. A. Williams, G. T. van de Kerkhof, R. M. Parker, K. Vynck, B. Frka-Petešić, and S. Vignolini, "Visual appearance of chiral nematic cellulose-based photonic films: Angular and polarization independent color response with a twist," *Adv. Mater.*, vol. 31, no. 52, p. 1905151, 2019.

[94] W. D. S. John, W. J. Fritz, Z. J. Lu, and D. K. Yang, "Bragg reflection from cholesteric liquid crystals," *Phys. Rev. E*, vol. 51, no. 2, pp. 1191–1198, 1995.

[95] B. D. Wilts, A. G. Dumanli, R. Middleton, P. Vukusic, and S. Vignolini, "Invited Article: Chiral optics of helicoidal cellulose nanocrystal films," *APL Photonics*, vol. 2, no. 4, 2017.

[96] D. W. Berreman, "Optics in stratified and anisotropic media: 4× 4-matrix formulation," *JOSA*, vol. 62, no. 4, pp. 502–510, 1972.

[97] H. L. de Vries, "Rotatory power and other optical properties of certain liquid crystals," *Acta Crystallogr.*, vol. 4, no. 3, pp. 219–226, 1951.

[98] E. I. Kats, "Optical properties of cholesteric liquid crystals," *Sov. Phys. JETP*, vol. 32, no. 5, pp. 1004–1007, 1971.

[99] R. Nityanada, "On the Theory of Light Propagation in Cholesteric Liquid Crystals.," *Mol Cryst Liq Cryst*, vol. 21, no. 3-4, pp. 315–331, 1973.

[100] G. H. Conners, "Electromagnetic Wave Propagation in Cholesteric Materials," *J. Opt. Soc. Am.*, vol. 58, no. 7, p. 875, 1968.

[101] M. M. Bay, S. Vignolini, and K. Vynck, "Pyllama: a stable and versatile python toolkit for the electromagnetic modeling of multilayered anisotropic media," 2020.

[102] K. Kurita, "Chitin and Chitosan: Functional Biopolymers from Marine Crustaceans," *Marine Biotechnology*, vol. 8, p. 203, Mar. 2006.

[103] Z. Değim, N. Çelebi, H. Sayan, A. Babül, D. Erdoğan, and G. Take, "An investigation on skin wound healing in mice with a taurine-chitosan gel formulation," *Amino Acids*, vol. 22, no. 2, pp. 187–198, 2002.

[104] Y. Shigemasa and S. Minami, "Applications of chitin and chitosan for biomaterials," *Biotechnol. Genet. Eng. Rev.*, vol. 13, no. 1, pp. 383–420, 1996.

[105] H. Zhou, Y. Tan, S. Lv, J. Liu, J. L. Muriel Mundo, L. Bai, O. J. Rojas, and D. J. McClements, "Nanochitin-stabilized pickering emulsions: Influence of nanochitin on lipid digestibility and vitamin bioaccessibility," *Food Hydrocoll.*, vol. 106, no. January, p. 105878, 2020.

[106] S. Hirano, T. Yamamoto, M. Hayashi, T. Nishida, and H. Inui, "Chitinase activity in seeds coated with chitosan derivatives," *Agric. Biol. Chem.*, vol. 54, no. 10, pp. 2719–2720, 1990.

[107] J. H. Willis, "Structural cuticular proteins from arthropods: annotation, nomenclature, and sequence characteristics in the genomics era," *Insect biochemistry and molecular biology*, vol. 40, pp. 189–204, Mar. 2010.

[108] J. E. Rebers and J. H. Willis, "A conserved domain in arthropod cuticular proteins binds," *Insect Biochemistry and Molecular Biology*, vol. 31, pp. 1083–1093, Oct. 2001.

[109] L. G. Greca, K. J. D. France, J. Majoinen, N. Kummer, O. I. V. Luotonen, S. Campioni, O. J. Rojas, G. Nyström, and B. L. Tardy, "Chitin–amyloid synergism and their use as sustainable structural adhesives," *Journal of Materials Chemistry A*, vol. 9, pp. 19741–19753, Sept. 2021.

[110] N. Aldred, V. B. S. Chan, K. Emami, K. Okano, A. S. Clare, and A. S. Mount, "Chitin is a functional component of the larval adhesive of barnacles," *Communications Biology*, vol. 3, p. 31, Jan. 2020.

[111] T. H. Tran, H. L. Nguyen, D. S. Hwang, J. Y. Lee, H. G. Cha, J. M. Koo, S. Y. Hwang, J. Park, and D. X. Oh, "Five different chitin nanomaterials from identical source with different advantageous functions and performances," *Carbohydr. Polym.*, vol. 205, no. July 2018, pp. 392–400, 2019.

[112] M. Roman and W. T. Winter, "Effect of sulfate groups from sulfuric acid hydrolysis on the thermal degradation behavior of bacterial cellulose," *Biomacromolecules*, vol. 5, no. 5, pp. 1671–1677, 2004.

[113] G. Guidetti, B. Frka-Petesic, A. G. Dumanli, W. Y. Hamad, and S. Vignolini, "Effect of thermal treatments on chiral nematic cellulose nanocrystal films," *Carbohydr. Polym.*, vol. 272, no. April, p. 118404, 2021.

[114] D. Dai and M. Fan, *Wood fibres as reinforcements in natural fibre composites: Structure, properties, processing and applications*. Woodhead Publishing Limited, 2013.

[115] X. M. Dong, J.-F. REVOL, and D. G. GRAY, "Effect of microcrystallite preparation conditions on the formation of colloid crystals of cellulose," *Cellulose*, vol. 5, pp. 19–32, Mar. 1998.

[116] D. G. Oonincx and I. J. de Boer, "Environmental Impact of the Production of Mealworms as a Protein Source for Humans - A Life Cycle Assessment," *PLoS One*, vol. 7, no. 12, pp. 1–5, 2012.

[117] V. Varelas, "Food wastes as a potential new source for edible insect mass production for food and feed: A review," *Fermentation*, vol. 5, no. 3, 2019.

[118] E. Pasquier, M. Beaumont, B. D. Mattos, C. G. Otoni, A. Winter, T. Rosenau, M. N. Belgacem, O. J. Rojas, and J. Bras, "Upcycling Byproducts from Insect (Fly Larvae and Mealworm) Farming into Chitin Nanofibers and Films," *ACS Sustain. Chem. Eng.*, 2021.

[119] N. D. Sanandiya, C. Ottenheim, J. W. Phua, A. Caligiani, S. Dritsas, and J. G. Fernandez, "Circular manufacturing of chitinous bio-composites via bioconversion of urban refuse," *Sci. Rep.*, vol. 10, no. 1, pp. 1–8, 2020.

[120] M. Paillet and A. Dufresne, "Chitin whisker reinforced thermoplastic nanocomposites," *Macromolecules*, vol. 34, no. 19, pp. 6527–6530, 2001.

[121] Y. Lu, L. Weng, and L. Zhang, "Morphology and properties of soy protein isolate thermoplastics reinforced with chitin whiskers," *Biomacromolecules*, vol. 5, no. 3, pp. 1046–1051, 2004.

[122] K. Gopalan Nair and A. Dufresne, "Crab Shell Chitin Whisker Reinforced Natural Rubber Nanocomposites. 1. Processing and Swelling Behavior," *Biomacromolecules*, vol. 4, pp. 657–665, May 2003.

[123] J. Sriupayo, P. Supaphol, J. Blackwell, and R. Rujiravanit, "Preparation and characterization of α-chitin whisker-reinforced chitosan nanocomposite films with or without heat treatment," *Carbohydr. Polym.*, vol. 62, no. 2, pp. 130–136, 2005.

[124] N. Naseri, C. Algan, V. Jacobs, M. John, K. Oksman, and A. P. Mathew, "Electrospun chitosan-based nanocomposite mats reinforced with chitin nanocrystals for wound dressing," *Carbohydr. Polym.*, vol. 109, pp. 7–15, 2014.

[125] J. Araki, Y. Yamanaka, and K. Ohkawa, "Chitin-chitosan nanocomposite gels: Reinforcement of chitosan hydrogels with rod-like chitin nanowhiskers," *Polym. J.*, vol. 44, no. 7, pp. 713–717, 2012.

[126] B. Ma, A. Qin, X. Li, X. Zhao, and C. He, "Bioinspired design and chitin whisker reinforced chitosan membrane," *Mater. Lett.*, vol. 120, pp. 82–85, 2014.

[127] B. Ma, A. Qin, X. Li, X. Zhao, and C. He, "Structure and properties of chitin whisker reinforced chitosan membranes," *Int. J. Biol. Macromol.*, vol. 64, pp. 341–346, 2014.

[128] M. V. Tzoumaki, T. Moschakis, V. Kiosseoglou, and C. G. Biliaderis, "Oil-in-water emulsions stabilized by chitin nanocrystal particles," *Food Hydrocoll.*, vol. 25, no. 6, pp. 1521–1529, 2011.

[129] S. Phongying, S. ichi Aiba, and S. Chirachanchai, "Direct chitosan nanoscaffold formation via chitin whiskers," *Polymer (Guildf).*, vol. 48, no. 1, pp. 393–400, 2007.

[130] T. Lertwattanaseri, N. Ichikawa, T. Mizoguchi, Y. Tanaka, and S. Chirachanchai, "Microwave technique for efficient deacetylation of chitin nanowhiskers to a chitosan nanoscaffold," *Carbohydr. Res.*, vol. 344, no. 3, pp. 331–335, 2009.

[131] R. Dolphen and P. Thiravetyan, "Adsorption of melanoidins by chitin nanofibers," *Chem. Eng. J.*, vol. 166, no. 3, pp. 890–895, 2011.

[132] P. Ang-atikarnkul, A. Watthanaphanit, and R. Rujiravanit, "Fabrication of cellulose nanofiber/chitin whisker/silk sericin bionanocomposite sponges and characterizations of their physical and biological properties," *Compos. Sci. Technol.*, vol. 96, pp. 88–96, 2014.

[133] P. Wongpanit, N. Sanchavanakit, P. Pavasant, T. Bunaprasert, Y. Tabata, and R. Rujiravanit, "Preparation and characterization of chitin whisker-reinforced silk fibroin nanocomposite sponges," *Eur. Polym. J.*, vol. 43, no. 10, pp. 4123–4135, 2007.

[134] Y. Zhou, S. Fu, Y. Pu, S. Pan, and A. J. Ragauskas, "Preparation of aligned porous chitin nanowhisker foams by directional freeze-casting technique," *Carbohydr. Polym.*, vol. 112, pp. 277–283, 2014.

[135] A. M. Salaberria, J. Labidi, and S. C. Fernandes, "Chitin nanocrystals and nanofibers as nano-sized fillers into thermoplastic starch-based biocomposites processed by melt-mixing," *Chem. Eng. J.*, vol. 256, pp. 356–364, 2014.

[136] J. Li, J.-F. Revol, and R. H. Marchessault, "Rheological properties of aqueous suspensions of chitin crystallites," *Journal of colloid and interface science*, vol. 183, no. 2, pp. 365–373, 1996.

[137] J. Li, J.-F. Revol, and R. Marchessault, "Effect of N-sulfonation on the colloidal and liquid crystal behavior of chitin crystallites," *J. Colloid Interface Sci.*, vol. 192, no. 2, pp. 447–457, 1997.

[138] A. M. Salaberria, J. Labidi, and S. C. Fernandes, "Different routes to turn chitin into stunning nano-objects," *Eur. Polym. J.*, vol. 68, pp. 503–515, 2015.

[139] T. Jin, T. Liu, E. Lam, and A. Moores, "Chitin and chitosan on the nanoscale," *Nanoscale Horizons*, vol. 6, no. 7, pp. 505–542, 2021.

[140] J. Meija, M. Bushell, M. Couillard, S. Beck, J. Bonevich, K. Cui, J. Foster, J. Will, D. Fox, W. Cho, M. Heidelmann, B. C. Park, Y. C. Park, L. Ren, L. Xu, A. B. Stefaniak, A. K. Knepp, R. Theissmann, H. Purwin, Z. Wang, N. De Val, and L. J. Johnston, "Particle Size Distributions for Cellulose Nanocrystals Measured by Transmission

Electron Microscopy: An Interlaboratory Comparison," *Anal. Chem.*, vol. 92, no. 19, pp. 13434–13442, 2020.

[141] M. Bushell, J. Meija, M. Chen, W. Batchelor, C. Browne, J. Y. Cho, C. A. Clifford, Z. Al-Rekabi, O. M. Vanderfleet, E. D. Cranston, M. Lawn, V. A. Coleman, G. Nyström, M. Arcari, R. Mezzenga, B. C. Park, C. H. Shin, L. Ren, T. Bu, T. Saito, Y. Kaku, R. Wagner, and L. J. Johnston, "Particle size distributions for cellulose nanocrystals measured by atomic force microscopy: an interlaboratory comparison," *Cellulose*, vol. 28, no. 3, pp. 1387–1403, 2021.

[142] M. S. Reid, M. Villalobos, and E. D. Cranston, "Benchmarking Cellulose Nanocrystals: From the Laboratory to Industrial Production," *Langmuir*, vol. 33, no. 7, pp. 1583–1598, 2017.

[143] G. L. Clark and A. F. Smith, "X-ray diffraction studies," *J. Phys. Chem.*, vol. 40, no. 7, pp. 863–879, 1996.

[144] Y. Qin, S. Zhang, J. Yu, J. Yang, L. Xiong, and Q. Sun, "Effects of chitin nanowhiskers on the antibacterial and physicochemical properties of maize starch films," *Carbohydr. Polym.*, vol. 147, pp. 372–378, 2016.

[145] S. Ge, Q. Liu, M. Li, J. Liu, H. Lu, F. Li, S. Zhang, Q. Sun, and L. Xiong, "Enhanced mechanical properties and gelling ability of gelatin hydrogels reinforced with chitin whiskers," *Food Hydrocoll.*, vol. 75, pp. 1–12, 2018.

[146] J. Pang, S. Bi, T. Kong, X. Luo, Z. Zhou, K. Qiu, L. Huang, X. Chen, and M. Kong, "Mechanically and functionally strengthened tissue adhesive of chitin whisker complexed chitosan/dextran derivatives based hydrogel," *Carbohydr. Polym.*, vol. 237, no. February, p. 116138, 2020.

[147] A. A. Oun and J. W. Rhim, "Effect of isolation methods of chitin nanocrystals on the properties of chitin-silver hybrid nanoparticles," *Carbohydr. Polym.*, vol. 197, no. June, pp. 349–358, 2018.

[148] Y. Fan, T. Saito, and A. Isogai, "Chitin nanocrystals prepared by TEMPO-mediated oxidation of α-chitin," *Biomacromolecules*, vol. 9, no. 1, pp. 192–198, 2008.

[149] J. Jiang, W. Ye, J. Yu, Y. Fan, Y. Ono, T. Saito, and A. Isogai, "Chitin nanocrystals prepared by oxidation of α-chitin using the O2/laccase/TEMPO system," *Carbohydr. Polym.*, vol. 189, no. August 2017, pp. 178–183, 2018.

[150] D. Liu, Y. Chang, D. Tian, W. Wu, A. Lu, N. Prempeh, M. Tan, and Y. Huang, "Lyotropic liquid crystal self-assembly of H2O2-hydrolyzed chitin nanocrystals," *Carbohydr. Polym.*, vol. 196, no. October 2017, pp. 66–72, 2018.

[151] Y. Yuan, S. Hong, H. Lian, K. Zhang, and H. Liimatainen, "Comparison of acidic deep eutectic solvents in production of chitin nanocrystals," *Carbohydr. Polym.*, vol. 236, no. January, p. 116095, 2020.

[152] S. Hong, Y. Yuan, K. Zhang, H. Lian, and H. Liimatainen, "Efficient hydrolysis of chitin in a deep eutectic solvent synergism for production of chitin nanocrystals," *Nanomaterials*, vol. 10, no. 5, 2020.

[153] W. M. F. B. W. Nawawi, M. Jones, R. J. Murphy, K.-Y. Lee, E. Kontturi, and A. Bismarck, "Nanomaterials Derived from Fungal Sources-Is It the New Hype?," *Biomacromolecules*, vol. 21, pp. 30–55, Jan. 2020.

[154] S. Ifuku, R. Nomura, M. Morimoto, and H. Saimoto, "Preparation of Chitin Nanofibers from Mushrooms," *Materials*, vol. 4, pp. 1417–1425, Aug. 2011.

[155] M. Kaya, I. Akata, T. Baran, and A. Menteş, "Physicochemical Properties of Chitin and Chitosan Produced from Medicinal Fungus (Fomitopsis pinicola)," *Food Biophysics*, vol. 10, pp. 162–168, June 2015.

[156] W. M. Fazli Wan Nawawi, K.-Y. Lee, E. Kontturi, R. J. Murphy, and A. Bismarck, "Chitin Nanopaper from Mushroom Extract: Natural Composite of Nanofibers and Glucan from a Single Biobased Source," *ACS Sustainable Chemistry & Engineering*, vol. 7, pp. 6492–6496, Apr. 2019.

[157] N. Lin, S. Zhao, L. Gan, P. R. Chang, T. Xia, and J. Huang, "Preparation of fungus-derived chitin nanocrystals and their dispersion stability evaluation in aqueous media," *Carbohydrate Polymers*, vol. 173, pp. 610–618, Oct. 2017.

[158] R. H. Marchessault, F. F. Morehead, and M. J. Koch, "Some Hydrodynamic Properties of Neutral As Related To Size and Shape," *J. Colloid Sci.*, vol. 344, pp. 327–344, 1961.

[159] J. Bouchard, M. Méthot, C. Fraschini, and S. Beck, "Effect of oligosaccharide deposition on the surface of cellulose nanocrystals as a function of acid hydrolysis temperature," *Cellulose*, vol. 23, no. 6, pp. 3555–3567, 2016.

[160] T. G. Parton, G. Van De Kerkhof, A. Narkevicius, J. Haataja, R. M. Parker, B. Frka-Petesic, and S. Vignolini, "Chiral Self-Assembly of Cellulose Nanocrystals is Driven by Crystallite Bundles," *Arxiv*, 2021.

[161] Y. Yamamoto, T. Nishimura, T. Saito, and T. Kato, "CaCO3/chitin-whisker hybrids: Formation of CaCO3crystals in chitin-based liquid-crystalline suspension," *Polym. J.*, vol. 42, no. 7, pp. 583–586, 2010.

[162] E. Lizundia, T.-D. Nguyen, R. J. Winnick, and M. J. MacLachlan, "Biomimetic photonic materials derived from chitin and chitosan," *Journal of Materials Chemistry C*, vol. 9, no. 3, pp. 796–817, 2021.

[163] Y. Habibi, L. A. Lucia, and O. J. Rojas, "Cellulose nanocrystals: Chemistry, self-assembly, and applications," *Chem. Rev.*, vol. 110, no. 6, pp. 3479–3500, 2010.

[164] L. Bai, S. Huan, W. Xiang, L. Liu, Y. Yang, R. W. N. Nugroho, Y. Fan, and O. J. Rojas, "Self-Assembled Networks of Short and Long Chitin Nanoparticles for Oil/Water Interfacial Superstabilization," *ACS Sustainable Chemistry & Engineering*, vol. 7, pp. 6497–6511, Apr. 2019.

[165] M. V. Tzoumaki, T. Moschakis, V. Kiosseoglou, and C. G. Biliaderis, "Oil-in-water emulsions stabilized by chitin nanocrystal particles," *Food Hydrocoll.*, vol. 25, no. 6, pp. 1521–1529, 2011.

[166] M. V. Tzoumaki, T. Moschakis, E. Scholten, and C. G. Biliaderis, "In vitro lipid digestion of chitin nanocrystal stabilized o/w emulsions," *Food Funct.*, vol. 4, no. 1, pp. 121–129, 2013.

[167] E. Perrin, H. Bizot, B. Cathala, and I. Capron, "Chitin nanocrystals for pickering high internal phase emulsions," *Biomacromolecules*, vol. 15, no. 10, pp. 3766–3771, 2014.

[168] Y. Huang, J. Yang, L. Chen, and L. Zhang, "Chitin Nanofibrils to Stabilize Long-Life Pickering Foams and Their Application for Lightweight Porous Materials," *ACS Sustain. Chem. Eng.*, vol. 6, no. 8, pp. 10552–10561, 2018.

[169] L. Heath, L. Zhu, and W. Thielemans, "Chitin nanowhisker aerogels," *ChemSusChem*, vol. 6, no. 3, pp. 537–544, 2013.

[170] M. Nogi, F. Kurosaki, H. Yano, and M. Takano, "Preparation of nanofibrillar carbon from chitin nanofibers," *Carbohydrate Polymers*, vol. 81, pp. 919–924, July 2010.

[171] Y. Tsutsumi, H. Koga, Z.-D. Qi, T. Saito, and A. Isogai, "Nanofibrillar Chitin Aerogels as Renewable Base Catalysts," *Biomacromolecules*, vol. 15, pp. 4314–4319, Nov. 2014.

[172] L. Liu, R. Wang, J. Yu, J. Jiang, K. Zheng, L. Hu, Z. Wang, and Y. Fan, "Robust Self-Standing Chitin Nanofiber/Nanowhisker Hydrogels with Designed Surface Charges and Ultralow Mass Content via Gas Phase Coagulation," *Biomacromolecules*, vol. 17, pp. 3773–3781, Nov. 2016.

[173] K. Gopalan Nair and A. Dufresne, "Crab Shell Chitin Whisker Reinforced Natural Rubber Nanocomposites. 2. Mechanical Behavior," *Biomacromolecules*, vol. 4, pp. 666–674, May 2003.

[174] S.-L. Cao, W.-M. Gu, W.-D. Ou-Yang, D.-C. Chen, B.-Y. Yang, L.-H. Lai, Y.-D. Wu, Y.-J. Liu, J. Zhu, W.-J. Chen, Z.-Q. Gai, X.-D. Hou, Y.-Z. Ma, and Y.-X. An, "Preparation, characterization and application of rod-like chitin nanocrystal by using p-toluenesulfonic acid/choline chloride deep eutectic solvent as a hydrolytic media," *Carbohydrate Polymers*, vol. 213, pp. 304–310, June 2019.

[175] K. Kurita, "Controlled functionalization of the polysaccharide chitin," *Progress in Polymer Science*, vol. 26, pp. 1921–1971, Nov. 2001.

[176] W. M. Argüelles-Monal, J. Lizardi-Mendoza, D. Fernández-Quiroz, M. T. Recillas-Mota, and M. Montiel-Herrera, "Chitosan Derivatives: Introducing New Functionalities with a Controlled Molecular Architecture for Innovative Materials," *Polymers*, vol. 10, p. 342, Mar. 2018.

[177] L. C. R. Carvalho, F. Queda, C. V. A. Santos, and M. M. B. Marques, "Selective Modification of Chitin and Chitosan: En Route to Tailored Oligosaccharides," *Chemistry – An Asian Journal*, vol. 11, no. 24, pp. 3468–3481, 2016.

[178] A. S. Kritchenkov and Y. A. Skorik, "Click reactions in chitosan chemistry," *Russ. Chem. Bull.*, vol. 66, no. 5, pp. 769–781, 2017.

[179] J. K. K. Lee, H. S. S. Lim, and J. H. H. Kim, "Cytotoxic activity of aminoderivatized cationic chitosan derivatives," *Bioorganic Med. Chem. Lett.*, vol. 12, no. 20, pp. 2949–2951, 2002.

[180] H. C. Kolb and K. B. Sharpless, "The growing impact of click chemistry on drug discovery," *Drug Discovery Today*, vol. 8, pp. 1128–1137, Dec. 2003.

[181] H. C. Kolb, M. G. Finn, and K. B. Sharpless, "Click Chemistry: Diverse Chemical Function from a Few Good Reactions," *Angewandte Chemie International Edition*, vol. 40, no. 11, pp. 2004–2021, 2001.

[182] S. Jung and H. Yi, "Fabrication of chitosan-poly(ethylene glycol) hybrid hydrogel microparticles via replica molding and its application toward facile conjugation of biomolecules," *Langmuir*, vol. 28, no. 49, pp. 17061–17070, 2012.

[183] O. Boutureira and G. J. Bernardes, "Advances in chemical protein modification," *Chem. Rev.*, vol. 115, no. 5, pp. 2174–2195, 2015.

[184] S. S. Wong and L.-J. C. Wong, "Chemical crosslinking and the stabilization of proteins and enzymes," *Enzym. Microb. Technol.*, vol. 14, 1992.

[185] J. N. DeGruyter, L. R. Malins, and P. S. Baran, "Residue-Specific Peptide Modification: A Chemist's Guide," *Biochemistry*, vol. 56, no. 30, pp. 3863–3873, 2017.

[186] H. K. No and S. P. Meyers, "Preparation and characterization of chitin and chitosan—a review," *J. Aquat. Food Prod. Technol.*, vol. 4, no. 2, pp. 27–52, 1995.

[187] C. A. Schneider, W. S. Rasband, and K. W. Eliceiri, "Nih image to imagej: 25 years of image analysis," *Nature methods*, vol. 9, no. 7, pp. 671–675, 2012.

[188] D. Nečas and P. Klapetek, "Gwyddion: an open-source software for SPM data analysis," *Central European Journal of Physics*, vol. 10, pp. 181–188, 2012.

[189] "Operating manual, axio scope.a1, microscope for routine and entry-level research," 2012.

[190] S. Park, J. O. Baker, M. E. Himmel, P. A. Parilla, and D. K. Johnson, "Cellulose crystallinity index: measurement techniques and their impact on interpreting cellulase performance," *Biotechnology for biofuels*, vol. 3, no. 1, pp. 1–10, 2010.

[191] C. Kittel, *Introduction to solid state physics*. John Wiley & Sons, Inc., 2005.

[192] V. K. Krieble and K. A. Holst, "Amide Hydrolysis with High Concentrations of Mineral Acids," *J. Am. Chem. Soc.*, vol. 60, no. 12, pp. 2976–2980, 1938.

[193] H. Merzendorfer, "The cellular basis of chitin synthesis in fungi and insects: common principles and differences," *European journal of cell biology*, vol. 90, no. 9, pp. 759–769, 2011.

[194] N. Lin, S. Zhao, L. Gan, P. R. Chang, T. Xia, and J. Huang, "Preparation of fungus-derived chitin nanocrystals and their dispersion stability evaluation in aqueous media," *Carbohydr. Polym.*, vol. 173, pp. 610–618, 2017.

[195] J. H. Sietsma and J. G. H. Wessels, "Solubility of (1-3)-β-d/(1-6)-β-d-glucan in fungal walls: Importance of presumed linkage between glucan and chitin," *Microbiology*, vol. 125, no. 1, pp. 209–212, 1981.

[196] S. Ifuku, R. Nomura, M. Morimoto, and H. Saimoto, "Preparation of chitin nanofibers from mushrooms," *Materials*, vol. 4, no. 8, pp. 1417–1425, 2011.

[197] I. Hughes and T. Hase, *Measurements and their uncertainties: a practical guide to modern error analysis*. OUP Oxford, 2010.

[198] D. Carlstrom, "The crystal structure of α-chitin (poly-n-acetyl-d-glucosamine)," *The Journal of Cell Biology*, vol. 3, no. 5, pp. 669–683, 1957.

[199] N. Suksangpanya, N. A. Yaraghi, D. Kisailus, and P. Zavattieri, "Twisting cracks in bouligand structures," *Journal of the mechanical behavior of biomedical materials*, vol. 76, pp. 38–57, 2017.

[200] K. Yao, Q. Meng, V. Bulone, and Q. Zhou, "Flexible and Responsive Chiral Nematic Cellulose Nanocrystal/Poly(ethylene glycol) Composite Films with Uniform and Tunable Structural Color," *Adv. Mater.*, vol. 29, no. 28, pp. 1–8, 2017.

[201] T.-D. Nguyen, K. E. Shopsowitz, and M. J. MacLachlan, "Mesoporous silica and organosilica films templated by nanocrystalline chitin," *Chemistry–A European Journal*, vol. 19, no. 45, pp. 15148–15154, 2013.

[202] A. Mendoza-Galván, E. Muñoz-Pineda, K. Järrendahl, and H. Arwin, "Birefringence of nanocrystalline chitin films studied by Mueller-matrix spectroscopic ellipsometry," *Opt. Mater. Express*, vol. 6, no. 2, p. 671, 2016.

[203] Y. Ogawa, Y. Nishiyama, and K. Mazeau, "Drying-induced bending deformation of cellulose nanocrystals studied by molecular dynamics simulations," *Cellulose*, vol. 27, no. 17, pp. 9779–9786, 2020.

[204] D. Yang, X.-W. Peng, L.-X. Zhong, X.-F. Cao, W. Chen, and R.-C. Sun, "Effects of pretreatmetns onf crystalline properties and morphology of cellulose nanocrystals," *Cellulose*, vol. 20, pp. 2427–2437, 2013.

[205] Y. Fan, T. Saito, and A. Isogai, "Preparation of chitin nanofibers from squid Pen β-chitin by simple mechanical treatment under acid conditions," *Biomacromolecules*, vol. 9, no. 7, pp. 1919–1923, 2008.

[206] D. Raabe, C. Sachs, and P. Romano, "The crustacean exoskeleton as an example of a structurally and mechanically graded biological nanocomposite material," *Acta Materialia*, vol. 53, pp. 4281–4292, Sept. 2005.

[207] S. Sviben, O. Spaeker, M. Bennet, M. Albéric, J. H. Dirks, B. Moussian, P. Fratzl, L. Bertinetti, and Y. Politi, "Epidermal Cell Surface Structure and Chitin-Protein Co-assembly Determine Fiber Architecture in the Locust Cuticle," *ACS Appl. Mater. Interfaces*, vol. 12, no. 23, pp. 25581–25590, 2020.

Appendix A

Double layer calculations

While it is a useful approximation to consider the effective diameter to be $D_{eff} = D + 2\kappa^{-1}$, where D is the physical diameter and κ^{-1} is the Debye length, it is a very rough approximation at best. It does not include the effects, e.g., that the surface charge imparts on D_{eff}. Starting from the assumption that ChNCs are perfect charged cylinders, their effective diameter (D_{eff}) can be mathematically expressed as: [49]

$$D_{eff} = D + \kappa^{-1}(lnA + 0.7704) \tag{A.1}$$

where A is a constant. The mathematical expression for κ^{-1} at 20 °C, in water is approximated to:

$$\kappa^{-1} = \frac{0.304}{I} \tag{A.2}$$

where the ionic strength, I, when used in mol/L (M), give κ^{-1} in nanometres.

The constant, A, has a more complicated mathematical expression:

$$A = 2\pi v_{eff}^2 \lambda_b \kappa^{-1} e^{-\kappa D} \tag{A.3}$$

where λ_b is the Bjerrum length (0.714 nm in water at 20 °C), and v_{eff} is the linear charge density. However, for colloidal nanoparticles such as ChNCs and CNCs, only the surface charge density can be directly evaluated experimentally. However, an apparent linear charge density can be calculated from surface charge density by employing the following equation:

$$v_{eff} = \frac{2\pi\kappa^{-1}\sigma}{K_1(\kappa D/2)} \tag{A.4}$$

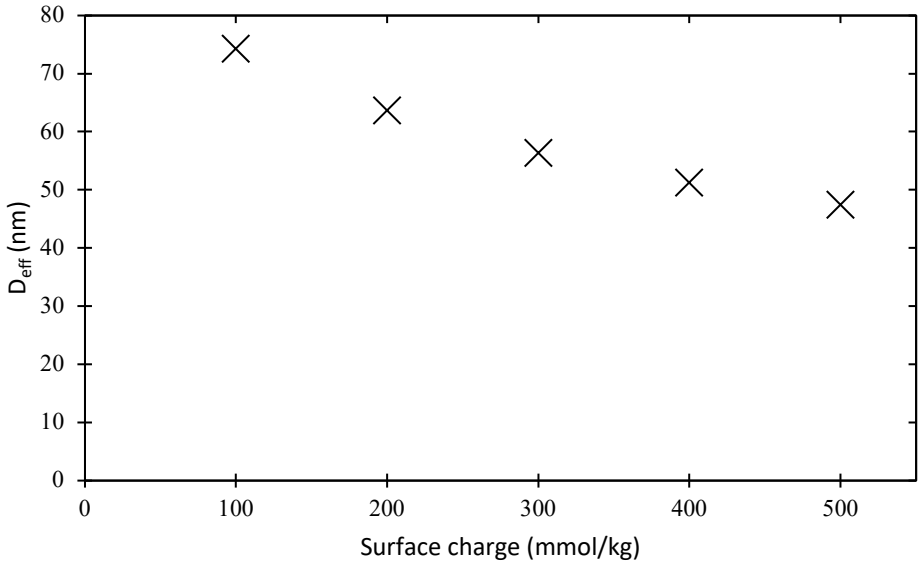

Figure A.1 Effective diameter of ChNC as a function of surface charge.

where σ is the surface charge density and K_1 is the first order Bessel function evaluated at $\kappa D/2$.

While we now have all the required equations to calculate the D_{eff}, the colloidal nanoparticles such as ChNCs are charged and their contribution to the ionic strength should not be neglected, and so the expression for the Debye length is altered to account for that:

$$\kappa^{-1} = \frac{0.304}{I + \Gamma z_p C_p} \tag{A.5}$$

where z_p is the valency of the polyelectrolyte, C_p the concentration of the polyelectrolyte, and Γ denotes Donnan salt exclusion coefficient:

$$\Gamma = (\frac{4\lambda_b}{\beta})^{-1} \tag{A.6}$$

with β being the distance between the charges. The equation for Γ is true while $\lambda_b/\beta > 1$, which is satisfied as the approximate inter-charge distance for CNCs and ChNCs is at least 0.2 nm. [115]

Based on the experimental measurements, it is safe to assume that the average nanoparticle dimensions for sChNC can be taken to be 200 nm (length) and 15 nm (width). The surface charge determined by conductometrically was 280 mmol/kg, chitin density is 1.425. [198] Taking ionic strength of 1 mM and a suspension at 1.00 wt%, the resulting calculations are presented in Figure A.1, where it shows that the increase in surface charge, counter-intuitively,

reduces D_{eff}. This can be rationalised by realised that the charged polyelectrolytes, like ChNCs and CNCs, have counterions which contribute to the ionic strength, thus reducing the Debye length and outweighing the expansion of the double layer caused by the higher potential due to the higher surface charge.